AN OBJECT-BASED APPROACH FOR QUANTIFICATION OF GCM BIASES IN THE SIMULATION OF OROGRAPHIC PRECIPITATION

by

Muharrem Soner Yorgun

A dissertation submitted in partial fulfillment
of the requirements for the degree of
Doctor of Philosophy
(Atmospheric, Oceanic and Space Sciences)
in The University of Michigan
2014

Doctoral Committee:

      Professor Richard B. Rood, Chair
      Associate Professor Christiane Jablonowski
      Assistant Professor Derek J. Posselt
      Professor Ji Zhu

to mom...

ACKNOWLEDGEMENTS

First and foremost, I would like to express my deepest gratitude for my advisor and mentor Prof. Richard B. Rood for his invaluable guidance not only in my research, but also in academic life, and life in general. It was an honor working with and learning from a person who combines accomplishment and modesty in such an elegant way, which inspired me greatly. His patience and support during my hard times have been of paramount importance for this thesis to be concluded, and will never be forgotten. I feel extremely lucky to have crossed paths with him in my life.

I would like to thank one of the most brilliant scientists I have ever met, Prof. Derek J. Posselt, for his continuous help since the beginning of my research. His extensive knowledge on both the conceptual and the quantitative aspects of climate science have been extremely helpful in many areas of my research. I would also like to thank Prof. Christiane Jablonowski for her invaluable input throughout my whole dissertation. Her rigorous approach and sharp insight made me a much better and more versatile scientist. I would like to thank Prof. Ji Zhu for teaching me the methods, which contributed to a crucial part of my dissertation and led to its conclusion. I would also like to thank Dr. Gerald Potter for his constant encouragement and help throughout my research. The data he provided and the analysis techniques he instructed played a crucial role in the completion of my dissertation. I would also like to thank Prof. Natalia Andronova for all her help and support, and for being such a beautiful person and inspiring me to be so. I wish she could have been with us here and see me graduate. I will always remember her with a smile on my face and with happiness, which she instilled in anyone she knew.

I would also like to thank Dr. Lawrence Buja and Dr. Julie Caron from the National Center for Atmospheric Research for providing me valuable computational

TABLE OF CONTENTS

LIST OF FIGURES

<u>Figure</u>

ABSTRACT

AN OBJECT-BASED APPROACH FOR QUANTIFICATION OF GCM BIASES IN
THE SIMULATION OF OROGRAPHIC PRECIPITATION

by

Muharrem Soner Yorgun

Chair: Richard B. Rood

An object-based evaluation method to identify and quantify biases of General Circulation Models (GCMs) is introduced. The focus is on how orographic precipitation is simulated by the Eulerian Spectral Transform and the finite volume (FV) dynamical cores within the National Center of Atmospheric Research (NCAR) Community Earth System Model (CESM) with its Community Atmosphere Model (CAM). The "local" biases introduced by dynamical cores and how they evolve with varying model resolution are quantified by looking at simulated precipitation over the Coast Range and the Sierra Nevada mountains on the West Coast of North America.

The first step of the object-based method involves identification of orographic precipitation features (study features) simulated differently by the CAM Eulerian Spectral Transform and CAM FV dynamical cores. We examined Atmospheric Model Intercomparison Project (AMIP) model simulations together with Global Precipitation Climatology Center (GPCC) observations to select the study features. There are significant differences of orographic precipitation simulated over local, complex topography. CAM FV resembled the observed spatial pattern of precipitation better than the CAM Eulerian Spectral Transform scheme. As the second step of the method, idealized experiments of orographic precipitation were conducted running the Community Atmosphere Model (CAM) coupled with a simplified physics parameterization to understand the causes of this difference between the CAM FV and

the CAM Eulerian Spectral Transform dynamical cores. Initially, zonal flow produced waves as the mountains perturbed the flow. Three different mechanisms of precipitation were isolated due to (a) stable upslope ascent, (b) local surface fluxes and moisture transport, and (c) resolved downstream waves. The application of spectral filtering to topography is shown to have a large effect on spectral model simulation. The removal of filtering improved the results when the scales of the topography (thus the scales of precipitation features) were resolvable. However, it reduced the simulation capability of the spectral dynamical core (introducing Gibbs oscillations) when the scales were smaller, leading to unrealistic results.

The idealized experiments reproduced the spatial characteristics of FV and spectral dynamical cores that were observed in the AMIP simulations. This led to better understanding of orographic precipitation features allowing better identification and isolation of features as "objects" using pattern recognition methods such as clustering and classification trees. The results of the object-based evaluation method revealed quantitative signatures of how the CAM Eulerian Spectral Transform model in AMIP simulations, unlike the CAM FV model, failed to reproduce the precipitation structure observed in the GPCC observations. It is shown that the CAM Eulerian Spectral Transform model simulations become more unrealistic as the resolvable scales of the simulated precipitation gets smaller, and the amount of simulated precipitation gets larger. The reasons of this problematic representation of orographic precipitation by the CAM Eulerian Spectral Transform dynamical core (i.e. bias) can be summarized in three categories: (a) bias due to spectral filtering of the topography, (b) bias in small-scale phenomena due to spectral transform method, (c) grid scale variability (noise) due to spectral transform method. The results also indicated stronger sensitivity of the CAM Eulerian Spectral Transform dynamical core to model resolution.

CHAPTER 1: INTRODUCTION

All of the state-of-the-art general circulation models (GCMs) have systematic errors in their simulation of the present climate. These systematic errors, *i.e.* biases, are sometimes quite resilient to putative improvements in model formulation. It has proved difficult to isolate cause and effect; that is, linking model formulation or model components to the presence or absence of a particular bias. For example, a common experimental approach is to change some model component, for instance the convective parameterization or dynamical core, and evaluate the impact of the change on the global climate. Improvements are sometimes realized and other times they are not. Often there is an ambiguous mix of results.

This study is motivated by the hypothesis that there is a subset of the biases in climate simulations that are at the mechanistic level; that is, the bias is the manifestation of a poor representation of quasi-local mechanisms rather that the residue of global inadequacies of, for instance, model parameterizations. There are two main objectives of this study:

- Identification and quantification of local biases in GCM simulations. Determination of structural GCM components that lead to these biases and examining the evolution of these biases with changing resolution
- Development of an object-based verification framework to be used in bias quantification that is applicable to a broad range of problems involving climate and numerical weather prediction (NWP) models.

The second objective involves development of a quantitative method to validate the "meteorological realism" of climate models. Deterministic weather predictions are often validated with feature-by-feature comparison. Probabilistic weather forecasts and climate simulations are evaluated with statistical methods. Model evaluation strategies that

identify similar "objects" – coherent systems with an associated set of measurable parameters (Douglass 2000) – are developed within the scope of the study. This makes it possible to evaluate processes in models without needing to reproduce the time and location of, for example, a particular observed cloud system. Process- and object-based evaluation preserves information in the observations by avoiding the need for extensive spatial and temporal averaging. Of particular interest in this research is the interaction of the dynamical core and the physical parameterizations, and how this interaction is affected as resolution is increased. In this context, the focus is on the representation of the orographic precipitation by spectral and finite volume dynamical cores. (Detailed discussion of dynamical cores is given in section 1.1). Candidate phenomena to be analyzed would be expected to have identifiable underlying fluid-dynamical features, which organize their spatial structure and correlated behavior between different parameters. The chosen phenomenon is the wintertime western United States orographic precipitation since it is relatively easy to isolate and there exists sufficient observational data for that area. The bias quantification of GCMs in their simulation of orographic precipitation is a complex problem. Therefore, this problem is broken down into simpler parts that will allow efficient scientific examination. The findings from each part of the problem are then linked back to the broader definitions of GCMs and their simulation of local processes to reconstruct scientific evidence of model biases and their origins.

The next section (1.1) gives information about the structure of GCMs with a specific focus on dynamical cores. Section 1.2 discusses the theory of orographic precipitation and the previous studies about its diagnostic and prognostic modeling. The notion of meteorological realism for model evaluation purposes is introduced in section 1.3. The general details of object-based analysis and the approach of this study using such analysis are also explained in section 1.3. Sections 2, 3, and 4 contain the discussion of the results of the approach and the conclusions are given in section 5.

1.1. General Circulation Models (GCMs)

GCMs are composed of multiple components that are connected together yielding a complex system. A climate model is composed of components such as a sea ice model, a land surface model, an ice sheet model, an ocean model and an atmospheric model, to simulate processes that affect the climate (e.g., cloud macro and microphysics, tracer transport etc.). The clouds component can be composed of other subcomponents that represent the different phases of water, aerosols, black carbon etc. Components at all levels need to communicate with each other through a coupler (Rood 2011). Figure 1 shows the Earth System Modeling Framework (ESMF) component architecture of the Goddard Earth Observing System, version 5 (GEOS-5) atmospheric model (Rienecker et al. 2008). From the top down, the structure shows the coupling of the atmospheric general circulation model ('agcm'), with the stored, digital 'history' files used in model initialization, diagnostics and application. The 'agcm' is composed of 'dynamics' and 'physics' combined with a coupler.
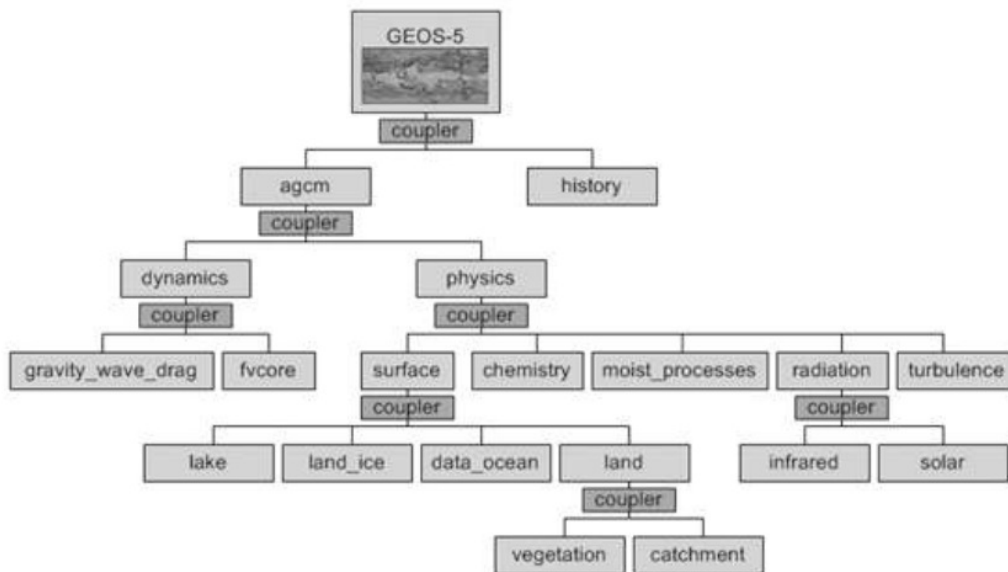
Figure 1: *Component architecture of the GEOS-5 atmosphere model.*

The advection and part of the sub-scale mixing algorithms are often identified as 'dynamics' ('fvcore' in Figure 1) and all of the other algorithms are identified as 'physics'. There is no standard definition of the term 'dynamical core' (in short 'dycore') (Rood 2011). Williamson (2007) defines the dynamical core to be 'the resolved fluid flow component of the model'. Thuburn (2008) used: 'the formulation of a numerical model of the atmosphere is usually considered to be made up of a dynamical core, and some parameterizations. Roughly speaking, the dynamical core solves the governing fluid and thermodynamic equations on resolved scales, while the parameterizations represent subgrid scale processes and other processes not included in the dynamical core such as radiative transfer'. In their simplest expressions, dynamical cores are generally include the following (Rood 2011):

- The resolved advection in the horizontal plane
- The resolved vertical advection
- Unresolved subscale transport
- A portfolio of filters and fixers that accommodate errors related to both the numerical technique and the characteristics of the underlying grid.

GCMs employ various dynamical cores for numerical modeling of advection. These dynamical cores include schemes such as quasi-Lagrangian, semi-Lagrangian, spectral, finite element, finite volume etc. This study focuses on the Eulerian spectral transform (EUL) and finite volume dynamical core components of the National Center for Atmospheric Research (NCAR) Community Atmosphere Model (CAM) version 3.0 (Collins et al. 2006), and version 5.0 (Neale et al. 2010).

1.1.1. CAM Eulerian Spectral Transform (EUL)

Spectral transform model schemes have been widely used in general circulation models since they can simulate the waveform behavior – the form which most of the large-scale features in the atmosphere is like – less expensively by using transformations between the gridded data and the waveform. Many wave-like features of the atmosphere are best simulated with a wave formulation. In spectral transform models, global basis functions are used to describe the horizontal spatial structure of the variables and hence information from both upstream and downstream influences a particular point in space. The vertical discretization in the CAM Eulerian Spectral Transform model is achieved via finite differences in a hybrid coordinate system (Neale et al. 2010).

The computational flow of a spectral GCM proceeds as the data fields are transformed to grid space at every time step via fast Fourier transforms and Gaussian quadrature (a form of numerical integration) and back to spectral space via Legendre transforms and Fourier transforms (McGuffie and Henderson-Sellers 2005). However, as these spectral harmonics are susceptible to Gibbs oscillations (erroneous simulations that arise when the spectral projection is used to represent fields with sharp spatial gradients or "discontinuities (Navarra et al. 1994)), spectral models are prone to produce unrealistic rippling, especially when dealing with sharp gradients, i.e. orographic precipitation, which is the subject of this study. Models employ different forms of dissipation/diffusion to mitigate rippling as well as other numerical noise generated by dispersion errors or computational modes. Explicit diffusion of varying degrees (such as second, fourth or higher order) is widely used to remove Gibbs oscillations in spectral models (Jablonowski and Williamson 2011). Relevant to our study, models also apply a terrain filter, which is an adoption of a monotonic filter (Bala et al. 2008b) to get a smoother topography, thus damping the gradients to reduce Gibbs oscillations. These filters, being

useful in removing noise, create a tradeoff between numerical artifacts, accuracy and physical realism.

1.1.2. CAM Finite Volume (FV)

Lin (2004) presented a multidimensional flux-form semi-Lagrangian transport scheme called the finite volume (FV) method, which is a generalization of 1D FV schemes to multi-dimensions combined with an efficient algorithm to reduce the stringent time-step stability requirements. The algorithm aimed to conserve mass without *a posteriori* restoration, compute fluxes based on the subgrid distribution in the upwind direction, generate no new maxima or minima, preserve tracer correlations, and be computationally efficient in spherical geometry (Lin and Rood 1996; Lin and Rood 1997). This algorithm eliminated the need for directional splitting which produce unacceptably large errors near the poles where the splitting errors are greatly amplified by the convergence of the meridians (Lin and Rood 1996). This scheme also solved the Pole-Courant problem, which arises from the close spacing of grid points towards the poles requiring extremely small time steps to maintain bounded Courant numbers for typical finite difference techniques. This problem was solved via the physical consideration of the contribution to fluxes from upstream volumes as far away as the Courant number indicated. The resulting multidimensional scheme was free of the Gibbs oscillations (with the optional monotonicity constraint), mass conserving, and stable for Courant number greater than one in the longitudinal direction. In addition to this progression, Lin and Rood (1997) adapted this scheme to the shallow water dynamical framework, which provided the consistent transport of the mass, the absolute vorticity, and the potential vorticity. The vertical discretization is Lagrangian with a conservative re-mapping, which essentially makes it quasi-Lagrangian (Lin 2004). Rasch et al. (2006) compared the tracer transport properties of the Eulerian spectral transform , semi-Lagrangian spectral transform, and FV numerical methods in CAM 3.0. They found that

the FV core is, unlike the Eulerian and semi-Lagrangian spectral transform cores, conservative and less diffusive. It also accurately maintains the nonlinear relationships (required by thermodynamic and mass conservation constraint) among conserved and non-conserved variables that are influenced by adiabatic and non-adiabatic processes.

The simulation of orographic precipitation by the Eulerian spectral transform and FV dynamical cores involves differences due to the numerical schemes discussed above. The next section discusses the physics of orographic precipitation and its modeling by diagnostic and prognostic (e.g., GCMs) models. Previous studies about the simulation of orographic precipitation by the spectral transform and the FV dynamical cores are also discussed.

1.2. Orographic Precipitation

Precipitation is a crucial element of the climate system since it has a paramount importance for fields such as agriculture, natural hazard assessment, water resource management, etc. The spatial and temporal changes in distribution of global precipitation are important thus the accurate simulation of precipitation is a high priority. However; due to the discontinuous and highly complex nature of precipitation in time and space precipitation is a challenging parameter for climate models to simulate. This challenge mostly arises due to the fact that the majority of precipitation occurs at scales less than the grid resolution GCMs. Validating climate models' performance using precipitation is an exacting test of a model's fidelity to the real world (i.e. meteorological realism) (Airey and Hulme 1995).

Orographic precipitation is a complex phenomenon due to the physical mechanisms involved, encompassing fluid dynamics, thermodynamics, and micro-scale cloud processes, as well as being dependent on the larger-scale patterns of the atmospheric

general circulation (Roe 2005). In addition to the problematic representation of the cloud microphysics by GCM's due to the fine scale of occurrence of these processes, orography introduces complexity regarding the dynamics of the flow. Figure 2 shows the schematic illustrations of different mechanisms of orographic precipitation.
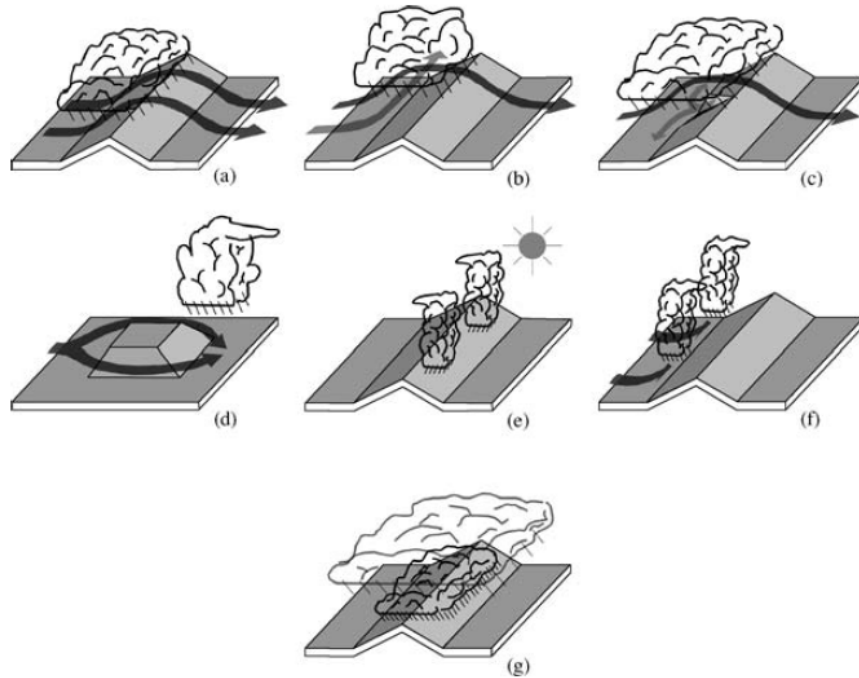
Figure 2: *Schematic illustrations of different mechanisms of orographic precipitation. (a) Stable upslope ascent, (b) partial blocking of the impinging air mass, (c) down valley flow induced by evaporative cooling, (d) lee-side convergence, (e) convection triggered by solar heating, (f) convection owing to mechanical lifting above level of free convection, and (g) seeder-feeder mechanism (Roe 2005).*

The stable upslope ascend shown in Figure 2a is the most general and straightforward mechanism of orographic precipitation. This mechanism is the result of air impinging onto the windward face of the mountain and lifting and cooling of the air column leading to condensation and precipitation. The air mass undergoes warming and drying due to descent on the leeward side of the mountain, which suppresses the precipitation and causes the "mountain shadow" over the leeward area. This mechanism is a good first-order description (e.g., Smith 2003) of the precipitation process at the scale of large mid-

latitude mountain ranges. Another mechanism is due to blockage of the flow (Figure 2b), which can be observed when the atmosphere is stable, or the flow is weak thus leading to stagnation or diversion of the flow along the windward flank of the mountain. This blocked air can cause ascent further windward of the range and can also enhance lifting (and hence precipitation) that does occur. The structure of the mountains can also affect the flow (Figure 2c) characteristics, which in turn raises the questions: how do GCMs represent the orography? What is the effect of the structural for of the orography on the representation of precipitation and how does it change with increasing resolution? The flow also can be diverted around the mountain in the case of narrow ranges, and create precipitation where a mountain shadow could be expected (Figure 2d). Triggering of unstable convection (Banta 1990) is another possible response of the atmosphere to orography. The air mass that undergoes mechanical lifting may rise above the level at which it becomes less dense than its surrounding (i.e. the free convection level). This will lead to a sustained rise of the air mass and lead to precipitation (Figure 2e). Heating can occur on mountain slopes facing the sun, which can cause convection and precipitation (Figure 2f). A final mechanism that is commonly involved is the "seeder-feeder" mechanism (Bergeron 1968) (Figure 2g). The seeder-feeder mechanism generally involves a large-scale precipitating cloud (seeder) at higher levels that is undisturbed by the orography which precipitates and feeds another low-level cloud over topography (feeder).

The diagnostic models that aim to describe orographic precipitation rely on the fact that the amount of precipitation tends to increase with the steeper windward slopes as a result of enhanced lifting and tends to decrease with elevation owing to the Clausius-Clapeyron effect (Alpert 1986; Barros and Lettenmaier 1994; Sanberg and Oerlemans 1983; Smith 1979). A highly adaptable orographic precipitation model was developed by Smith and Barstad (2004) in which they incorporated a linear atmospheric response. One of the advantages of this model is its efficiency of the calculation over complex terrain. Also, cloud microphysics are represented by characteristic delay timescales for

hydrometeor growth and fallout. Vertically integrated steady-state governing equations for condensed water were solved using Fourier transform techniques. However the model also has its caveats – the model includes crude representations of the physical processes that provide the proper weights to different scales and there are strong assumptions in the model formulation (such as linear steady wave dynamics and near saturation conditions). The model also treated only the vertically integrated condensed water and is unsuitable for unstable atmospheres. Roe and Baker (2006) developed an extension of the classic upslope model, which incorporates an explicit representation in the vertical dimension, represents the finite growth of hydrometeors, their downwind advection by the prevailing wind, and also allows for evaporation. The caveats of this model are – the analytical solution was obtainable only for a simplified mountain geometry and many other processes that have been shown to be important in orographic precipitation (such as blocking, modification of the atmospheric flow by latent heating, convective instability, evaporative cooling, valley circulations, and multiphase clouds) are omitted. However the results are especially informative for parameter values which are broadly consistent with case studies of orographic precipitation (e.g., Sinclair 1994; Smith and Barstad 2004). Figure 3 shows the precipitation pattern for standard choices of parameters i.e. mountain height = 2.5 km, mountain width = 60 km, wind speed = 10 m/s, terminal fall speed = 4 m/s evaporation time scale = 2000 sec, growth time = 1000 sec, moisture height scale = 3 km. The pattern shown in Figure 3 is consistent with the typical pattern for orographic precipitation on large mountain ranges.
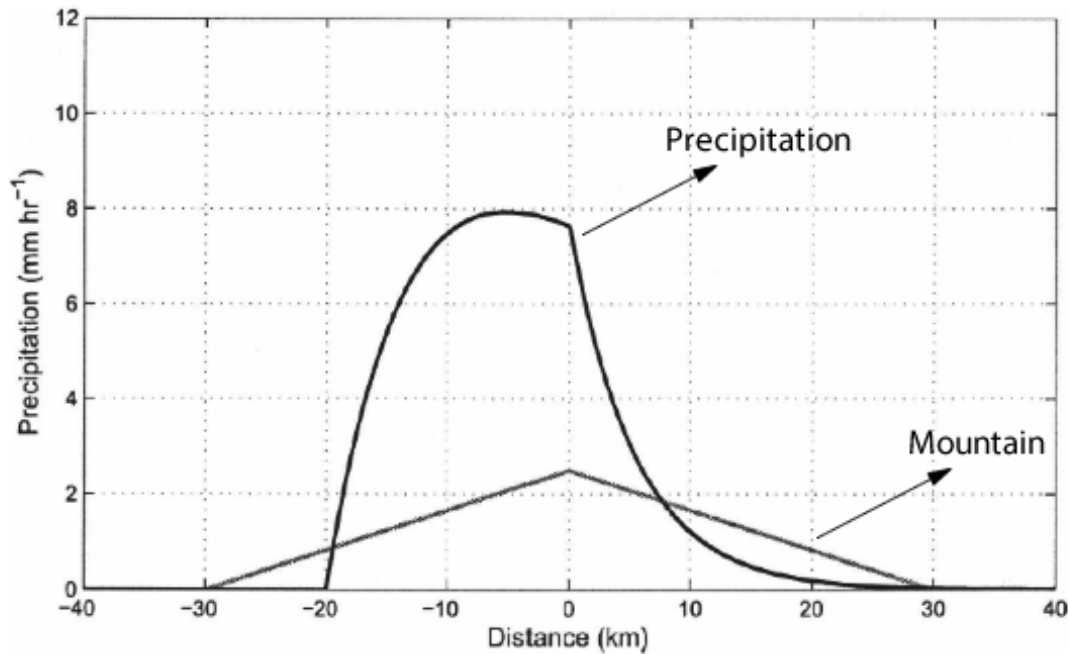
Figure 3: *Precipitation pattern for a standard choice of parameters represented by the analytical model of Roe and Baker (2006).*

There are other similar models which focus on the seeder-feeder mechanism and parameterize the wash-out of droplets (or ice) from the orographic cloud given an imposed large-scale precipitation rate (e.g., Bader and Roach 1977; Carruthers and Choularton 1983; Choularton and Perry 1986) and numerical models that, to varying degrees of complexity, solve for the topographically modified atmospheric flow from the large-scale circulation and include formulations of precipitation formation (e.g, Barros and Lettenmaier 1993; Sinclair 1994).

Diagnostic models are inherently unable to reflect the complexity of the observed transient interactions (mainly due to crude representations of topography), which can involve processes like convection, blocking, and valley circulations. Consequently, we need prognostic models (e.g., GCMs) that will operate in high resolution to include such physical phenomena for better representation of orographic precipitation. There have also been numerous studies about prognostic (numerical) modeling of orographic

precipitation, which includes solving equations of momentum, continuity and energy to simulate moisture advection and precipitation with connection to physical parameterizations. One example is Jiang and Smith (2003), who studied orographic precipitation by analyzing the sensitivity of numerical simulations to variations in mountain height, width and wind speed with emphasis on upslope lifting over isolated mountains in cold climates. They used a mesoscale model which is a 3D non-hydrostatic model solving the full non-linear momentum, continuity, and thermodynamic equations at discrete grid points. Colle (2007) performed 2D numerical simulations with the fifth generation Pennsylvania State University-National Center for Atmospheric research (PSU-NCAR) Mesoscale Model (MM5) to study the impact of multiple mountain ridges on the distribution of precipitation and the simulated microphysics. Miglietta and Rotunno (2009) performed numerical simulations of conditionally unstable flows on mesoscale mountains using a 3D numerical model described in Bryan and Fritsch (2002). The model is designed with particular emphasis on cloud-scale motions and processes, and it was run on high resolution (250 m). They performed the simulations using different values for parameters such as wind speed, mountain height, and mountain half widths. They found that the maximum rainfall rate mainly depends on the ratio of mountain height to the level of free convection, the ridge aspect ratio, and a parameter that measures the ratio of advective to convective time scales.

As indicated in the previous section, this study focuses on the representation of orographic precipitation by CAM Eulerian Spectral Transform and CAM FV dynamical cores. Rasch et al. (2006) compared the tracer transport properties of the Eulerian spectral transform semi-Lagrangian, and FV numerical methods in CAM3 within the Community Climate System Model (CCSM) environment. They found that the FV core is, unlike the Eulerian spectral transform and semi-Lagrangian, conservative and less diffusive, and more accurately maintains the nonlinear relationships (required by thermodynamic and mass conservation constraint) among conserved and non-conserved variables that are influenced by adiabatic and diabatic processes. The relationship between potential

12

temperature to temperature and pressure is an example of such nonlinear relationship. Bala et al. (2008b) investigated the sensitivity of long climate simulations to the CAM Eulerian Spectral Transform and CAM FV dycores and they also analyzed the representation of orographic precipitation by these two dycores. They revealed the positive impact of the CAM FV dynamical core on local processes, especially, the pattern of continental precipitation. Although they found that CAM FV reduced the wet biases in the central Pacific and in the South Pacific convergence zone, the regional land precipitation deficits over the southeast United States, Amazonia, and Southeast Asia, and the excess over central Africa, northern India, Australia, and the western United States (Collins et al. 2006) persisted. Bala et al. (2008a) investigated the realism of both the CAM Eulerian Spectral Transform and the CAM FV precipitation and showed that there are significant differences between two simulations for the western United States in January, where precipitation is dominated by synoptic-scale orographic effects. They concluded that the wet-dry contrast important for regional water resources is better represented with the CAM FV method since they showed that the smaller precipitation features, associated with the Cascades and the Rocky Mountains in the northwest US, were simulated in CAM FV at 1 degree resolution. These features were non-existent for the CAM Eulerian Spectral Transform model, even if the resolution was increased to as high as T239 spectral truncation (Iorio et al. 2004).
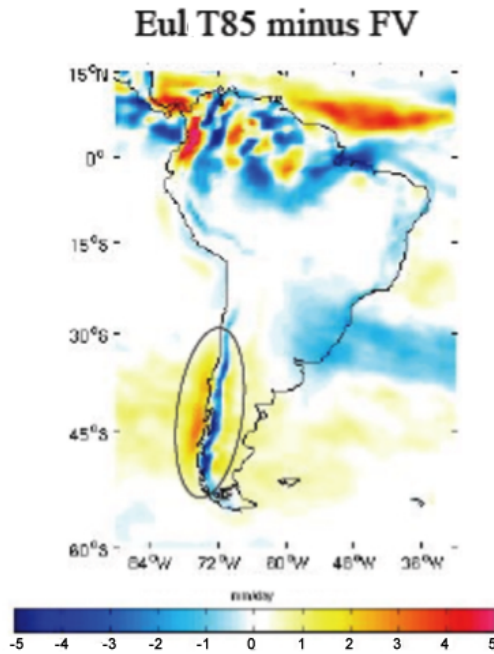
Figure 4*: July mean precipitation rate difference between the CAM Eulerian Spectral Transform and CAM FV simulations. The ellipse indicates the Andes mountain regions where a clear difference between CAM EUL and CAM FV orographic precipitation exists.*

Figure 4 shows the 1991 July mean precipitation rate difference between the CAM EUL T85 and CAM FV 1 degree simulations over the South American Andes. Over the mountain ranges the difference is negative meaning that the CAM FV model predicts higher values in that region, while EUL spreads precipitation over a wider range in the east-west direction, thus over-representing the precipitation amount where it should be less. This difference over the mountain is due to the high peak precipitation simulated by CAM FV as a result of orographic lifting. This upslope mechanism has been confirmed as the most typical cause of orographic precipitation by previous studies (Jiang and Smith 2003; Roe 2005; Roe and Baker 2006) as shown in Figure 3. Williamson and Rasch (1994) proposed the following mechanism for the over-representation of precipitation in spectral transform models: (1) one fundamental disadvantage of the spectral models is that they create negative values for tracers (such as water vapor), thus a negative filler is required to obtain realistic results. The negative values in a region are filled to zero,

which can result in an increase in the local area average; (2) the spectral advection (truncation) then re-introduces oscillations with positive values overshooting local saturation, and zero values again becoming negative; (3) the supersaturated areas are then returned to saturation through stable condensation. The process is then repeated. This mechanism provides a path for computational transport into regions of small water vapor and then condensation.

The results of the previous studies suggest that the formulation of the dynamical core can have a direct effect on the representation of processes that are normally viewed as controlled by the physical parameterizations, and it is the local details of the interaction of the synoptic waves and topography which are important to the morphology of precipitation. We aim to investigate the representations of such features of large-scale, topographically enhanced precipitation and thus the realism of different models. We introduce the concept of "meteorological realism" that is, do local representations of large-scale phenomena by GCMs look like the observations? The next section discusses the essence of such concept and previous studies about the validation of GCMs in order to check their realism.

1.3. Meteorological Realism: Connecting Theory, Observations and Simulations

Many aspects of climatology and meteorology involve the need to assess the differences between model-generated spatial fields and/or to compare model and observed fields. Gates (1992) states that a comprehensive atmospheric model validation program includes examination of not only the mean and variance, but of the complete frequency distribution. Moreover, in addition to the primary dynamical and physical variables, the derived quantities associated with fluxes and processes and the occurrence of specific events should also be evaluated. These assessments are essential to validations

of GCMs, because to improve such models, the reasons of biases should be discovered. Airey and Hulme (1995) state two ways to achieve this goal. First is to evaluate versions of the same GCM where just one change to the model has been made between versions. However this approach is problematic since more than one change is made from one generation of a model to another, thus it is hard to isolate the real source of the difference between two versions. Therefore, it is often more practical to use a second method where observed and modeled fields are compared. This second approach is what we base our notion of meteorological realism on.

Meteorological realism combines our theory-based mechanistic understanding of a meteorological feature, with weather-scale observations describing the feature, and the morphology of how models represent the feature. To introduce this notion, we look at the 21-year (1979-2000) January mean precipitation of two configurations of the Community Atmosphere Model (Bala et al. 2008b) over our study domain (Figure 6). Our study domain (Figure 5) is the North American West Coast (20-65 N, 200-260 W) and we specifically focus on the topography of the Coast Range and the Sierra Nevada (red rectangle in Figure 5). The highest point in the area is Mount Whitney in the Sierra Nevada with an elevation of 4,421 m and the average width of the mountains is 105 km (including the valley between the mountains).
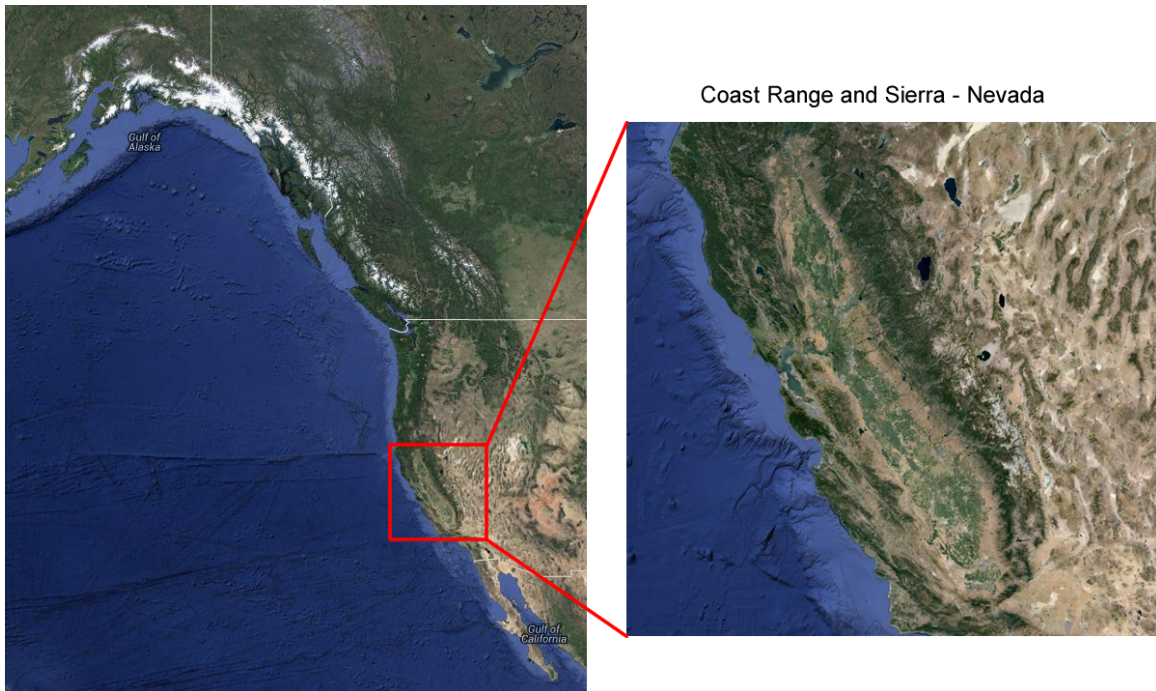
Figure 5: *The study domain (North American West Coast 20-65 N, 200-260 W, left) and California showing the Coast Range, the Central Valley and Sierra Nevada Mountains (right).*

The configurations of the model differ by the dynamical core with one configuration using a CAM FV dynamical core and the other using a CAM Eulerian Spectral Transform dynamical core.
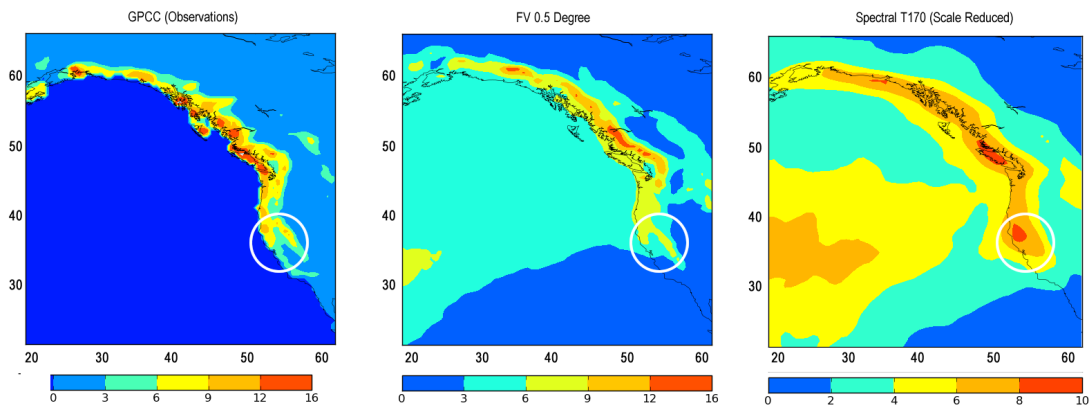
Figure 6: *1979-2000 long-term mean precipitation (mm/day) plots of Global Precipitation Climatology Centre (GPCC-observations) (left), FV 0.5 degrees model (middle) and Eulerian Spectral T170 model (right) run with CAM3 (Bala et. al., 2008).*

The CAM FV model and GPCC observations in Figure 6 have ~0.5-degrees horizontal resolution and CAM Eulerian Spectral Transform model has T170 (~0.7-degrees) triangular truncation. The AMIP runs for the CAM Eulerian Spectral Transform model produced relatively less precipitation on the North American West Coast when compared to the CAM FV and the GPCC observations. Therefore, the color scale of the CAM Eulerian Spectral Transform model plot is reduced in order to show the structure and the spatial orientation of the precipitation features better. The observations in Figure 6 are limited to land. The observed precipitation is concentrated on the coastline, and closely linked to the mountain ranges on the western edge of the continent. Examination of the observations shows similarities with the simple description of orographic precipitation in Figure 3. The rain is on the windward side of the mountains, associated with the moisture flux from the west. To the eastward (leeward) side of the mountains there is a rain shadow. The rain shadow is observed in both the Central Valley of California and to the east of the Sierra Nevada. In much of the western US, the land to the east of the mountains is semi-arid or desert.

Comparing the model simulations in Figure 6, there are qualitative differences. Both simulations show precipitation near the coast. The CAM Eulerian Spectral Transform simulation is spread out spatially (similar to what is observed in Figure 4), notably in the east-west direction. Focusing on the area inside of the white circle the observations show a distinct line of precipitation, which aligns with the westward side of the Sierra Nevada. This is reproduced in the CAM FV simulation, but is less distinct in the CAM Eulerian Spectral Transform dynamical core. To the east of the Sierra Nevada, the observations and CAM FV simulation are drier than the CAM Eulerian Spectral Transform simulation.

If we examine orographic precipitation at smaller scales (Barros et al. 2004) we find organized structure on a finer scale. There are sensitivities due to the structure of the mountains, for example, moisture flux convergence/divergence, small-scale wind circulation, and different convection characteristics at different locations. These features aggregate to form the features that we observe in the larger scale. Consequently, in order to verify meteorological realism, we need to recognize these processes at different scales and examine how models represent these scales as spatial resolution increases. The presence of small-scale structure in weather observations provides powerful information on model performance that is both quantitative and qualitative. For example, in Figure 6 the structure of the precipitation in the FV model aligns with the underlying topography in a way similar to the observations and appears "more realistic." We strive to bring quantitative descriptions to this realism, and how it changes as a function of resolution.

There are a number of phenomena that numerical schemes represent with distinct visual differences. Fronts and rain bands in hurricanes are examples, where numerical schemes designed to preserve strong gradients, like the FV scheme, make an obvious difference. Measures of fit, such as comparisons with observations of mean and variance, may not distinguish these qualitative measures of realism with robustness. We recognize some attributes that describe meteorological realism. First, there is consistency with heuristics, e.g. Figures 2 and 3, which are often at the foundation of the intuition developed by weather forecasters. Second, there is the notion that rather than the simulation simply comparing well with, for example, the mean cell value of the observations, the simulation is a composite of smaller scale processes as is the case in nature.

With a focus on features, which we will define as objects, such as the precipitation field in Figure 6, fronts, rain bands, clouds in deep convection etc. (Xu et al. 2005), and the recognition that these are composed of clusters of small-scale processes, we assert that we can develop strategies to bridge the evaluation of weather and climate models.

These features are "weather," and weather features are represented in climate models. The dynamics of the weather features organize the flow and, hence, precipitation. A focus of these as objects and how the objects relate to simulated and observed underlying structure allows us to look at like features in models and observations and supplements the grid-level comparisons (Gates et al. 1999; Notaro et al. 2007; Preisendorfer and Barnett 1983; Santer and Wigley 1990; Santer et al. 2009) that are exemplified by many forecast evaluation techniques. The next section gives general information about object-based analysis, the previous studies about its application on weather and climate modeling (Section 1.3.1). Our object-based approach to the problem of bias quantification for GCMs is detailed in section 1.3.2.

1.3.1. Object-based Analysis

Douglass (2000) defines an object as a cohesive entity that has attributes, behavior, and (optionally) state. Objects may represent real world entities (sensors, engines etc.), purely conceptual entities (bank accounts, marriages etc.), or they can be visuals (histograms, circles etc.). For example, a real world entity might be a sensor that can detect and report both a linear value and its rate of change, so the sensor contains two attributes: the monitored sensor value and its computed rate of change. The object state consists of the last acquired/computed values and the object behavior includes actions such as acquisition, reporting, enabling, disabling. In our study, an object can be viewed as a visual entity i.e., the precipitation features. In an object-based analysis, the various concepts inherent in the various domains of concerns are identified, along with their relations to each other. There are two primary aspects of object-based analysis: structural and behavioral.

- *Object structural analysis* identifies the key abstractions of the application that are required for correctness, as well as the relation that links them together.
- *Object behavioral analysis* identifies how the key abstractions behave in response to environmental and internal stimuli.

As explained in the meteorological realism section, the effect of internal and environmental stimuli (i.e. the underlying physics of precipitation and the effect of topography) should be incorporated as some sort of an object behavioral analysis in model verification.

Object-based techniques are relatively scarce in the climate model verification studies (Posselt et al. 2012; Skok et al. 2013); however they have been used in the field of weather prediction. These techniques aim to fit the predictions to the observations, and the measure of this fit indicates how well the forecasts represent the observations (Gilleland 2013; Gilleland et al. 2009). Next we review the important studies among the object-based studies of weather forecast verification as they can be easily linked to an object-based approach regarding GCM verification.

Distortion representation of forecast errors (Hoffman et al. 1995) is accepted as a landmark study since it is an important step towards an object-based verification approach. In its simplest form, the approach of Hoffman et al. (1995) decomposes the forecast error into a part attributable to displacement errors and a residual. They define displacement as a smooth transformation of a meteorological field without any amplification (a smooth translation being any combination of translation, stretching, and rotation without tearing). Errors due to amplification can also be included as large-scale errors like displacement. The idea of the study is that the removal of these large-scale errors from the total forecast error will lead to the remaining residual errors being much closer to the "ideal". In mathematical terms, if X is a meteorological variable, then for a simple displacement:

$$X_d(r) = X_f(r') \tag{1}$$

where X_d is the distorted variable due to displacement and amplification, X_f is the same forecast variable, r is the original location of the variable (as a meteorological field) and r' is the location of the displaced field, which can be obtained by a displacement function D i.e.:

$$r' = D(r) \tag{2}$$

The essence of the method is to choose $D(r)$ to optimize some goodness of fit criterion using, for example, standard minimization algorithms. If the displacement and amplification are assumed to be constant over the entire domain, they can be determined by minimizing the root mean squared (RMS) error or maximizing the correlation coefficient between the corrected forecast and the verifying analysis.

Ebert and McBride (2000) used this approach to determine the systematic errors of numerical weather prediction models in terms of their representations of precipitation. They applied an object-based method in which they defined a contiguous rain area (CRA), which is the area of contiguous observed and/or forecasted rainfall enclosed within a specified contour. A CRA can be regarded as the union of the forecasted and observed rain entities. An example of such CRA is given in Figure 7:
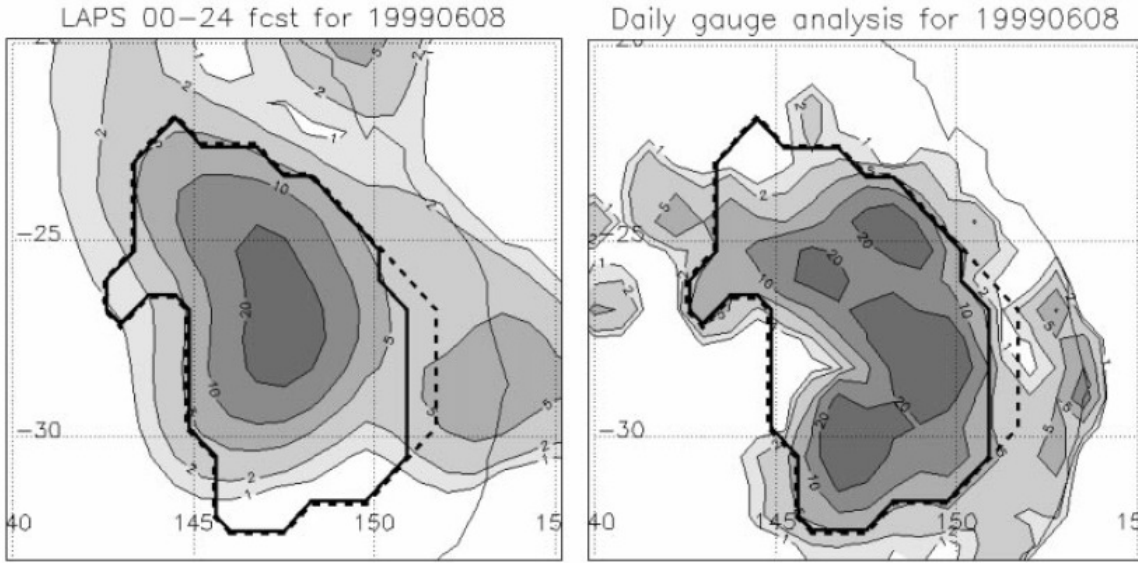
Figure 7: *Rain system in eastern Australia for June 8, 1999 represented by Australian Bureau of Meteorology's Limited Area Prediction System (LAPS) (left), and daily gauge analysis (right). The heavy line shows the boundary of the original CRA. The dashed line shows the verification domain, in which the original CRA is extended to include the shifted forecast rain entity (Ebert and McBride 2000).*

The heavy line in Figure 7 indicates the boundary of the CRA using a threshold of 5 mm/day to isolate the storm of interest. The displacement error is determined by incrementally moving the forecast field over the observed field until a best fit criterion is optimized (which can be minimization of the RMS error or maximization of the correlation coefficient as indicated in Hoffman et al. (1995). The verification domain is shown by the dashed line, which was obtained when the forecast field was moved two grid points in both southward and eastward directions. This shift is analogous to the $D(r)$ in equation 2.

Following the identification of the CRA as an object, the verification is done according to the Hoffman et al.'s (1995) approach, i.e. the total mean squared error (MSE) is partitioned as:

$$MSE_{total} = MSE_{displacement} + MSE_{volume} + MSE_{pattern} \qquad (3)$$

23

After calculation of the displacement, the forecast rain is shifted to a position of zero displacement and MSE$_{\text{shift}}$ is calculated. Then:

$$\text{MSE}_{\text{displacement}} = \text{MSE}_{\text{total}} - \text{MSE}_{\text{shift}} \tag{4}$$

and

$$\text{MSE}_{\text{pattern}} = \text{MSE}_{\text{shift}} - \text{MSE}_{\text{volume}} \tag{5}$$

Although this verification approach explicitly identifies the pattern error in an objective sense, it still crunches the pattern difference between the forecast and the observation to a single number. The other caveat of this approach is the statistical significance. In their study, Ebert and McBride (2000) conducted a Monte Carlo simulation to test the robustness of the method and found out that the number of observations within a CRA (i.e., the number of grid points) should be at least 20 in order for results to be significant. This is problematic for orographic precipitation as some of the objects we aim to identify in this study are small-scale features that include fewer than 20 grid points.

Baldwin et al. (2002) developed an "events-oriented" approach assigning a set of attributes to an event. For this purpose they defined an attribute vector (f_i for a forecast event and o_i for an observed event):

$$f_i = (\propto_i, \beta_i, \dots, x_i, y_i)^T \tag{6}$$

where x_i and y_i are the attributes associated with the spatial location of this event, and $\propto_i, \beta_i$ are attributes that are related to the characteristics of the event such as location, shape, scale, amplitude, orientation, continuity etc. Once the vectors are constructed,

24

similarity measures can be calculated, such as correlation coefficient, for verification purposes. As an application of such approach, Baldwin and Lakshmivarahan (2003) combined objective attribution of forecast events with a subjective classification where they first visually defined different modes of convection as stratiform, linear and cellular from 1 hour accumulated rainfall analyses obtained from the NCEP " Stage IV" (Lin and Mitchell 2005) analysis system. Then objective methods for such classification were conducted and were compared to initially classified events. They first employed hierarchical cluster analysis, which proved efficient in differentiating between stratiform and linear/cellular events. However, it couldn't effectively classify the convective events into linear and cellular events separately. This was due to the fact that the attributes were only able to describe the overall distribution of rainfall across the region but not able to more specifically describe how rainfall were organized spatially. As the second step, geostatistical methods were used to identify such spatial attributes. For this purpose they plotted 2D semi-variograms, correlograms and covariance plots to obtain a measure of spatial continuity from which the extracted the spatial attributes. Then, using these new attributes hierarchical clustering was applied again as a result of which they obtained 75% correct classification. More local information is needed to improve the classification efficiency.

In another study, Marzban and Sandgathe (2006) used cluster analysis to identify features of precipitation in forecast and observation fields. They used the iterative clustering as a means of scale analysis, in other words every iteration agglomerates grids into bigger clusters thus at the initial iteration it addresses individual grid points and the whole field is treated as a single event at the final iteration. This allows different number of clusters to be treated as different scales, however, smaller or larger clusters don't necessarily mean different scales in precipitation events as the method can agglomerate smaller scale events into bigger ones as the iteration number increases. One strength of this method is the possibility of application over varying number of parameters. Clustering can be applied to spatial coordinates only (latitude and longitude) which will

assess the agreement between the two fields in terms of the size, shape and displacement, or it can be applied to latitude, longitude and precipitation, which will assess the sum of all errors including the precipitation amount. The verification measure Marzban et al. (2006) used was the distance between the clusters either when they are matched between forecast and observation after every iteration, or the average of the distances between matched clusters, which again suffers from the loss of information inherent to different precipitation events (local bias).

Micheas et al. (2007) combined the idea of an attribute vector for an event, with decomposition of forecast errors (Hoffman et al. 1995). They introduced a verification scheme that uses shape analysis by identifying precipitation objects and assigning attributes through a number of angular components that specify the shape of the object. Each forecast model (say there are M number of models under analysis) is described as a collection of N_i cells, which correspond to objects. Each cell is described by an attribute vector such as:

$$S_{ij} = (c_x^{ij}, c_y^{ij}, c_{min}^{ij}, c_{max}^{ij}, c_{avg}^{ij}, r_{\theta_0}^{ij}, \dots, r_{\theta_{A-1}}^{ij}) \tag{7}$$

where c_x^{ij}, c_y^{ij} defines the centroid of the cell (location), $c_{min}^{ij}, c_{max}^{ij}, c_{avg}^{ij}$ defines the minimum, maximum and average value attained by the cell respectively, and r_θ^{ij} which gives the radial distance from the centroid to the edge for various angles for j=1,2,..,N number of cells and i = 1,2,..,M number of models. A similar vector is constructed for observations too and each cell was forced to match between models and observations based on either their location (centriod based), or their shape differences (Procrustes matching). Procrustes approach (Dryden and Mardia 1998) was used in order to capture shape variation (translation, dilation and rotation). As a result, they obtain sum of squares (SS) measures such as SS$_{shape}$, SS$_{avg}$, SS$_{min}$, SS$_{max}$, SS$_{location}$, SS$_{rotation}$, SS$_{scale}$. Consequently, the decomposition of errors is even extended to other parameters such as

scale and rotation, however the averaging inherent to the sum of squares measure still persists.

Davis et al. (2006) developed a different method for identification of precipitation events as objects, with emphasis on how to match the objects correctly between models and observations. Their method starts with convolution of the original field (Figure 8a) with an appropriate shape, such as a cylinder. The convolution replaces the precipitation value at a point with its average over the area within a disk whose centroid is located at that point (Figure 8b). The convolution step is for smoothing purposes, which allows the precipitation to be thresholded and masked in order to obtain the rain areas. Thresholds can be tuned to distinguish rain areas of greater size and intensity from those that are weaker and more isolated. The result of thresholding is a mask that has only rain areas, and 0's otherwise (Figure 8c). Then the precipitation values over the rain areas are replaced by the values of the original field to retain precipitation features as objects.
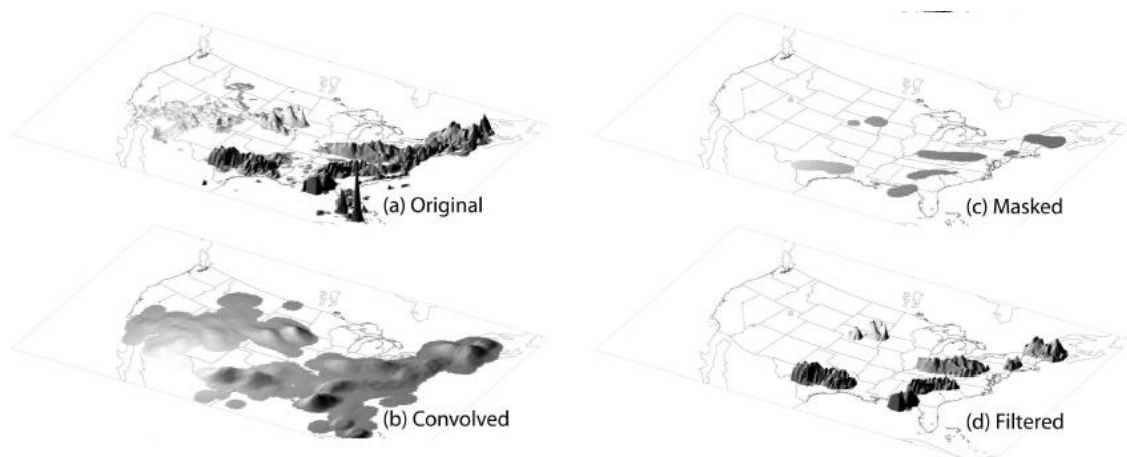
Figure 8*: Example of application of approach to a particular Weather Research and Forecasting (WRF) model precipitation forecast grid: (a) original precipitation field; (b) convolved field; (c) masked field; and (d) filtered grid, showing the precipitation intensities over the rain areas. The grid covers the entire United States. (Davis et al., 2006)*

Each identified object is assigned various properties (analogous to the attribute vector of Baldwin et al. (2002)) such as intensity, area (object size), centroid, axis angle (object alignment), aspect ratio, curvature (obtained by fitting a circular arc to the object). The objects are then matched (between observations and models) based on the distance between their centroids, namely the separation between the centroids of the two objects should be less than their sizes. This study touches the climatology analysis by examining the objects without matching them, which is claimed to indicate systematic model errors. One approach is to plot the histograms of sizes of the unmatched objects within each model, for every model time. This approach can give an overall behavior of the modeled precipitation however; as described earlier, there are important local biases in the models information about which would be lost in such approach. In the same histogram analysis, it was also observed that there were peaks in histograms (i.e. the points corresponding to object size of about 200 km), which was attributed to be an exaggeration to the smoothing inherent in the convolution process. It was also stated that when examined on a finer grid, no peak was evident. This is a weakness in terms of object identification, as we need a robust method that would be resilient to model resolution so that the effect of resolution can be quantitatively documented.

Wernli et al. (2008) adopted a different approach to computation of object statistics in which they included three components namely structure (S), amplitude (A), and location (L) of the precipitation domain. The method does not require one-to-one matching between the identified objects. The amplitude measure does not deal with individual objects but corresponds to the normalized difference of the domain-averaged precipitation values. The location component consists of two parts, first one being related to the normalized distance between centers of mass of the modeled and observed precipitation fields, second one considering the averaged distance between the center of mass of the total precipitation fields and individual precipitation objects. The basic idea of the structure component is to compare the volume of the normalized precipitation objects. This approach takes the decomposition of forecast errors one step further,

however, it still suffers from extensive averaging of precipitation fields and especially structure comparison since volume does not necessarily give information about the shape of the objects, especially when dealing with small-scale events such as orographic precipitation.

For climate model validation, Xu et al. (2005) used such objective classification technique that uses satellite data to classify distinct "cloud objects" defined by cloud-system types, sizes geographic locations, and matched large-scale environments. They identified a cloud object as a contiguous region of the earth with a single dominant cloud-system type by using a region growing method dependent on selection criteria. The statistical properties of the identified cloud objects were analyzed in terms of their probability density functions based upon the satellite data. This method enhanced the ability to study the cloud feedback processes directly for a single cloud-system type, as opposed to the multiple cloud-system types that are often simultaneously present in a fixed region of the earth using monthly, seasonally, or yearly averaged satellite/surface data.

As a summary of the previous model verification studies, it can be concluded that the efforts can be considered in two groups:

- Identification/Isolation of the features of a meteorological field (hereafter referred to as identification)
- Subsequent verification of the identified features by comparison between model and observations (or between two models).

The previous studies focus intensively on the identification part of the problem either by using known statistical methods (such as cluster analysis used by Marzban et al. (2006)) or developing new techniques as Davis et al. (2006) did with convolution of precipitation fields. Studies show that the identification task is well accomplished using different methods, however the scales of the identified features is still problematic and still needs subjective input according to the nature of the problem (i.e., how to define

29

features). Thus our aim is to apply suitable methods to better identify the precipitation features that will especially work well on the smaller scale events. The verification part of the problem, as indicated numerous times in our review of previous studies, has not been a focus as much as identification and is still problematic in terms of an object based comparison. Still the most popular verification methods use RMS or correlation coefficient. Although Hoffman et al.'s (1995) approach of error decomposition is somewhat expanded by some following studies (i.e., Ebert and McBride (2000), and Micheas et al. (2007)) they still suffer either domain averaging or averaging between matched objects like. Our aim is to move to a different direction in the verification task by looking at the errors arose from pre-specified objects that carry important local information. This can require subjective input since the problem under investigation (orographic precipitation) has characteristic behavior in terms of its features, however once they are defined; the method can be evolved into a more objective approach. In most of the previous studies, the methods used in both the identification and the verification parts do not include multivariability with other parameters (in our case moisture flux and topography). Since we aim to link the local biases to underlying physics, we aim to develop quantitative methods that will investigate the effects of the physics on the orographic precipitation both in an objective and subjective way. The next section details how we approach to address these issues in the context of an object-based approach.

1.3.2. An Object-based Approach for Bias Quantification of GCMs

As indicated previously one of the objectives of this study is to develop an object-based framework to be applicable to a variety of scales of orographic precipitation simulation by GCMs. Our object-based approach can be detailed in three main steps:

1. Characterization of the representation of orographic precipitation by GCMs

30

2. Linking the representation of orographic precipitation to GCM structure

3. Identification and evaluation of the orographic precipitation features

Characterization of the representation of orographic precipitation by GCMs is the initial step to quantify the biases of GCMs to understand how weather phenomena are represented. This step involves finding features of similar origin and location, but simulated differently by different models (which we label as study features). The reasons for such difference are challenging underlying conditions (e.g. topography). These features should be reproduced over progressive simulation steps in order to be considered "study features" and they give valuable information about the artifacts of the models. This identification task consists of both subjective (theory of orographic precipitation) and objective input. The 21-year (1979-2000) January mean precipitation of two configurations of the Community Atmosphere Model exhibits such features (Figure 6).

The area in Figure 6 (white circle) is the California Coast Range and the Sierra Nevada Mountains with the Central Valley in between (Figure 5). In this region, the rain shadow is observed in both the Central Valley and to the east of the Sierra Nevada. The Coast Range provides the orographic lift to the impinging moist air leading to precipitation. As a result of the smaller scale dynamical and physical mechanisms taking place in between two mountain ranges, the remaining moisture (if any) undergoes a second lift over the Sierra Nevada, which is on average higher than the Coast Range. The CAM Eulerian Spectral Transform dynamical core in Figure 6 created a big blob of precipitation with the precipitation over the mountain ranges combined into a single large precipitation feature. On the other hand, the CAM FV model produced a narrow band of precipitation over the mountain range with a higher peak value (10 mm/day) than that of the CAM Eulerian Spectral model (8.5 mm/day). This "spread out" effect in the CAM EUL model is also observed in Figure 4. The precipitation feature produced by the CAM FV model visually represents the observations better than the CAM EUL model. The monthly mean plots (not shown) illustrate that this type of behavior for CAM FV and CAM Eulerian Spectral Transform models is typical throughout the 21-year period. As a

31

result, relating back to our definition of a study feature, the precipitation over the Coast Range and Sierra Nevada is a good candidate for further analysis.

Linking the representation of orographic precipitation to GCM structure is the second step after characterization of the features of interest. This is achieved by setting up idealized GCM runs to provide analogues to the features to be investigated. For this purpose, we implement a modification to the mountain Rossby wave test case (Jablonowski et al. 2008) to create suitable conditions of wind, moisture flux and topography. The simpler -and controlled- experiments reveal relationships between the simulation of orographic precipitation and the components of GCMs:

- Which model part shapes the appearance of orographic features of interest?
- What causes the difference of these features of interest between FV and Spectral dynamical cores?
- How do these features of interest evolve with increasing resolution and why?

Identification and evaluation of the orographic precipitation features is the last step to quantify the simulation differences of these study features. Each feature is defined as an object based on their inherent characteristics such as size, magnitude, alignment etc. Pattern recognition techniques are employed to classify and isolate the objects. Once the objects are isolated, they are subjected to comparison as a statistical verification process (simple statistics as well as geostatistical measures) in order to quantify differences.

Section 2 involves the discussion of the results of the application of this three-step approach. The first step (Characterization of the representation of orographic precipitation by GCMs) is already concluded as we selected our study features over the Coast Range and Sierra Nevada (Figure 6). The second step of the approach is explained and its results are discussed in chapter 2, where we link the representation of the selected study features to GCM structure by creating simplified test cases that resemble the conditions over Coast Range and Sierra Nevada. In chapter 3 the first part of the

identification and verification task (3rd step of our approach) is discussed. We start this task by application of k-means clustering (for object identification) and geostatistics (for object comparison and evaluation) to the monthly mean precipitation results from the idealized test cases. In chapter 4 we add the time dimension to our analysis and quantify the daily precipitation results using a pattern recognition method (classification trees). We also examine the grid scale variability of both CAM Eulerian Spectral and CAM FV models in their simulation of orographic precipitation in the idealized test cases. Finally, chapter 5 summarizes the findings from our object-based approach and gives the conclusions of this study.

CHAPTER 2: IDEALIZED SIMULATIONS: Linking the Representation of Orographic Precipitation to GCM Structure.

The idealized simulations are the second step of our object-based approach and link the representation of orographic precipitation in the Atmospheric Model Intercomparison Project (AMIP) runs given in Figure 6 to GCM infrastructure. The two dynamical cores under analysis, namely CAM FV and CAM Eulerian Spectral, were run in two different resolutions for each dynamical core i.e. 1 degree and 0.5 degrees for CAM FV, T85 and T170 for CAM Eulerian Spectral. The two dynamical cores were coupled with a reduced moist parameterization suite (hereafter "simple physics") that was used to test the simulation of tropical cyclones by GCMs and the effect of the dynamical core (Reed and Jablonowski 2012). CAM allows us to couple a simpler version of physics parameterization with a dynamical core in order to assess the capabilities of each dynamical core and compare them to each other in terms of simulation of orographic precipitation. The simple-physics suite allows physical processes that are important for orographic precipitation such as large-scale condensation defined to occur when the atmosphere becomes saturated, surface fluxes of horizontal momentum, evaporation, and sensible heat, boundary layer turbulence of horizontal momentum, temperature, and specific humidity. The surface flux of evaporation especially is an effective process in creating precipitation over the mountains. Because our test cases are on an aquaplanet setting (Neale and Hoskins 2000), the mountains are covered with water and this leads to the reinforcement of the moisture in the lower atmosphere via surface fluxes. This is analogous to a well-known phenomenon called precipitation recycling which is the contribution of evaporation within a region to precipitation in that same region (Bosilovich et al. 2003; Eltahir and Bras 1996). This is observed in all cases in this study and gives valuable insight as to how it is simulated by different dynamical cores with varying resolution. All experiments were conducted using 26 hybrid vertical model levels. The physics and dynamics time steps for the CAM Eulerian Spectral model are

identical, and are 1800 and 300 seconds for T85 and T170 respectively. For the CAM FV model, the physics time steps are 1800 and 600, and the dynamics time steps are 180 and 60 seconds for 1 and 0.5 degrees respectively. The total model run is for 30 days.

2.1. Test Case Setup

The initial conditions are similar to the mountain-induced Rossby wave train test case (Jablonowski et al. 2008), which are similar to initial conditions by Tomita and Satoh (2004). The main difference is the derivation of the surface pressure for hydrostatic conditions. The simulation starts from smooth isothermal initial conditions that are a balanced analytic solution to the primitive equations.

The horizontal wind components are prescribed as:

$$u(\lambda, \phi, \eta) = u_0 \cos \phi \tag{8}$$

$$v(\lambda, \phi, \eta) = 0 \ m \ s^{-1} \tag{9}$$

where λ, ϕ, η are longitude, latitude, and hybrid model level respectively, and u_0 is constant 20 m/s for all experiments. The meridional wind is set to zero initially. The experiments were run on an aquaplanet setting where the isothermal surface temperature was taken as 288K. This yields the constant Brunt-Väisälä frequency (N) of 0.0182 s^{-1}. The vertical temperature profile is also isothermal thus the atmosphere has zero lapse rate. The waves are triggered by idealized Gaussian-bell shaped mountains. The mountains induce the disturbance to the initial conditions to create baroclinic waves in the leeward side. The idealized Gaussian-bell mountain is introduced via surface geopotential (Φ_s):

$$\Phi_s(\lambda, \phi) = gz_s = gh_0 exp[-(r/d)^2] \tag{10}$$

where g is the gravitational acceleration, z_s is the surface height, h_0 is the peak height of the mountain and d is the half width of the Gaussian mountain profile. r is defined as the great circle distance:

$$r = a \ arccos[sin\phi_c \ sin\phi + cos\phi_s cos\phi cos(\lambda - \lambda_c)] \tag{11}$$

where a is Earth's radius, ϕ_c and λ_c are center points in latitude and longitude respectively. The mountain specifications for each setup are given in Table 1.

Table 1: The mountain specifications for 3 experimental setup cases.

Case #	Center Point in Longitude (λ_c)		Center Point in Latitude (ϕ_c)		Peak Height (h_0) (m)		Half Width (d) (km)	
	1st Peak	*2nd Peak*	*1st Peak*	*2nd Peak*	*1st Peak*	*2nd Peak*	*1st Peak*	*2nd Peak*
1	97° E	-	30° N	-	1500	-	1500	-
2	90° E	97° E	30° N	30° N	1500	1500	1500	1500
3	90° E	93° E	30° N	30° N	500	3000	500	500

The test cases are set up to progress from simple towards more complex to observe the evolution of complexity in the simulation of orographic precipitation by different models. The first case with a single mountain represents stable upslope ascent precipitation on the windward side of the mountain as well as the rain shadow on the leeward side. The baroclinic waves induced by the mountain also create precipitation after some distance. The second case has a second mountain peak in front of the first one to observe the smaller scale dynamics and the distribution of precipitation between the two peaks. The third ("realistic") case contains two mountains resembling those of the Coast Range and the Sierra Nevada. As can be seen in Table 1, cases 2 and 3 have two

mountains in their setups and case 2 is labeled as "double mountain", however case 3 is labeled as "realistic" for clarity due to its resemblance to the Coast Range and Sierra Nevada.

The surface pressure field balances the initial conditions. For hydrostatic primitive equation models it is defined as:

$$p_s(\lambda, \phi) = p_{sp} \, exp\left[-\frac{a \, N^2 u_0}{2 \, g^2 \, \kappa}\left(\frac{u_0}{a} + 2\Omega\right)(sin^2\phi - 1) - \frac{N^2}{g^2 \, \kappa}\Phi_s(\lambda, \phi)\right] \tag{12}$$

where κ is the ideal gas constant for dry air (R_d) divided by specific heat at constant pressure (c_p) and is 2/7, $\Omega = 7.29212$ x 10^{-5} s^{-1} (Earth's angular velocity), p_{sp} denotes the surface pressure at the South Pole which is set to 930 hPa. The moisture, which triggers the orographic precipitation, is initialized via specific humidity calculated as:

$$q = \frac{q_0 \times p}{p_{s,0}} \tag{13}$$

where q is the specific humidity, p is pressure, $p_{s,0}$ is a reference surface pressure (1000 hPa) and q_0 is the specific humidity at the surface when the relative humidity equals 80%.

2.2. Discussion of Idealized Test Case Results

2.2.1. Case 1 "Single Mountain"

Figure 9 shows the surface geopotential overlaid by 30-day mean precipitation for CAM Eulerian Spectral T85 and T170, and CAM FV 1 and 0.5 degrees resolutions.
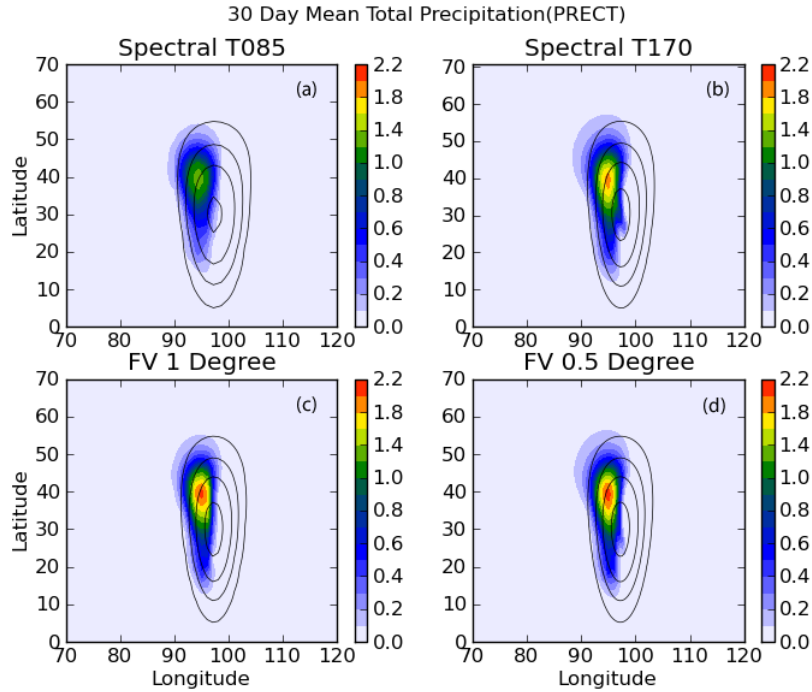
Figure 9: *30 day mean total precipitation rate (mm/day), surface geopotential for case 1 of experimental test cases, simulated by (a) CAM Eulerian Spectral T85, (b) CAM Eulerian Spectral T170, (c) CAM FV 1 degree, and (d) CAM FV 0.5 degrees.*

Surface geopotential contours (topography) are 500, 2.000, 5.000 and 11.000 $m^2 s^{-2}$ throughout all plots. Stable upslope ascent precipitation features are observed in all simulations on the northward and windward side of the mountains. The large-scale precipitation is initiated at the start of the simulation, moves northward, and loses intensity as the simulation continues. The intensity of the precipitation feature simulated by CAM Eulerian Spectral T85 is significantly lower than that of other models. This is mostly due to the spectral filtering applied to the topography, the effect of which will be discussed in the next section (case 2). The intensity for CAM Eulerian Spectral T170 is lower than that of both CAM FV models. The simulation is almost identical for CAM FV 1 and 0.5 degrees resolutions in terms of both the shape and the intensity of the features. This difference in intensity between CAM Eulerian Spectral and CAM FV models was

observed in AMIP runs (Figure 3). This idealized simulation also indicates the high
sensitivity to resolution for spectral models.

Examining the daily precipitation plot (Figure 10) reveals information about the types
of simulated features, some of which are not apparent in the monthly mean plot.
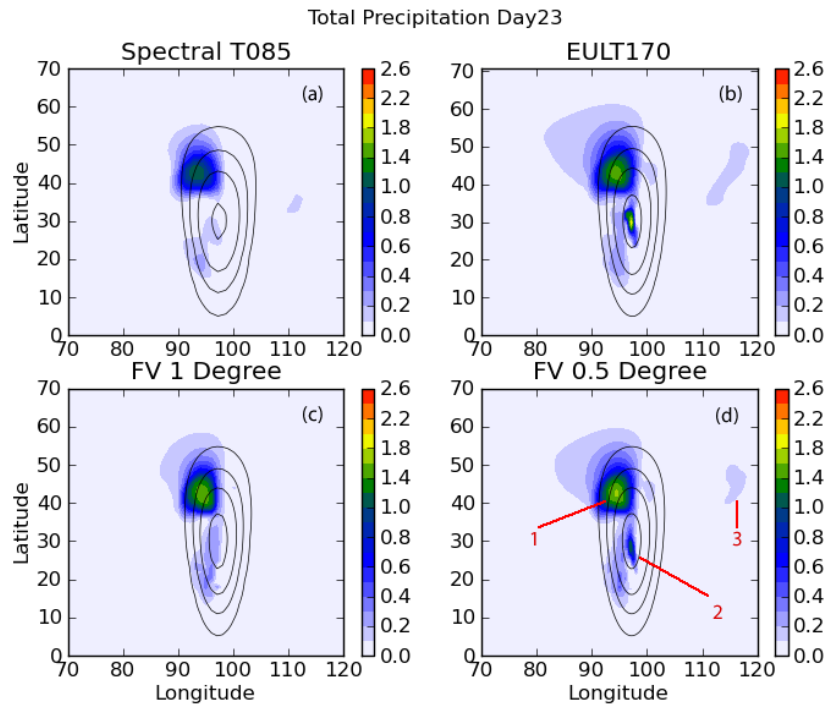
Figure 10: *Day 23 total precipitation rate (mm/day), surface geopotential for case 1
simulated by (a) CAM Eulerian Spectral T85, (b) CAM Eulerian Spectral T170, (c) CAM
FV 1 degree, and (d) CAM FV 0.5 degrees. Day 23 is selected due to the explicit
appearance of the features of interest.*

These features (as indicated by their corresponding numbers in Figure 10d) are:

1. Large-scale features due to stable upslope ascent
2. Small-scale features due to local evaporation and lee-side convergence
3. Feature due to leeward baroclinic waves

39

The picture in Figure 10 is different than Figure 9, where the stable upslope ascent precipitation features (1) lost intensity and moved northward, the small-scale features (2) started to emerge (around day 18) and the features due to baroclinic waves (3) started to appear periodically as the simulation went on. These three features are all different in their origin, thus present valuable insight in terms of their difference between each dynamical core as they point towards a different aspect of models. Coarser resolution models (CAM Eulerian Spectral T85 and CAM FV 1 degree) do not simulate the small-scale features, although some very low intensity precipitation can be observed for CAM FV 1 degree model on the mountain peak. The finer resolution models simulate these features, but with the difference of CAM Eulerian Spectral T170 simulating them with larger spatial extent and higher intensity when compared to that of CAM FV 0.5 degrees. This sensitivity to intensity is contrary to what is observed with the large-scale stable upslope ascent features. All models produced the features due to baroclinic waves (CAM FV 1 degree seem to have missed it in Figure 10; however it appears in other days due to periodic nature of this phenomenon).

To understand these differences, it is essential to understand the genesis and evolution of these features. Vertical pressure velocity (OMEGA), moisture flux convergence (MFC) and zonal winds were plotted for the lowest model level and are given in Figure 11.
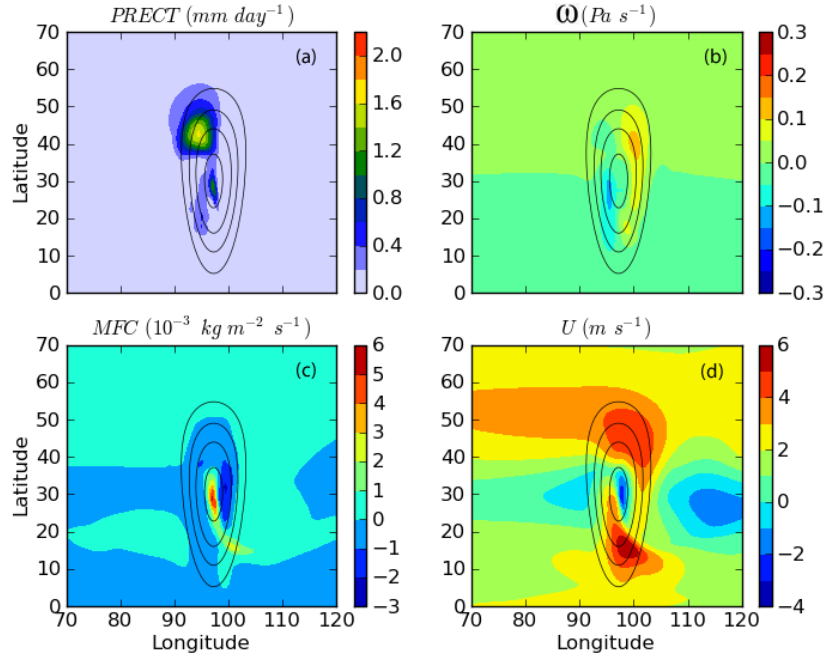
Figure 11: (a) Day 23 total precipitation rate, (b) vertical pressure velocity (ω), (c) moisture flux convergence (MFC), and (d) zonal velocity (U) overlaid by surface geopotential for case 1 simulated by CAM FV 0.5 degrees.

Diagnostics for CAM FV 0.5 degrees are chosen to explain the evolution of features as it has all the features simulated. There is negative pressure velocity, upward motion, (Figure 7b) on the windward side of the mountain where the large-scale precipitation feature is observed. This is consistent with the stable upslope ascent process and the subsequent condensation/precipitation explained in section 1.2 (Figure 3).

MFC is a prognostic quantity for forecasting convective initiation, with an emphasis on determining the favorable spatial location(s) for such development (Banacos and Schultz 2005). In our study we use this quantity as a diagnostic to understand the behavior of the small-scale features appearing on the peak of our mountains. MFC can be derived from the conservation equation for water vapor in pressure coordinates:

$$\frac{dq}{dt} = S \tag{14}$$

where q is the specific humidity and S represents the sources and sinks of water vapor. We calculated the surface MFC on the lowest hybrid model level. The material derivative for water vapor on hybrid vertical coordinate (Collins et al. 2006) can be written as:

$$\frac{dq}{dt} = \frac{\partial q}{\partial t} + \boldsymbol{V}_h \cdot (\boldsymbol{\nabla} q) + \dot{\eta}\frac{\partial q}{\partial \eta} \tag{15}$$

where η represents the model level, $\dot{\eta}$ is $d\eta/dt$, $\boldsymbol{V}_h$ is the horizontal velocity vector, and $\boldsymbol{\nabla}$ is the two-dimensional gradient on constant η surfaces. The continuity equation in the hybrid vertical coordinate:

$$\frac{\partial}{\partial t}\left(\frac{\partial p}{\partial \eta}\right) + \boldsymbol{\nabla} \cdot \left(\frac{\partial p}{\partial \eta}\boldsymbol{V}_h\right) + \frac{\partial}{\partial \eta}\left(\dot{\eta}\frac{\partial p}{\partial \eta}q\right) = 0 \tag{16}$$

where $\partial p / \partial \eta$ is the hybrid vertical coordinate pseudo density. Writing the flux form using these two equations and rearranging in spherical coordinates yields:

$$\frac{\partial}{\partial t}\left(q\frac{\partial p}{\partial \eta}\right) = -\frac{1}{a\cos\phi}\left[\frac{\partial}{\partial \lambda}\left(uq\frac{\partial p}{\partial \eta}\right) + \frac{\partial}{\partial \phi}\left(vq\frac{\partial p}{\partial \eta}\cos\phi\right)\right] - \frac{\partial}{\partial \eta}(q\frac{\partial p}{\partial \eta}\dot{\eta}) + (E-P)\frac{\partial p}{\partial \eta} \tag{17}$$

where E is evaporation and P is precipitation. This equation is an expression of the moisture budget of an air parcel. All terms in this equation are divided by g (gravitational acceleration) thus the MFC unit is kg m^{-2} s^{-1}. The first, bracketed term in the right hand side of the above equation is the MFC and is plotted in Figure 11c. The second term is the vertical MFC. MFC has traditionally been calculated as a vertically integrated quantity (Frankhauser 1965; Hudson 1970); however, Newman (1971) calculated the surface MFC to be able to make use of high-resolution temporal and spatial observations of the lower level atmosphere. The majority of the studies computed surface, not vertically integrated, MFC since then. Given the variable of interest being total precipitation on the surface in our study, we also calculated surface MFC to be able to have a sensible diagnosis.

The small-scale precipitation features (2) in Figure 10 have complex and multiple underlying causes. The location of peak convergence of moisture flux and in Figure 11c (on the mountain peak) is where the small-scale precipitation is observed. Previous studies also showed a strong relationship between surface MFC and the precipitation (Becker et al. 2011; Bhushan and Barros 2007; Holman and Vavrus 2012). This convergence can have multiple reasons such as moisture transport from the moist air impinging on the mountain and local evaporation over the mountain peak where precipitation is observed. These small-scale features, unlike the large-scale stable upslope ascent features, remain stationary after their inception. However, there is a convergence of zonal wind (Figure 11d) where the precipitation is observed. This convergence of the zonal winds transport moisture to this area representing another mechanism of orographic precipitation given in Figure 2d, i.e. lee-side convergence. Also, additional model runs were made with varying the SST of the aquaplanet setting, which showed increased intensity of these small-scale precipitation features with increasing SST, whereas decreased SST ultimately led to the disappearance of these features. This phenomenon is due to the increase in local evaporation triggered by the surface flux parameterization in the simple physics suite, with increased SST. Therefore these small-scale features are labeled as features due to local evaporation and lee-side convergence.

As summary for this initial case, we were able to observe and identify causes and evolution of orographic precipitation features observed in AMIP runs in Figure 6. The small-scale precipitation features (2) were lost via averaging in Figure 3, however the large-scale upslope features (1) were apparent. The features due to the baroclinic waves (3) were inherent to the setup we created, and do not have easy analogues in the AMIP runs we examined.

2.2.2. Case 2 "Double Mountain"

Figure 12 shows the surface geopotential and 30 day mean total precipitation (as in Figure 5) for case 2, two mountains of the same size.
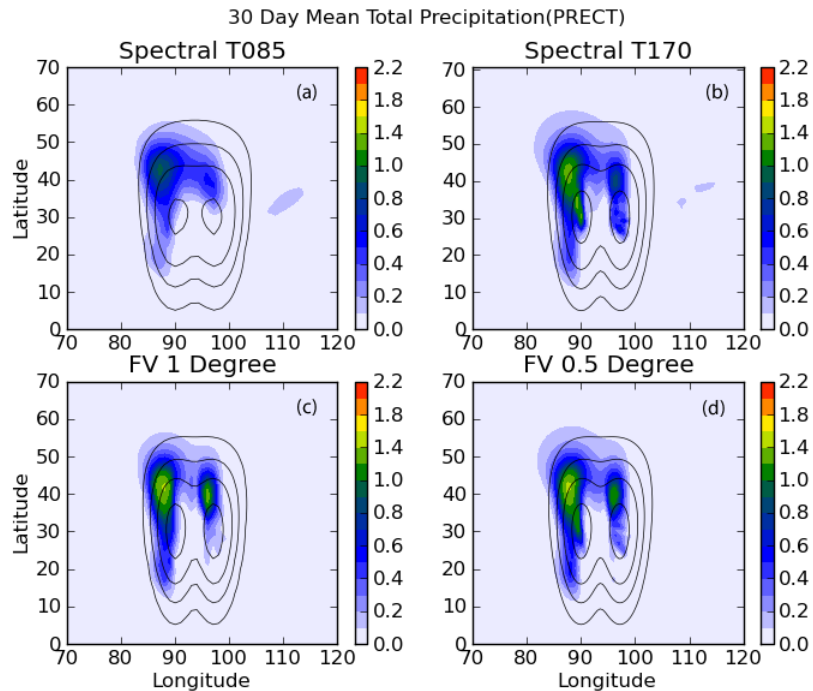
Figure 12: *30 day mean total precipitation rate (mm/day), surface geopotential for case 2 simulated by (a) CAM Eulerian Spectral T85, (b) CAM Eulerian Spectral T170, (c) CAM FV 1 degree, and (d) CAM FV 0.5 degrees.*

The large-scale stable upslope ascent precipitation features appear in this case as separate features in the windward side of each mountain. The features in front of the eastward, downstream peak are lower in intensity and smaller in extent as the moist air precipitates at the first peak. Daily precipitation plots (not shown) exhibit these features appearing in front of the peaks on day 1 with high intensity. They then move northward and lose intensity every day. The large-scale features simulated by CAM Eulerian Spectral T170 are similar to CAM FV, however there is a higher amount of merging

between the two features simulated by CAM Eulerian Spectral T170. There is almost a total merge in CAM Eulerian Spectral T85 with relatively low peak intensity (1 mm/day), whereas features of the other three simulations have peak intensities at around 1.7 mm/day.

The main reason for the difference at the spectral resolutions is the spectral filtering applied to the topography for the CAM Eulerian Spectral model. To understand the effect of topographic filtering, additional model runs were made with CAM Eulerian Spectral T85 and T170 without the topographic filtering (Figure 13).

Figure 13: *30 day mean total precipitation rate (mm/day), surface geopotential for case 2 simulated by (a) CAM Eulerian Spectral T85, (b) CAM Eulerian Spectral T170 without the spectral filtering applied to topography.*

The filtering reduces the peak height of CAM Eulerian Spectral T85 by 243 meters, which is 16% of the total height of the mountain (The reduction is 42 meters for CAM Eulerian Spectral T170). The effect of removing the spectral filtering is especially apparent in the CAM Eulerian Spectral T85 precipitation plot (Figure 13a, compare with 12a) where the mountains are more structured and the two large-scale features in front of each mountain are more distinct in the case of unfiltered topography. However these features still have relatively low intensity when compared to the other three simulations. The peak precipitation rates of the two large-scale features for CAM Eulerian Spectral

T170 (Figure 8b) increased with the steeper topography. The change in the topography of CAM Eulerian Spectral T85 as a result of filtering can also be observed via the surface geopotential plot (Figure 14).
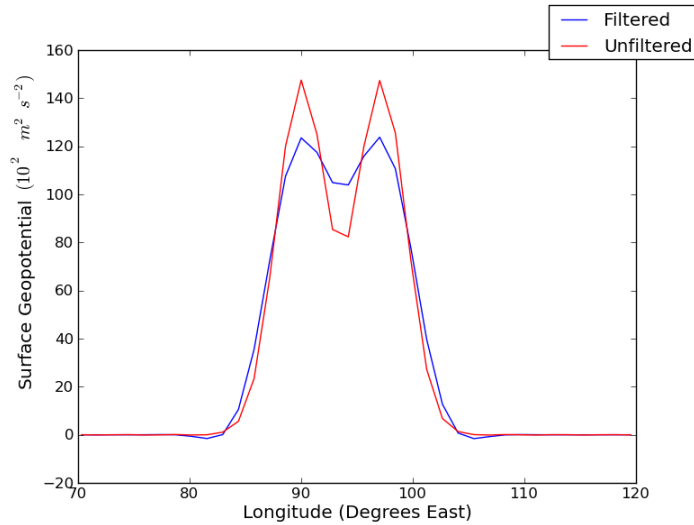
Figure 14: *The surface geopotential vs. longitude plot of CAM Eulerian Spectral T85 for filtered (blue) and unfiltered (red) topography. The latitude is 30° N, where the mountains have peak height.*

The orographic precipitation simulated by CAM Eulerian Spectral T170 strongly resembles CAM FV models due to the setup of case 2, which is not observed in the AMIP runs given in Figure 3. The mountains in case 2 are large and the related precipitation due to impinging airflow is easily resolvable for the fine resolution CAM Eulerian Spectral model. The separation distance between the two mountains is another parameter affecting the distribution of precipitation. The first mountain is located at 90° East and the second is located at 97° East, which allows 10 grid increments between them for CAM Eulerian Spectral 170 and 5 grid increments for CAM Eulerian Spectral T85. 10 grid points were enough for CAM Eulerian Spectral T170 to resolve the dynamics and precipitation behavior between the mountains so it was able to simulate the dryer region.

As the simulation proceeds, smaller precipitation features start to form after day 10 for all models except CAM Eulerian Spectral T85 (they are not as apparent for CAM FV 1 degree due to their relatively lower values thus being lost in the 30 day mean plots).

These features start to form at the peak points of the mountains as apparent in Figure 12b and Figure 12d. The second mountain leads to small-scale dynamics especially in between the two mountains (Figure 15d).
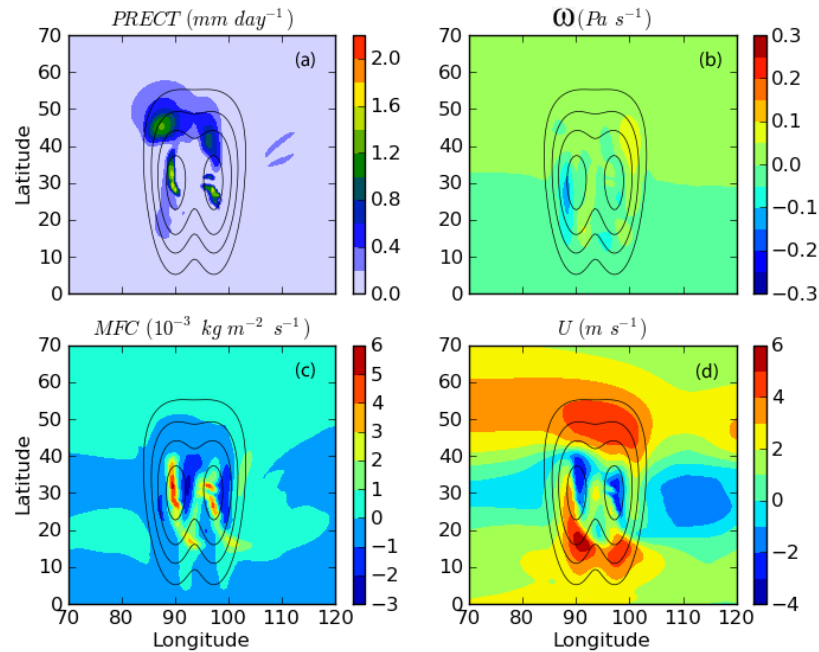
Figure 15: (a) Day 23 total precipitation rate, (b) vertical pressure velocity (ω), (c) moisture flux convergence (MFC), and (d) zonal velocity (U) overlaid by surface geopotential for case 2 simulated by CAM FV 0.5 degrees.

Figure 15 shows diagnostic measures as in Figure 11. The more structured manifestation of smaller scale features compared to case 1 (Figure 10), over both mountain peaks is apparent in Figure 15a. A similar manifestation can also be observed in MFC in Figure 15c, due to the smaller scale local dynamics. In addition to the surface flux parameterization of the simple physics suite feeding moisture back to the atmosphere, turbulence can also play a role in making the smaller scale features more structured. Houze and Medina (2005) showed that even if a stable flow impinges on the mountains, it can organize itself to produce a layer of smaller scale cellular overturning due to either shear-induced turbulence or buoyancy oscillations in the shear layer that are forced by the lower terrain.

Case 2 revealed that the size and the grid spacing between the two mountains significantly affect the simulation of orographic precipitation as well as the treatment of topography (i.e., the spectral filtering). We have yet to see the merging of the large features due to stable upslope ascent in front of each mountain peak for CAM Eulerian Spectral T170. However, as we move towards less resolvable scales (case 3) that are more resembling of Coast Ranges and the Sierra Nevada region, the differences between CAM FV and CAM Eulerian Spectral models become more apparent.
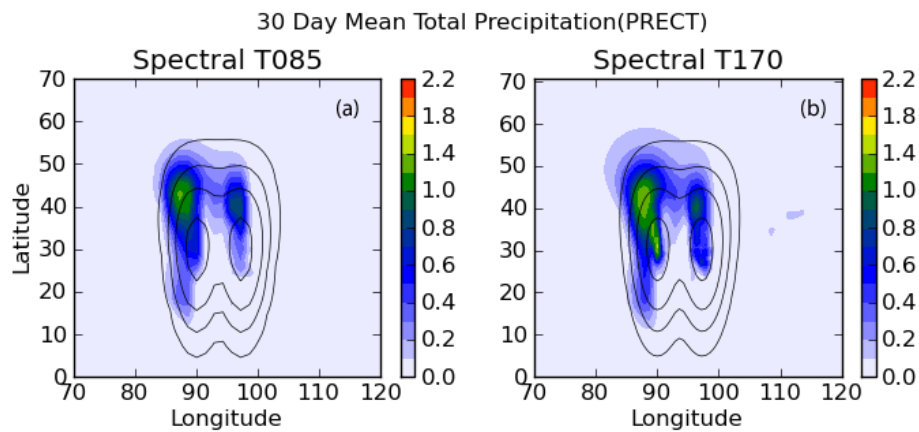
2.2.3. Case 3 "Realistic"
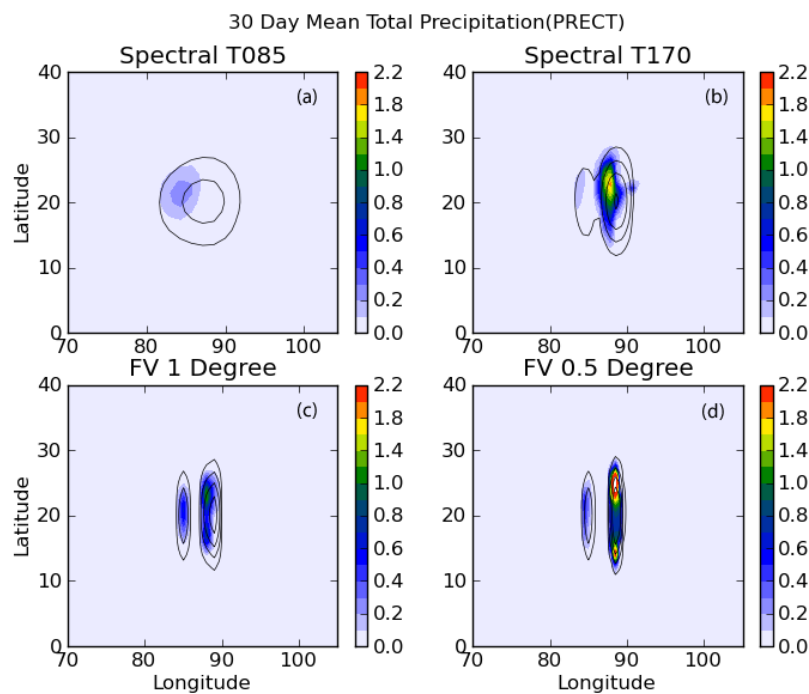
Figure 16: 30 day mean total precipitation rate (mm/day) and surface geopotential for case 3 simulated by (a) CAM Eulerian Spectral T85, (b) CAM Eulerian Spectral T170, (c) CAM FV 1 degree, and (d) CAM FV 0.5 degrees.

In this case the differences between CAM FV and CAM Eulerian Spectral models are much more apparent (Figure 16). Both CAM FV model resolutions were able to simulate

the dry region between the mountains whereas there is a merge between two precipitation features in the cases of CAM Eulerian Spectral T85 and T170. Both CAM FV models were able to create distinct mountains separated from each other. The CAM Eulerian Spectral T170 has connected the two mountains, leaving 5 grid points between peaks and CAM Eulerian Spectral T85 merged the mountains into one (Figures 16a and 16b). This shows that, as the topography gets smaller and structured, the ability of all models to simulate orographic precipitation is reduced. The CAM FV dynamical core represents the spatial structure and relationship with underlying topography more realistically than the CAM Eulerian Spectral dynamical core (Figure 6).

In case 2 there was the suggestion that topographical filtering adversely affects the simulation of orographic precipitation. In case 3 the CAM Eulerian Spectral core run without the filter, introduced significant amounts of noise due to Gibbs oscillations thus producing smaller scale precipitation features that dominate the entire field in a short period of simulation time. Therefore, without the topography filter the simulation is not realistic.

In case 3 there are significant differences between two resolutions of CAM FV model. In both CAM FV simulations, a precipitation feature occurs at the peak of the first, westward, mountain, which is lower than the second mountain. On the second mountain, two separate precipitation features are observed over both the north and south ends of the Gaussian-bell shape. The features simulated by CAM FV 1 degree are significantly lower in intensity when compared to CAM FV 0.5 degrees. This separation of large-scale stable upslope ascent features into two is not observed in either CAM Eulerian Spectral simulation; there is one big feature related to each mountain peak as in the previous cases. These big features are connected to the ones simulated over the first mountain peaks, creating a wet region between the mountains as opposed to the dry region in CAM FV models. To understand these differences, total precipitation, vertical

velocity and MFC are plotted for both CAM FV 0.5 degrees and CAM Eulerian Spectral T170, for day 3.
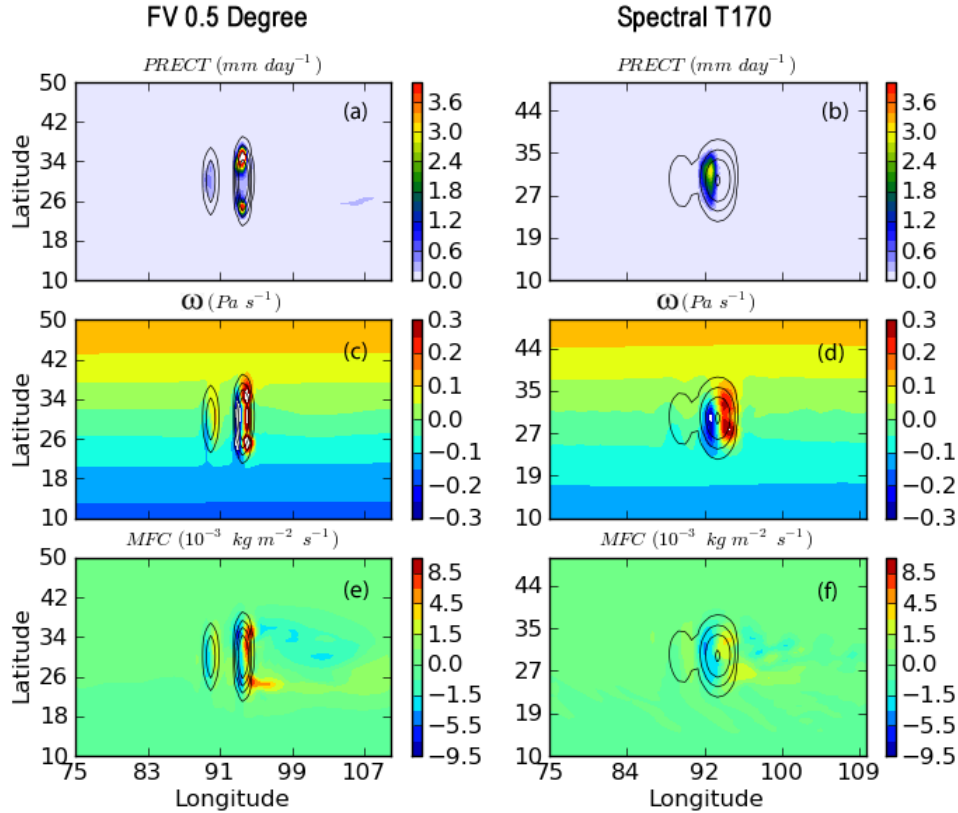
Figure 17: *Day 3 total precipitation rate, vertical pressure velocity (ω), moisture flux convergence (MFC) overlaid by surface geopotential, for case 3 simulated by (a,c,e) CAM FV 0.5 degrees, and (b,d,f) CAM Eulerian Spectral T170.*

The negative vertical pressure velocity (upward motion) at the windward side of the first mountain of CAM FV 0.5 degrees simulation leads to the large-scale stable upslope ascent precipitation (Figure 17c). This is not the case for CAM Eulerian Spectral T170 (Figure 17d), thus no precipitation over the first mountain, however it is apparent over the second mountain creating the single large precipitation peak observed in Figure 17b. The reason we don't observe such single precipitation feature for CAM FV simulation (Figure 17a) is the structured manifestation of both vertical velocity and the MFC (Figure 17e) over the second mountain. Both stable upslope ascent and surface fluxes contribute to the

organization of the precipitation for the CAM FV model, and both convergence/divergence boundaries and the negative vertical velocities occur at both tails of the second mountain, producing precipitation features over that area.

2.3. Summary of the Idealized Test Case Results

We were able to reproduce the precipitation features inherent to an orographic disturbance perceived in observations and simulated in AMIP runs (Figure 6). We were able to identify the origins of these features via orographic precipitation theory and diagnostic measures and classify them as (1) large-scale features due to stable upslope ascent, (2) smaller scale features due to local surface fluxes, (3) leeward side features due to baroclinic waves.

Examination of the differences in simulation of these features by CAM FV and CAM Eulerian Spectral dynamical cores with varying resolutions led to deeper understanding about the sources of biases related to GCM structure, and how the biases evolve with varying resolution. CAM FV model simulations resembled observations, producing precipitation consistent with underlying topography as well as the dry regions. The fine resolution CAM Eulerian Spectral model exhibited similar behavior, when the mountains were well separated and the same height (cases 1 and 2). The CAM Eulerian Spectral simulation developed biases similar to the AMIP simulations when the mountains were of different height and closer together (case 3). It was also noted that the effect of resolution is much more pronounced for CAM Eulerian Spectral models compared to CAM FV models, as the improvement of results from T85 to T170 was significant while CAM FV 1 degree and 0.5 degrees consistently produced similar results.

The merger of two large-scale stable upslope ascent features observed in AMIP runs for CAM Eulerian Spectral T170, were not observed in case 2 where mountains were

well separated. Furthermore in case 2, the removal of the spectral filtering applied to topography improved the results (especially for CAM Eulerian Spectral T85). However, the merger was apparent in the realistic case 3 and the removal of spectral filtering gave unacceptable results for both CAM Eulerian Spectral T170 and T85. We conclude that the performance of CAM Eulerian Spectral dynamical core and the improvement capability of spectral filtering depend on both the scales of the topography and the scales of the features to be simulated. These scales are in a dynamic relationship with each other, thus it is challenging to produce a specific solution of when and/or how to apply any limitation (e.g. filtering) to spectral models.

The characterization of features observed in AMIP runs and our test cases is a crucial step towards application of our object-based bias, as identification and isolation of these features will depend on the underlying conditions that create them as well as their size, shape, and location etc.

CHAPTER 3: QUANTITATIVE ANALYSIS PART I: Monthly Mean Analysis with Clustering and Geostatistics.

The quantitative analysis involves the identification and the evaluation of the orographic precipitation features (3rd step of the object-based approach) simulated by the idealized test cases. After analyzing the simulated features and identifying the underlying causes of their manifestation (previous section), the features are isolated from the whole precipitation field and matched by their analogues across all simulations (i.e., CAM Eulerian Spectral T85 and T170, CAM FV 1 and 0.5 degrees resolution). This chapter focuses on monthly mean results for all simulations. The small-scale features due to local evaporation and lee-side convergence do not explicitly show up on monthly mean results due to averaging. Therefore, the focus of this chapter is on the large-scale features using k-means clustering and geostatistics (variography) for their identification and evaluation. The time dimension is added to the analysis in chapter 4 by analyzing the daily results using classification trees for the identification of the features (which also involves small-scale features) and simple statistical measures (e.g., mean and variance) for their comparison.

An object-based method involves the classification of the field of interest into parts to be treated and evaluated as objects. This is a crucial step since the accuracy in defining and isolating the objects determines the overall reliability of the final results of the method. To decide which class of object the grid point belongs to, object classification is traditionally done by setting a threshold for a variable and evaluating the grids in the field relative to that threshold (i.e., is the grid value above or below the threshold?) (Davis et al. 2006; Ebert and McBride 2000; Micheas et al. 2007; Wernli et al. 2008). This has been a limiting step in object-based methods since user defined threshold values can be insufficient in treating different types of objects that can be manifested in different times

of simulations (e.g., a big threshold might lead to missing the small features). This problem was addressed by (Skok et al. 2013) where they employed more than one value as a threshold to increase the capability of the method. We adopt an approach to increase the flexibility of the object identification by making dynamic threshold decisions according to the characteristics of the field of interest. In this study, we used k-means clustering (Everitt et al. 2011) for the purpose of object identification, which eliminates the user defined threshold by setting a pre-specified number of object classes. We also investigate the applicability of variography (Isaaks and Srivastava 1989) for comparison and verification of isolated objects. The next section gives information about both k-means cluster analysis and variography. Both methods have been used for evaluation of weather prediction and climate models (Alhamed et al. 2002; Johnson et al. 2011; Liu and George 2005; Marzban and Sandgathe 2006, 2009). They are applied to the idealized test case results with an object-based point of view. Initially, variography is applied to synthetic data that resemble orographic precipitation features to observe how variography quantifies important characteristics of objects (e.g., magnitude, location, size). Results of this analysis are also given in the next section. Application of these methods to the idealized test cases and the discussion of the results are given in sections 3.2 and 3.3, and the summary of the results are given in section 3.4.

3.1. Methods

3.1.1. K-means Cluster Analysis

Cluster analysis is a technique that uses a measure of similarity (or dissimilarity) to classify data into groups called clusters. Each cluster is formed in a way that its members have higher similarity to each other than to members of other clusters. Clustering has been extensively used in meteorology and climatology (Huth et al. 1993; Littmann 2000; Liu and George 2005). It has also been applied for object-based purposes including storm

54

and cloud identification (Lakshmanan et al. 2003; Peak and Tag 1994), verification of precipitation fields produced by weather prediction models (Marzban and Sandgathe 2006), and classification of multi-model ensemble data (Alhamed et al. 2002). These studies employed hierarchical cluster analysis methods. Hierarchical clustering makes a series of partitions, which may run from a single cluster containing all individuals, to *n* clusters each containing a single individual. In this study we use k-means clustering, which does not form hierarchical classifications but partitions the data into a pre-specified number of groups. The partitioning algorithm involves calculating the centroid of each cluster via a measure of distance, where each centroid is the mean value of the points in that cluster. We use the squared Euclidian distance as the measure of distance. It should be noted that this distance is not the spatial distance between the grid points, but rather it is the difference between the grid point values. In general, given an n x p matrix **X** where n is the number of observations and p is the number of variables, the squared Euclidian distance (d) is defined as:

$$d_{ij} = \left[\sum_{k=1}^{p} \left(x_{ik} - x_{jk} \right)^2 \right]^{1/2} \tag{18}$$

The Euclidian distance (d) can be defined as the distance between two p-dimensional points $x_i = (x_{i1}, \ldots, x_{ip})$ and $x_j = (x_{j1}, \ldots, x_{jp})$ in Euclidian space. In our analysis we reduce a latitude-longitude grid matrix of a given precipitation field into a single one-dimensional vector (n x 1, where n = latitude x longitude) to apply the k-means algorithm. In this case the Euclidian distance (d) reduces to:

$$d_{ij} = \left| x_i - x_j \right| \tag{19}$$

The sum of distances, over all clusters, from each point to its cluster centroid is then minimized iteratively. The points are moved between clusters until the sum cannot be decreased further, resulting in clusters as well-separated as possible. The mathematical details of this method can be found in Spath (1985) and Everitt et al. (2011).

Once the clusters are formed, the reduced vector is then expanded to the latitude-longitude grid to visualize the cluster boundaries. We used 2 (k=2) and 3 (k=3) clusters in our calculations. The k=2 clustering is assumed to classify the whole field into non-rain and rain parts whereas the k=3 clustering classifies for non-rain, light rain, and heavy rain parts. This analysis serves as the identification of the orographic precipitation features by determining the boundaries of the rain areas to be analyzed as objects. These rain areas are analogous to the ones defined in Davis et al. (2006), where they are determined by convolving the precipitation field with a given shape as a smoothing process. The smoothed field is then thresholded to get the object boundaries.

3.1.2. Variography

The objects determined by the spatial boundaries of the rain areas from cluster analysis are evaluated by applying variography. Variography is a geostatistical method, which is used to measure the spatial continuity of a variable Z. Marzban and Sandgathe (2009) applied variography as a verification method to numerical weather prediction models. In that study variography was used to compare two fields, however; in this study we apply the method to acquire information about isolated objects rather than the whole field.

The semivariogram (γ) (hereafter SV) is defined as the variance of the difference between two points separated by a distance h. Assuming stationarity, which states that all pairs of random variables separated by a particular distance h have the same joint

56

probability distribution regardless of their locations (Isaaks and Srivastava 1989), the SV can be defined as:

$$\gamma(h) = \frac{1}{2} Var[Z(s + h) - Z(s)] \tag{20}$$

where Var is the variance function, $Z(s)$ is the variable of interest (in our case precipitation), which is a function of location s (Matheron 1963). Assuming the spatial variable Z is free of systematic surface trends yields:

$$\gamma(h) = \frac{1}{2} E\{[Z(s + h) - Z(s)]^2\} \tag{21}$$

where E is the expected value (mean) function. The above equation computationally yields:

$$\gamma(h) = \frac{1}{2|N(h)|} \sum_{N(h)} [Z(s_i) - Z(s_j)]^2 \tag{22}$$

where $N(h)$ is the set containing all the neighboring pairs at distance h, i.e., $N(h) = \{i, j: s_i - s_j = h\}$, and $|N(h)|$ is the total number of pairs. The SV function is then plotted against varying h to observe the spatial continuity of the variable. The selection and the classification of data pairs are crucial in the SV computation. Pairs might not be separated exactly by the selected distance h, so distance classes are formed in order not to exclude them from the computation. The distance class L for two arbitrary points P_1 and P_2 is calculated as:

$$L(P_1P_2) = \lfloor |P_1P_2|/\Delta + 0.5 \rfloor \qquad\qquad\qquad (23)$$

where $|P_1P_2|$ is the distance between P_1 and P_2, $\lfloor x \rfloor$ denotes the largest integer $\leq x$ for any arbitrary x, and Δ is the user defined parameter determined depending on the case. If the points are paired in every possible direction (i.e. if a pair is determined only depending on the scalar separation distance but not a vector with an angle), the resulting SV is called an omni-directional SV. However points can be paired specifying an angle. If, say, we pair the points only in 90° direction, the resulting SV is called a 90° directional SV and gives information about the spatial continuity in that particular direction. As in the case of distance specification, an angle tolerance value is defined to have enough number of pairs in the calculation. So as an example, if we are looking at 90° direction and define an angle tolerance of 10°, we look for a pair of a point within a 90° ± 10° arc, rather than only looking at a line on 90° direction. The parameter Δ and the angle tolerance are taken as 300 km and 10° respectively for all SV calculations presented in section 3.1.2.

Prior to application of this method to the idealized test case results, we tested the utility of variography using synthetically created data. Two Gaussian-hill shaped objects were created to represent the mountain range precipitation features. The objects were trimmed in two sides to create an elongated feature similar to a precipitation feature aligned with a mountain range. Figures 18a and 18b show the 3D plots of these two objects, Figures 18c and 18d show their corresponding contour plots, and Figure 18e shows the omni-directional SV of the two objects.
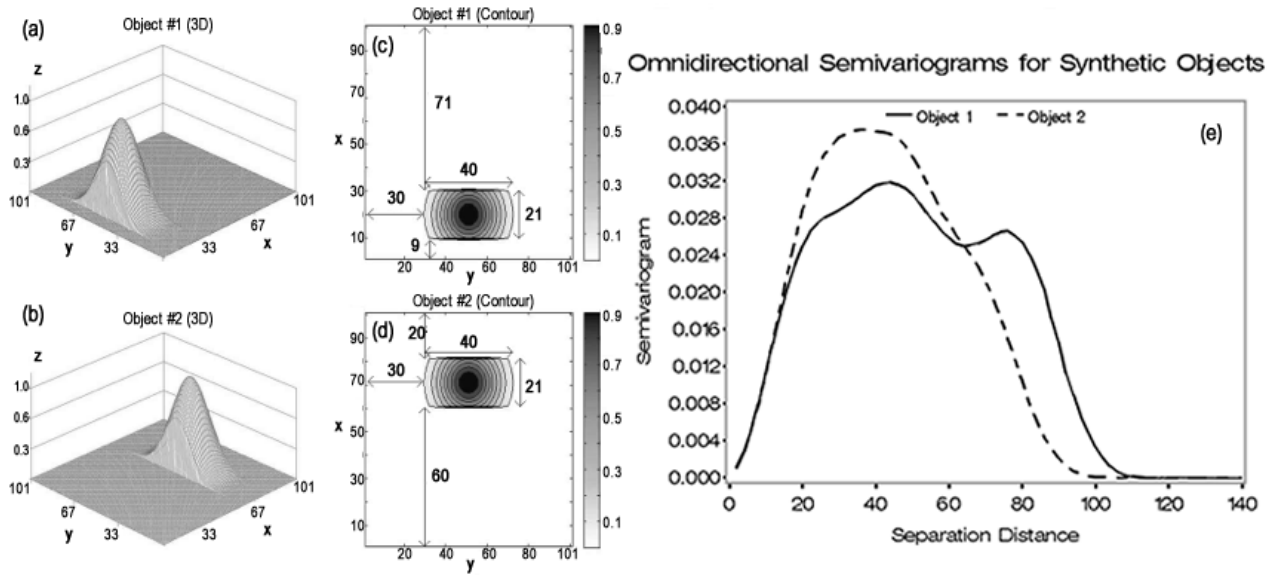
Figure 18: 3D plots of synthetic objects 1 (a) and 2 (b), their corresponding contour plots (c, d), and their SVs (e). The size, length and the magnitude of the objects as well as the SV values are in arbitrary units.

The x and y distances (the horizontal domain) that the objects are created on are both 101 arbitrary units respectively. Each object is 71 x 21 units in horizontal plane and they are created at the same orientation in y direction, i.e. 30 units away from both ends of y axis. However the objects do not have this symmetry in x direction. Object 1 starts 9 units away from the x-axis and object 2 ends 20 units away from the end of the x axis. The maximum value (magnitude) attained by both objects is 1.

There are striking differences between the two SVs due to the dissymmetry of two objects in x direction. When two objects are symmetric (e.g., the same unit distances from the center of the object and the end of the domain in x direction), the resulting SVs would be identical due to the stationarity assumption. Advantageous from an object-based point of view, SVs carry information about the location of objects; however, one should be careful interpreting the results due to the sensitivity of SVs to shifts in location. The solid line SV in Figure 18e exhibits characteristics of object 1 in a way that is quite similar to the synthetic data analysis done by Marzban and Sandgathe (2009). The SV has

a bend at separation distance 22, which is about the size (length) of the object in x direction. After that point the SV steadily increases to the peak point at separation distance 42. This peak is related to the distance of the center of the object from the origin in Marzban and Sandgathe (2009), which in our case is around 53. This difference between the two synthetic data analyses is due to the difference in shapes of the objects. In our case we have a Gaussian-hill with trimmed tails in the x direction, however Marzban and Sandgathe (2009) had a bivariate Gaussian with same mean (30) and standard deviation (7.5) in both x and y. As equation 5 implies, the SV value for a particular separation distance is calculated by adding the squared difference of the pairs divided by the total number of pairs separated by that distance. If we pick a separation distance longer than the size of the object on the direction parallel to the y axis (i.e. 0 degrees) for object 1, we can pair points on the same direction both of which will remain outside the object. This means subtracting zero from zero, which doesn't add to the cumulative SV value. However if we focus on separation distance approximately 42 (which is the distance where we observe our maximum SV peak in Figure 18e) on the same direction; it can be seen that we always pair one point inside the object and one point outside thus the squared difference always gives a positive value. This leads to the maximum valued peak in the SV in Figure 18e. The next peak in the SV is at separation distance 77, which is about the distance from the center of the object to the end of the domain in x-axis, and this agrees with the discussion in Marzban and Sandgathe (2009) about their analogous peak.

Object 2 is in the same location as object 1 in y direction, but is pushed to the other end of the domain in x direction. The corresponding SV exhibits one single peak at separation distance 38 and a slight bend in separation distance at around 70. The change in location of the object changed the behavior of the corresponding SV; however we cannot observe signatures of that particular location except the distance 70 which is the distance of the center of the object to the beginning of the domain in x direction.
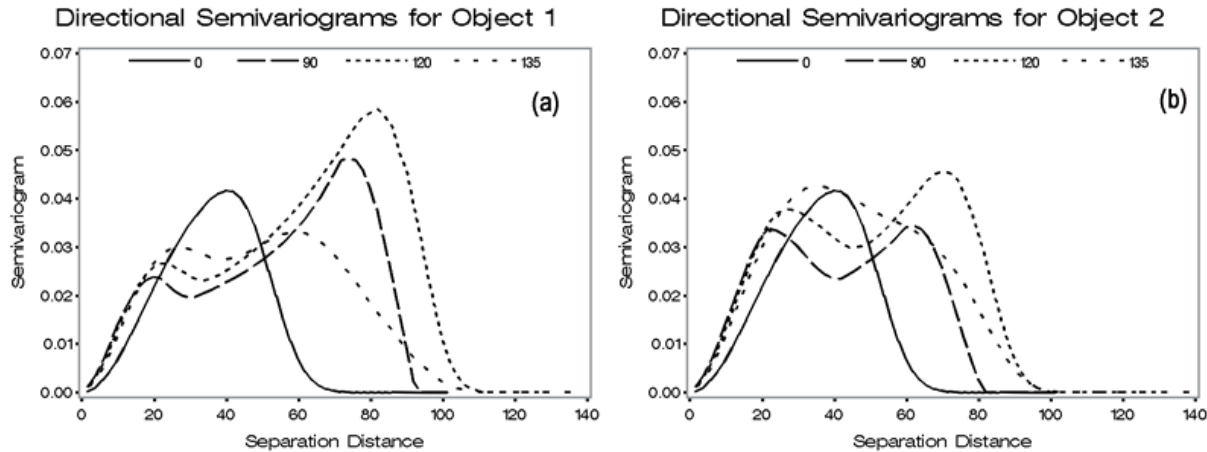
Figure 19: *Directional SVs of object 1 (a), and object 2 (b) for four different directions.*

To extract detailed information about objects, SVs of particular directions should be employed. Figure 19 shows SVs of the two objects in 4 directions: 0°, 90°, 120° and 135°. 0° direction is the direction along the y-axis, 90° direction is the direction along the x axis. The angle tolerance is 10°. In the directional SVs, we observe signatures of size and location of the objects as peaks at particular separation distances in Figure 19. For the 90° SV two peaks are observed for both objects, the initial peak being at separation distance 20 and 22, the latter peak being at separation distance 74 and 62 for objects 1 and 2 respectively. The first peak in both SVs is related to the size of the objects in x direction and second peak is related to the distance of the center of the object to the far end of the domain in x direction. So the 90° SV gives information about the attributes of both objects in x direction. The 120° SV gives similar results, but there is a shift in peaks to longer separation distances. On the other hand the 0° SV for both objects give information about the attributes in y direction. As can be seen on both red curves, there is a single peak at separation distance 40 which is both the size of the object in y direction and the distance of the center of the object from both sides of x axis.

The synthetic data analysis proves the capability of SVs on exhibiting information about characteristics of an object on a single curve. However, the ambiguity of SVs is

also apparent in the case of overlapping distances, e.g. if an objects size is similar to its distance from a particular end of the domain, both will be represented by the same peak or bend on an SV. To overcome this issue, directional SVs will be employed to identify the significance of each peak or bend on an omni-directional SV. The directional SVs will not be presented in the discussion of results of idealized test cases, however the information obtained from them will be indicated when necessary.

3.2. Identification of Objects by K-means Clustering

K-means clustering was applied to monthly mean simulations of single mountain, double mountain, and realistic setups of idealized test cases. The object classification results for the double mountain setup (topographical setup #2) are presented in this section as a representation of the utility of clustering. The comparison and evaluation results for all three topographical setups (Table 1) will be presented in the next section. The object boundaries for k=2 and k=3 cluster analyses for simulations of the double mountain setup of two dynamical cores with two resolutions are given in Figure 20.
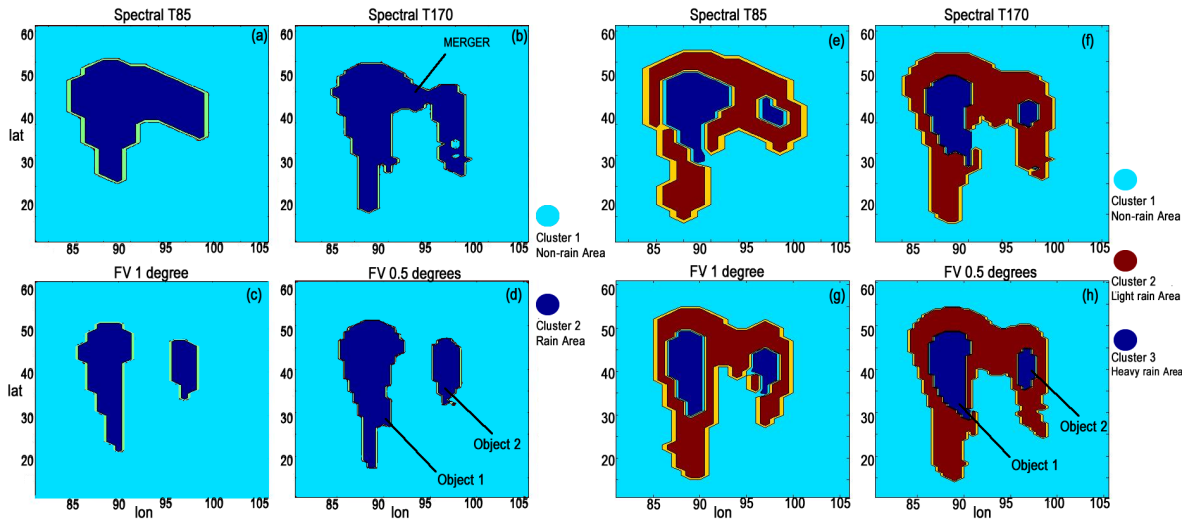
Figure 20: *K-means clustering results of the double mountain setup for k=2 and k=3 of (a,e) CAM Eulerian Spectral Transform T85, (b,f) CAM Eulerian Spectral Transform T170, (c,g) CAM FV 1 degree, and (d,h) CAM FV 0.5 degrees dynamical cores.*

The dark blue areas in Figure 20 indicate the boundaries of the objects to be isolated and evaluated by variography. These areas are predominantly stable upslope precipitation (Figure 12). For the k=2 clustering (Figures 20a-d) the clusters are labeled as rain areas (dark blue) and non-rain areas (light blue). The similarity of both large-scale upslope ascent features (labeled as objects 1 and 2 in Figure 20d) between CAM FV 0.5 degree and CAM Eulerian Spectral T170, which has been observed visually is apparent in Figure 20 in terms of their spatial boundaries. The clustering reveals the level of merger between the two features simulated by CAM Eulerian Spectral T170 (black arrow in Figure 20b). This merger was observed in the AMIP simulations of spectral T170, which motivated us to select these features as study features for further analysis. However, this merger was not visually apparent in the CAM Eulerian Spectral T170 simulation for the double mountain setup (Figure 12). Unlike T170, the merger was apparent for CAM Eulerian Spectral T85 and this is affirmed by cluster analysis, which produced a single rain area with an eastward extension (Figure 20a).

The large-scale stable upslope features for CAM FV 1 degree and 0.5 degrees show similarity in their spatial boundaries (Figures 20c and 20d). The dryer region between the two mountains for both CAM FV models is included in the non-rain area cluster as an indication of the separation of two features. The cluster analysis suggests a stronger wet-dry contrast in the CAM FV core than in the spectral core. There is a stronger sensitivity to resolution in the CAM Eulerian Spectral core, as well as a suggestion that at the higher resolution the two cores are more similar.

For the k=3 clustering (Figures 20e-h) the clusters are labeled as heavy rain areas (dark blue), light rain areas (red), and non-rain areas (light blue). With the inclusion of a light-rain category the spatial pattern of the precipitation fields are more similar. The contrast between the CAM Eulerian Spectral and CAM FV dynamical cores is less distinct with the k=3 clusters.

The results of k=3 clustering exhibits the flexible nature of cluster analysis on object boundary identification. The total area occupied by both heavy and light rain in k=3 clustering is bigger than the area occupied by the rain areas in k=2 clustering. As the number of clusters change, the proximity of points between the clusters change. As the number of pre-defined clusters increase the total area of rain represented by clusters increase. This characteristic of the method is beneficial in terms of an object-based point of view, not only because it defines objects relative to values of the field of interest, but also because it can divide an object into sub-parts, the analysis of which can give valuable information.

Returning to the meteorological description of the rain in Figure 12, the additional light-rain category allows more distinct identification of the stable up-slope precipitation with the dark blue clusters of Figure 20e-h. Our analysis proceeds by using the object boundaries in Figure 20 along with the precipitation values over the defined object areas.

The points outside the object boundaries were assigned the value 0 and the original sizes of the field were kept the same, since SVs are sensitive to location. Then, variography is used for all simulations for comparison and evaluation. The comparison of objects with variography is given in the next section.

3.3. Comparison of Objects with Semivariograms

In this section the objects are extracted from the three idealized topographies described in Table 1. For the double mountain case, the stable upslope precipitation features are labeled as objects 1 and 2 (Figure 20d). In the single mountain case, not shown, there is only one stable upslope feature, and it is labeled as object 1. Object 1 in both the single and double mountain cases are characterized by being on the windward, westward side of the domain. They are the features simulated where the moist air first impinges on a mountain slope.

The omni-directional SVs of object 1 for the single mountain and double mountain cases are given in Figure 21. These are for k=2 clustering given in Figures 20a-d. The merger for the spectral model simulations in k=2 clustering (Figures 20a and 20b) means, formally, that 2 objects are not identified for the spectral model simulations. To allow comparison of the precipitation on the westward peak, a line is drawn between two mountains at 93° W, and the westward part of the divided rain area is included in the SV calculation as object 1.
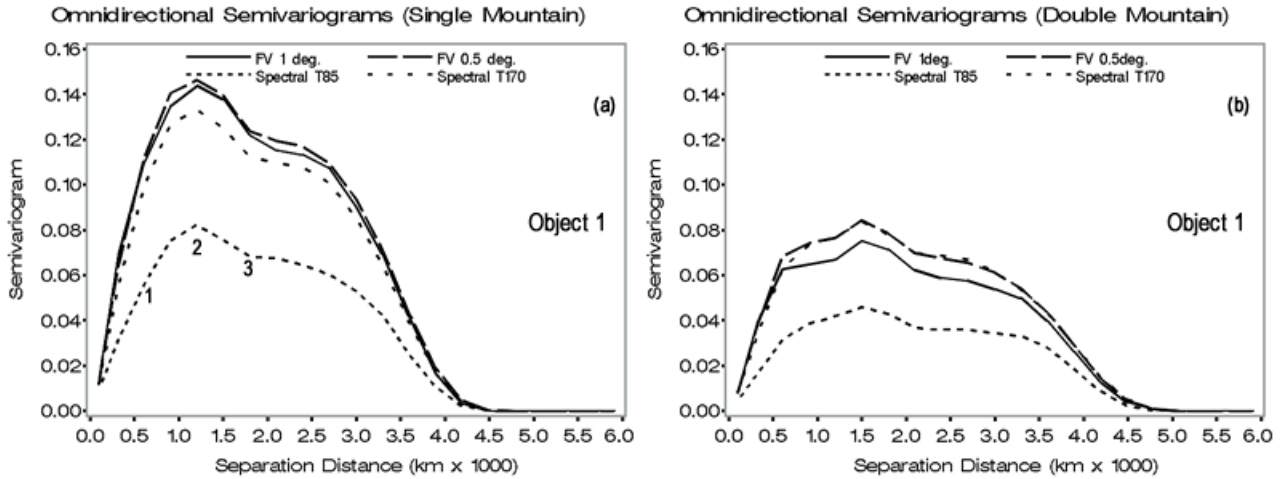
Figure 21: *Omni-directional SVs (mm/day)^2 of the large scale upslope ascent features (object 1) for (a) single mountain, and (b) double mountain setups simulated by CAM Eulerian Spectral T85 and T170, CAM FV 1 degree and 0.5 degrees dynamical cores. The object boundaries were determined by k-means clustering where k=2.*

In Figure 21, the magnitude difference of CAM Eulerian Spectral T85 from other simulations is apparent in the SVs of both single and double mountain cases. This shows a quantitative measure of how CAM Eulerian Spectral T85 simulates the large-scale upslope ascent feature in relatively lower intensity. There is close agreement in CAM FV 1 degree and 0.5 degrees SVs for the single mountain setup; however, they depart in the double mountain setup. The SVs of CAM FV 0.5 degrees and CAM Eulerian Spectral T170 shows close agreement for the double mountain setup. Figure 21 shows that the effect of resolution is much more pronounced in the case of the CAM Eulerian Spectral dynamical core. In the simpler setup (single mountain), the CAM FV dynamical core does not seem to have been affected by resolution as the SVs of both CAM FV resolutions are in agreement. In the more complex setup (double mountain) the agreement is between the higher resolution simulations of both dynamical cores suggesting the advantage of higher resolution over the more complex terrain.

The shapes of the SVs of all simulations for single and double mountain setups are similar. As indicated in the discussion of the synthetic data analysis, directional SVs are

important to interpret the peaks and bends of the omni-directional SVs in Figure 21 (which are numbered on the SV of CAM Eulerian Spectral T85 in Figure 5a). The initial bend at separation distance around 600 km (#1, Figure 21a) observed in all four simulations of both cases is related to the width of the objects in the zonal direction, therefore it shows up as a separate peak in the 90° directional SVs (not shown). The difference between the single and double mountain setups in Figure 21 is where the peak SVs occur (#2, Figure 21a). It is at around 1200 km for the single mountain, and 1500 km for the double mountain setups for all simulations. This shift is due to the change in the location of the object. After the peak SV there is another distinct bend in all four simulations at around 1700 km for single mountain, and 2000 km for double mountain setups (#3, Figure 21a). The 0° directional SVs show peaks at these distances for their corresponding setups, therefore this bend is indicative of the size of object 1 in the meridional direction. The large-scale stable upslope precipitation object extends to a longer distance in the case of double mountain setup, which shows that the circulation in the leeward side (due to the second peak and in between) affects the precipitation in the windward side. Another effect of addition of the second peak is the reduced rain amount of the windward (westward) large-scale stable upslope feature in the double mountain case. This is shown in Figure 21 as the reduced SV values of the double mountain setup, where the total amount of precipitation is distributed to both mountains. A simple calculation of the total amount of rain shows that there is an increase in precipitation for all simulations in double mountain setup compared to the single mountain setup. This increase is 15% for CAM Eulerian Spectral T85, 20% for CAM Eulerian Spectral T170, 15% for CAM FV 1 degree and 18% for CAM FV 0.5 degrees. An analysis of the total amount of precipitation in double mountain setup shows that 30% of the rain is simulated over the leeward mountain for CAM Eulerian Spectral T170, FV 1 and 0.5 degrees, whereas this percentage is 22% for CAM Eulerian Spectral T85.
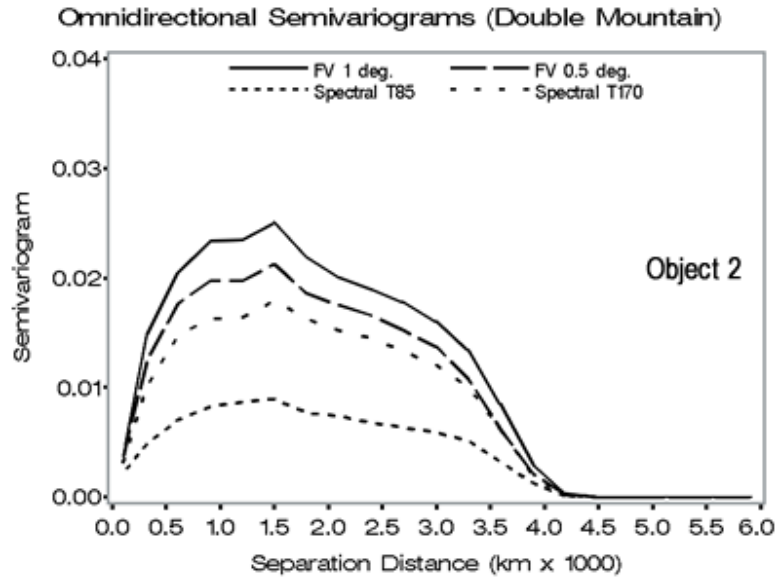
Figure 22: *Omni-directional SVs (mm/day)^2 of the large scale upslope ascent features, eastward mountain (object 2) for double mountain setup simulated by CAM Eulerian Spectral T85 and T170, CAM FV 1 degree 0.5 degrees dynamical cores. The object boundaries were determined by k-means clustering where k=2.*

In the double mountain case, object 2 is associated with the eastward mountain. The SVs of object 2 defined by k=2 clustering for all simulations is given in Figure 22. The close agreement between CAM FV 1 and 0.5 degrees and CAM Eulerian Spectral T170 for object 1 is not observed in the SVs for object 2 of the double mountain setup. FV 1 degree simulates the highest amount of rain in this object followed by FV 0.5 degrees and spectral T170. Although object 2 is the manifestation of the same phenomenon as object 1 (stable upslope ascent), it is smaller in size and affected by the small-scale circulation in between the two mountain peaks. Therefore this feature has more complex internal (unforced) dynamics and the reduction in spatial scales. The disagreement between simulations increases as the resolvable scales get smaller.
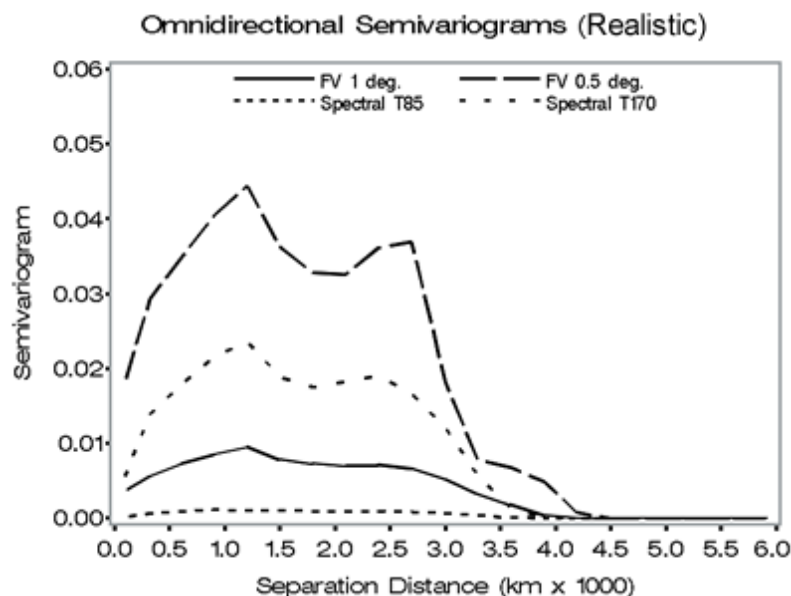
Figure 23: *Omni-directional SVs (mm/day)^2 of the precipitation features for the realistic setup simulated by CAM Eulerian Spectral T85 and T170, CAM FV 1 degree and 0.5 degrees dynamical cores. The object boundaries were determined by k-means clustering where k=2.*

For the more realistic setup that resembles the Coast Range and the Sierra-Nevada (Table 1) it is not possible to define obvious similar objects across all of the simulations, therefore the isolated objects are not labeled. Figure 23 shows the SVs of the objects defined by k=2 clustering, simulated by CAM FV 1 and 0.5 degrees, CAM Eulerian Spectral T85 and T170 for the realistic setup. This is simple separation into rain and non-rain. In this case the sensitivity to resolution is apparent, with CAM FV 0.5 degrees simulating higher amounts of rain followed by CAM Eulerian Spectral T170 and CAM FV 1 degree. The difference between each simulation is much more pronounced compared to the previous cases where the scales of the features were bigger. CAM Eulerian Spectral T85 produced very light rain and spectral model with both T85 and T170 resolutions produced a single feature over the mountains, whereas CAM FV model with both 1 degree and 0.5 degrees resolutions were able to simulate the dry region between two peaks (which was observed in the AMIP simulations discussed in Figure 6). This qualitative difference between the simulations, the merging of the precipitation

associated with the two mountains, is not obvious in the SVs in Figure 23, as the shapes of the SVs are again similar for all simulations. That is because the area between the two mountains is small in scale and in this case SV favors longer distances such as the distance of objects from the sides of the domain (The first peak in Figure 23 at around 1300 km is the distance of the objects to the westward end of the domain).

As noted in Figures 20e-h, the additional light-rain category for the k=3 cluster analysis allows more distinct identification of the stable up-slope precipitation. This supports more investigation of the sensitivity to resolvable scales. The top four frames of Figure 24 show object 2, for the eastward, down wind peak of the double mountain case. The objects are for both k=2 and k=3 cluster analysis results. These objects are isolated with the precipitation outside of the objects set equal to zero.
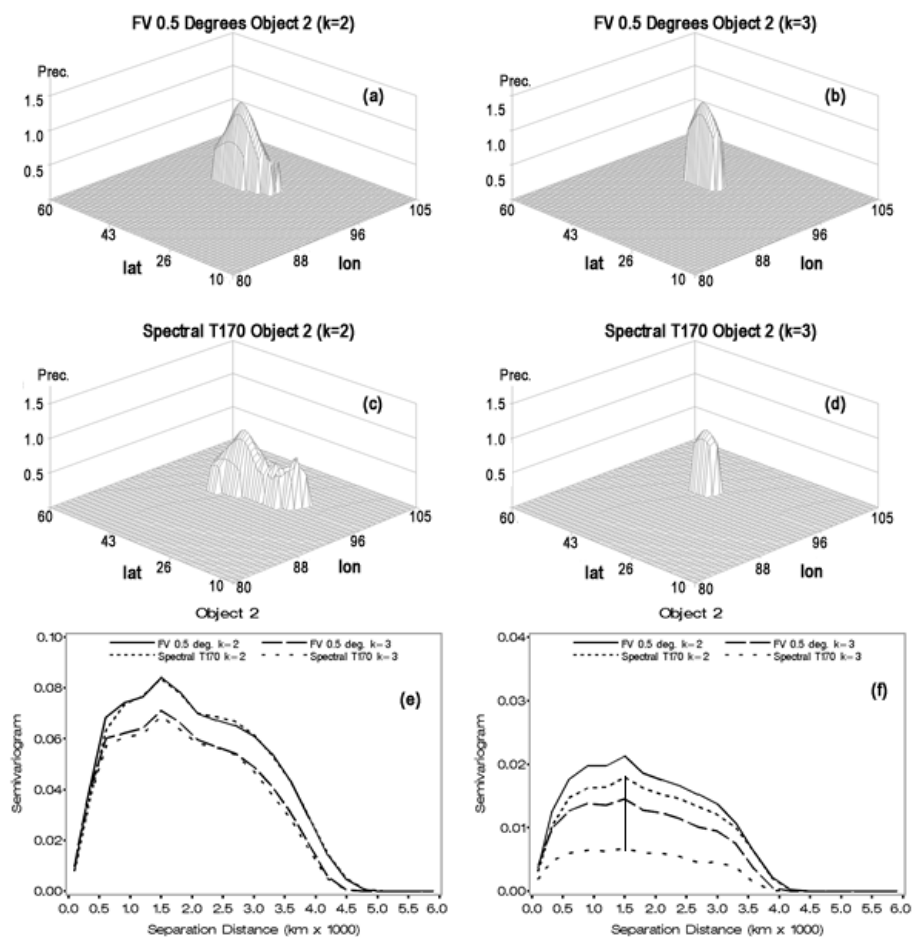
Figure 24: *3D plot of object 2 of the double mountain setup simulated by CAM FV 0.5 degrees with (a, b) k=2 and k=3 cluster analyses, CAM Eulerian Spectral T170 with (c,d) k=2 and k=3 cluster analyses. The omni-directional SVs (mm/day)^2 of CAM FV 0.5 degrees and CAM Eulerian Spectral T170 with k=2 and k=3 for object 1 (e, westward peak), and object 2 (f, eastward peak).*

The two frames on the top left (Figures 24a and 24c) are for the k=2 cluster analysis. The change of the boundary from k=2 to k=3 clustering (Figure 24b and 24d) can be viewed as how the "light rain" decided objectively by the cluster analysis is removed from the object. The remaining precipitation is the "heavy rain" as labeled in the selection process of the number of clusters (Figure 20). As can be seen in Figure 24a, CAM FV 0.5 degrees simulates object 2 with peak intensity without much spread, which is not the case for CAM Eulerian Spectral T170 (Figure 24c). CAM Eulerian Spectral T170 simulates the same object with lower intensity but higher spread. Referring back to

71

our definitions of the different types of observed features, this light rain category is primarily the rain associated with small-scale dynamics and local evaporation. This "spread out" effect of spectral dynamical core on precipitation was documented by Bala et al. (2008b).

    On the bottom right of Figure 24 are the SVs for object 2, the rain on the eastward peak. These are for the higher resolution simulations of the two dynamical cores for the k=2 and k=3 cluster analysis. By using k-means clustering together with variography, we are able to quantify how the distribution of rain in the heavy and light clusters differs in the two dynamical cores. As can be seen in Figure 24f, the difference between k=2 and k=3 clustering for object 2 is represented by the difference in SVs with a much higher difference in the case of CAM Eulerian Spectral T170 (indicated by a vertical line between the SV peaks of the spectral T170 k=2 and k=3). For comparison, we present the SVs for the precipitation on the westward, windward peak (Object 1, Figure 24e). For this object the SVs for CAM FV 0.5 degrees and CAM Eulerian Spectral T170 are similar for both k=2 and k=3 cluster analysis. We see that for the westward, windward peak (object 1) the precipitation from the two dynamical cores agree closely. The precipitation on the westward peak is largely defined by the design of the simulation experiment and is well resolved. The precipitation on the eastward, downwind peak is organized by dynamical features that develop after the interaction with the first peak. These dynamical features are of smaller scale than the flow that impinges on the westward peak. Though the dynamical characteristics of smaller scale features are similar in all simulations, the characteristics of the precipitation are qualitatively and quantitatively different.

3.4. Summary of the Monthly Mean Analysis

We applied k-means clustering to the idealized simulations for identification and isolation of orographic precipitation features as objects. Once the objects were defined, we applied variography to isolated objects and plotted their semivariograms (SVs) to compare and evaluate the features simulated by CAM FV and CAM Eulerian Spectral models in two resolutions to quantify their differences. Such quantitative analysis revealed the differences between CAM FV and CAM Eulerian Spectral dynamical cores better than a visual analysis. The level of merger of two precipitation features over the Coast Range and the Sierra Nevada mountains that was observed in AMIP simulations of CAM Eulerian Spectral T170 was not visually apparent in the double mountain setup (Figure 12). However the k=2 clustering quantified the relatively high level of merger for CAM Eulerian Spectral T170 by identifying the area between the two mountains as "rain-area", whereas both CAM FV 1 degree and 0.5 degrees resolutions produced a dryer region between the mountains (Figure 20).

We were able to quantify the tendency of spectral models to spread out precipitation by examining the difference between k=2 and k=3 clustering results. As shown in Figure 8, the "light rain" area for CAM Eulerian Spectral T170 for the smaller large-scale stable upslope feature (object 2) is bigger than that of CAM FV 0.5 degrees. This difference reflected to the difference between k=2 and k=3 clustering SVs (Figure 24f), which is larger than that of FV's.

We also evaluated the utility of SVs applied to isolated objects rather than to a whole precipitation field. Our synthetic data analysis showed that SV plots carry information about an objects magnitude, size, and location. This characteristic of SVs led us reveal the effect of the downwind mountain on the simulation of the precipitation due to the upwind mountain. The shift in the 3rd SV peak (Figure 21) between the single mountain

73

and double mountain setups is a quantitative indication of the change of size of the object 1. We were also able to show how the double mountain setup simulated object 1 in lower intensity relative to the single mountain setup from the difference of the scales of the SVs for both setups (Figure 21). This shows the utility of SVs in quantifying the differences, which are not visually apparent. However, there is also an inherent ambiguity in SVs in terms of object-based analysis. One shortcoming is that the SVs tend to aggregate the objects in calculations when the objects are small and close to each other (as in the case of the realistic setup SVs shown in Figure 23. Another potential ambiguity is that if two or more characteristics of an object (e.g., size and location) are close to each other, SVs tend to show them on a single peak or bend, which makes the evaluation difficult especially for simulations with coarse resolution. Therefore a more efficient evaluation measure may be required to quantify the differences between objects that are similar to each other, and simulated by coarse resolution models.

CHAPTER 4: QUANTITATIVE ANALYSIS PART II: Daily Simulation Analysis with Classification Trees

The quantitative analysis with k-means clustering and semivariograms (SVs) revealed important characteristics of the large-scale stable upslope precipitation features simulated by the CAM Eulerian Spectral and CAM FV models, and the differences between the simulations. However, a complete analysis requires evaluation and comparison of the small-scale features due to local evaporation and lee-side convergence as well as the grid scale variability. Examining the daily simulations of CAM Eulerian Spectral T85, T170 and CAM FV 1 degree, and 0.5 degrees allows quantification of the daily evolution of the small-scale features. These small-scale features introduce difficulty in terms of their identification and isolation from the whole field due to their size and proximity to other large and/or small-scale features (Figure 10). K-means clustering tends to merge these small-scale features to the large-scale features, or aggregate the precipitation in the vicinity of the small-scale feature to form a larger cluster, which is not desirable from an object-based point of view. Therefore an ad hoc pattern recognition technique using classification trees is developed to have more control on the object identification step in order to separate each feature sensibly. The developed method also allows flexible thresholding depending on the characteristics of the features to be isolated. The details of the classification tree algorithm are given in the next section (4.1). Due to the ambiguity of semivariograms (SVs) in quantifying object characteristics discussed in the previous section, simple statistical measures (i.e., mean, variance, peak value) were used to compare the isolated features across all simulations. Once the features are isolated as objects, they are removed from the whole precipitation field and the remaining "background" precipitation is analyzed with SVs to compare the grid-scale variability of the CAM Eulerian Spectral and CAM FV simulations.

4.1. Method

A classification tree (Breiman et al. 1984) algorithm was implemented for identification and isolation of precipitation features simulated in idealized test cases. Classification trees is a machine learning method for constructing prediction models from data by recursively partitioning the data space and fitting a simple model into each partition. Given a class variable (Y) with values 1, 2, …, k, and p predictor variables (X_1, X_2, …, X_p), a classification strategy aims to construct a model to predict the class value of Y from values of X. The solution is a partition of the X space into k disjoint sets S_1, S_2, …, S_k, such that the predicted value of Y is j if X belongs to S_j for $j = 1, 2, …, k$. Classification trees yield rectangular sets S_j by recursively partitioning the data field on X (Loh 2011).

The data field (in our case the precipitation rate) is partitioned into rectangular boxes that are called nodes. The initial field (the root node) is split into a series of parent and leaf nodes, where each parent node is split into two leaf nodes. The splitting is done until a stopping criterion is met for a leaf node in which case the leaf node is called a terminal node. Both the split and the stopping decisions are made via an impurity measure. The measure of node impurity is based on the distribution of the observed Y values in the node. Our algorithm finds a subset over all X values for the split that minimizes the difference between the impurity of the node and the impurity of its two leaf nodes. An example classification tree of a precipitation field simulated by CAM FV 0.5 degrees is given in Figure 25.
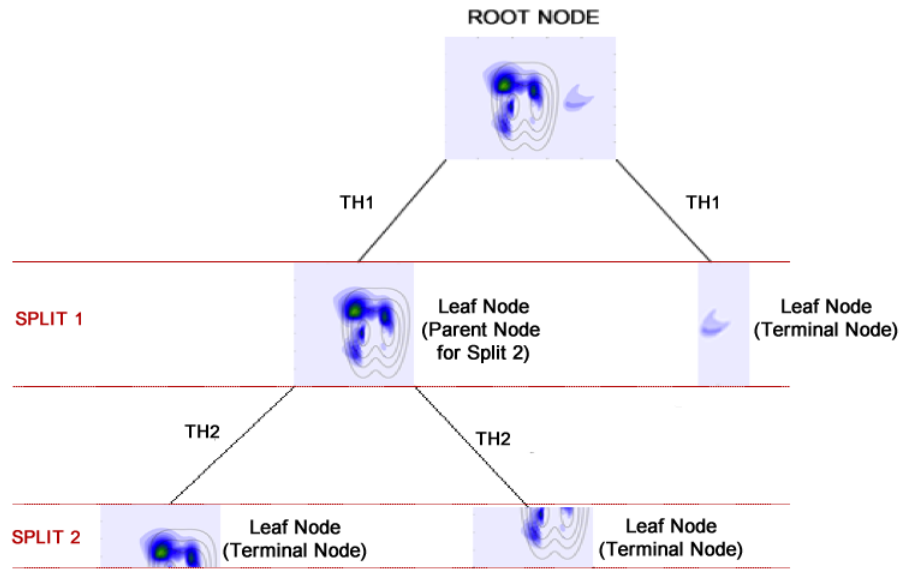
Figure 25: *An example classification tree with 2 rectangular splits at day 15 total precipitation rate for the double mountain case, simulated by CAM FV 0.5 degrees. TH is threshold.*

Only 2 splits are shown in Figure 25 for presentation purposes. The root node is the initial precipitation field for the double mountain case simulated by CAM FV 0.5 degrees. The first split is done over a longitude line, which partitions the initial field such that the large-scale upslope ascent and the small-scale local evaporation and lee-side convergence features remain in one node (westward of the split boundary), and the feature due to the leeward waves remain in the other (eastward of the split boundary). The resulting two nodes of split 1 are both leaf nodes of the root node (i.e., the combination of the two leaf nodes gives the root node). In this example it is assumed that the impurity measure (explained below) of the node containing the feature due to the leeward baroclinic wave meets the stopping criterion, therefore it can also be labeled as the terminal node. A further split is done over the node containing the large and small-scale features; therefore it can also be labeled as the parent node. The second split is done over a latitude line on the parent node resulting from split 1, which separates the small-scale features in one node, and the large-scale features on the other. Both nodes are the

77

leaf nodes of their parent node, however there are no more splits in this example so they can also be labeled as terminal nodes. As can be seen in Figure 25, there are two threshold values employed for each split (TH1 and TH2). The decision of these threshold values, the decision of the longitude (or latitude) line as the split boundary due to an impurity measure, and the decision of stopping criteria after each split are the key factors in the formation of such a classification tree. These factors are explained in detail by looking at the first split given in Figure 25.
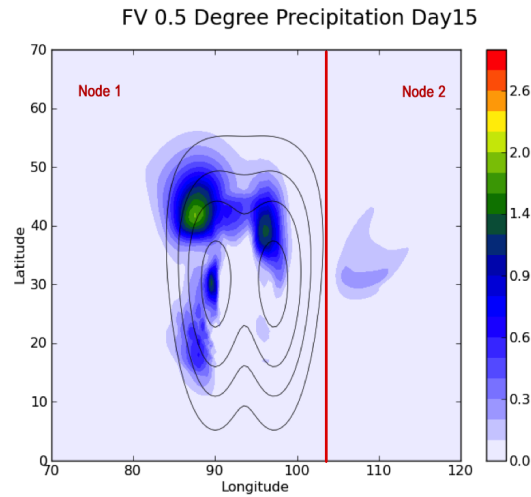
Figure 26: Day 15 total precipitation rate, surface geopotential (topography) for double mountain case, simulated by FV 0.5 degrees. The longitudinal split boundary is shown with the red line.

In Figure 26, the whole precipitation field is the root node and is split into two leaf nodes at longitude 104° W. For each partition, the algorithm calculates the impurity of each node via a measure called Gini index:

$$Gini(node) = \sum_{y=1}^{Y} p_y(1 - p_y) \tag{24}$$

where p_y is the frequency of occurrence of grid-points belonging to class y. We defined 2 classes (Y=2) in our calculations, one being the rain (i.e., the grid-point that belongs to the object of interest) the other being the non-rain (i.e., any grid-point outside objects).

The classes and the corresponding node impurities are defined via thresholds. The decision of the split is done via maximizing the Qsplit parameter:

$$Qsplit =$$

$$Impurity(parent) - \left[\frac{N_{node1}}{N_{parent}} Impurity(node1) + \frac{N_{node2}}{N_{parent}} Impurity(node2)\right] \quad (25)$$

where N_{parent}, N_{node1}, N_{node2} are the total number of grid-points included in the parent node and subsets of leaf nodes (nodes 1 and 2) respectively. Each impurity value (i.e., the impurity values for parent, node1, and node2) in equation 25 is calculated by the Gini index given in equation 24. The split in Figure 26 is achieved via maximizing the Qsplit with the threshold value of 0.5 mm/day (i.e., if a grid-point value is above 0.5 mm/day it is considered rain class, if it is below this threshold it is considered non-rain class). After this first split, the algorithm continues to split each leaf node until all the resulting nodes become terminal, which is decided when the impurity of nodes drops below a certain value (i.e., until they become pure). The spilt is done sequentially in latitudes and longitudes (if the first split is in longitudes, then the second is in latitudes, third is in longitudes etc.), however this sequence can be changed depending on the user's choice.

This nature of classification trees that allow step-by-step splitting of the root node into terminal leaf nodes allows the resetting of the threshold value according to the characteristics of each parent node. In Figure 26, node 1 includes two types of features discussed in chapter 2, namely the large-scale upslope ascent feature and the small-scale feature due to local evaporation and lee-side convergence, whereas node 2 includes the feature due to the leeward waves. These features are different in their manifestations, characteristics and evolutions in time, therefore they should not be attempted to be classified with the same threshold. The algorithm objectively calculates the threshold before each split by looking at the statistics of the parent node to be split. In this study the threshold is defined by adding half of the standard deviation of the node to the mean

value of the node. This measure can be changed according to the nature of the problem, however in our case this calculation gave a sensible identification of classes.

As indicated previously, the decision tree algorithm partitions the initial field into rectangular boxes. This introduces a limitation to our problem since the precipitation features are not rectangular. Depending on the threshold value, the algorithm may split a precipitation feature into more than one rectangle by chopping off the edges of the curved feature. A post processing was conducted to overcome the issue where we reconstructed the split features -if any- into the original form. We used information from the topography field for that purpose. The qualitative analysis (Chapter 2) gave information about the locations of each type of feature, therefore the terminal nodes, which are exactly over the peak of mountains are aggregated to form the small-scale features due to local evaporation and lee-side convergence. The other two types of features are formed in the same manner by measuring the node distances to mountain peaks. This flexibility of the algorithm also allows the usage of other information (e.g. moisture flux convergence, winds) if needed.

The identification and extraction of the features with the classification tree algorithm was applied to daily precipitation results for a total model run time of 30 days. Once the features were extracted, some simple statistical analyses (e.g. mean values, peak values, variances) were conducted and the results were compared for all four simulations which are discussed in the next section.

4.2. Statistical Comparison of Isolated Features (Objects)

The classification tree algorithm is applied to the daily simulations of the double mountain and the realistic setups of the idealized simulations. Our comparison focuses on the large-scale upslope ascent features and the small-scale features due to local

evaporation and lee-side convergence simulated by CAM FV 1 and 0.5 degrees, and CAM Eulerian Spectral T85 and T170 triangular truncation resolutions.
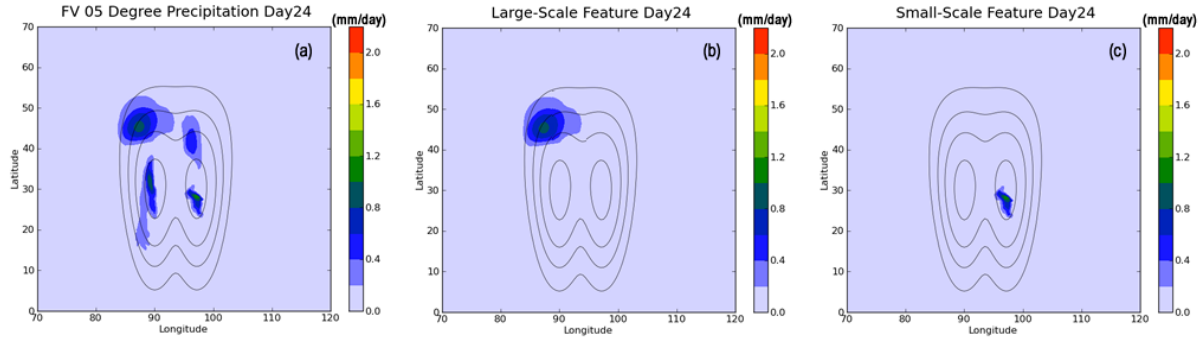
Figure 27: *Day 24 total precipitation rate, surface geopotential (topography) for the double mountain case, simulated by (a) CAM FV 0.5 degrees. The isolated large-scale stable upslope ascent feature on the windward mountain and the small-scale feature on the leeward mountain are shown in b and c respectively.*

An example of how the algorithm partitions the precipitation field simulated by CAM FV 0.5 degrees for the double mountain setup is given in Figure 27. The algorithm was able to identify and isolate the large-scale upslope ascent feature (Figure 27b) and the small-scale local evaporation and lee-side convergence feature (Figure 27c). The large-scale feature in front of the windward mountain and the small-scale feature on the leeward mountain are selected to be included in our evaluation. The analysis on the large-scale feature in front of the leeward mountain and the small-scale feature on the windward mountain (not shown) produced similar results to those included in this study; therefore they are excluded to avoid repetitive results. The algorithm was also applied to CAM FV 1 degree and the CAM Eulerian Spectral T85 and T170 simulations of the double mountain case and the precipitation features were successfully isolated (not shown). Then the peak value, the mean value and the variance for the isolated features were calculated within the enclosed object boundaries for each day over 30 days of simulation time.
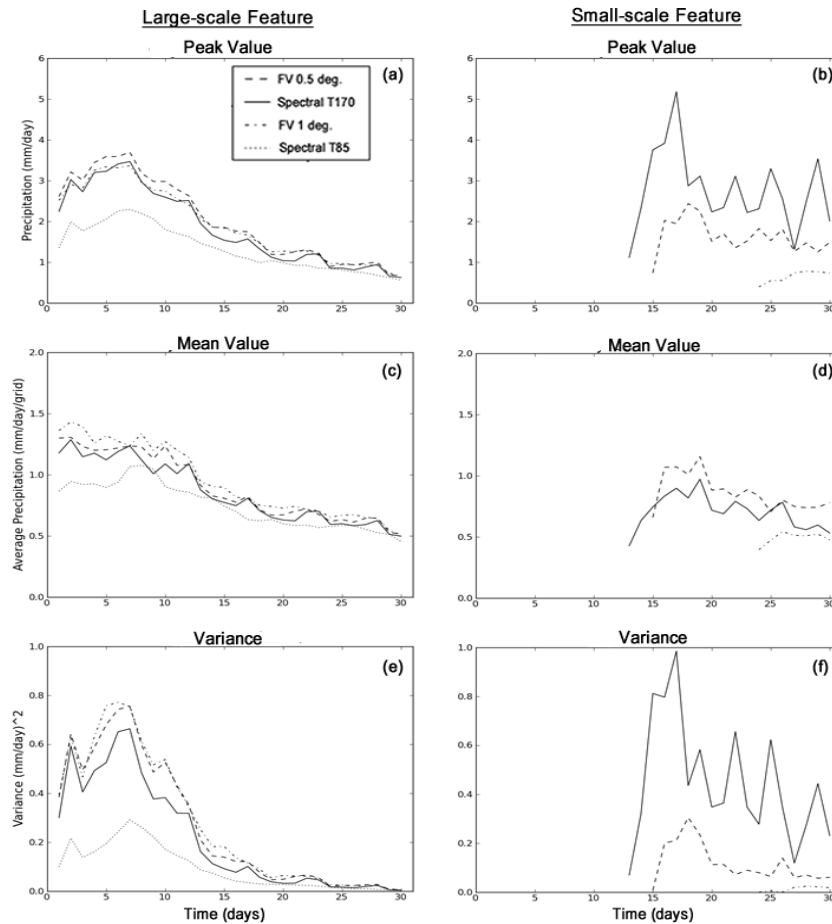
Figure 28: *The peak value, mean value and the variance for the large-scale stable upslope ascent feature on the windward mountain (a,c,e), and the small-scale local evaporation and lee-side convergence feature on the leeward mountain (b,d,f) for the double mountain setup, simulated by all four models.*

The results for the large-scale stable upslope ascent feature (Figures 28a, 28c, and 28e) show close agreement between CAM FV 1 and 0.5 degrees, and the CAM Eulerian Spectral T170 models, however there is a disagreement for CAM Eulerian Spectral T85 results (the dotted line). CAM Eulerian Spectral T85 simulated this large-scale feature with lower intensity, which is in agreement with our qualitative analysis. Figure 28e shows that CAM Eulerian Spectral T85 also produced lower values of variance whereas the other simulations exhibit a peak variance in the beginning and between day 5 and day

10. Note that the variance is calculated over the values within the boundaries of the objects determined by the classification tree algorithm; therefore low values of variance indicate a smoother feature without a distinct peak of precipitation. This peak precipitation (therefore higher values of variance) is expected for a stable upslope precipitation feature given the nature of such features (Roe 2005), where there is a peak precipitation value together with lower values (Figure 3). The variance results also show how both CAM FV resolutions (dashed lines) agree closely with each other yielding slightly higher values than that of CAM Eulerian Spectral T170. The results start to converge for all models after day 15 for the large-scale stable upslope feature as it loses intensity and the amount of rain produced is reduced.

The agreement of model simulations for the large-scale upslope ascent feature is not observed for the small-scale local evaporation and lee-side convergence feature (Figures 28b, 28d, and 28f). The onset time of this small-scale feature is different for all four simulations (i.e., day 13 for CAM Eulerian Spectral T170, day 15 for CAM FV 0.5 degrees, day 24 for CAM FV 1 degree). CAM Eulerian Spectral T85 did not simulate this feature within the 30-day simulation time, however a 45-day run was made and it was observed that spectral T85 simulated this feature starting at day 37. Except from the CAM Eulerian Spectral T170, the onset time of this type of feature shows a correlation with model resolution (i.e., the higher the resolution, the earlier the onset). CAM Eulerian Spectral T170, however, starts simulating this object the earliest, but with an erratic behavior. It starts with low peak and variance values (Figures 28b and 28f), with an abrupt increase afterwards and an oscillatory behavior until the end of the simulation with significantly higher values compared to both CAM FV resolutions. This result agrees with the over-representation of precipitation by spectral models shown by Williamson and Rasch (1994) given in section 1.2. On the other hand, CAM FV 1 and 0.5 degrees resolution simulations exhibit relatively stable behavior, keeping similar peak, mean and variance values throughout the simulations. The mean values (Figure 28d) for CAM Eulerian Spectral T170 are stable throughout the simulation time. The mean values are

calculated such that the precipitation rate is summed over all grid points and divided by the number of grid points within the boundaries of the object. A qualitative examination of the isolated small-scale local evaporation and lee-side convergence features shows that CAM Eulerian Spectral T170 simulates these features over a larger spatial extent, therefore the mean values of CAM Eulerian Spectral T170 are comparable to CAM FV 0.5 degrees even though CAM Eulerian Spectral T170 produces higher peak precipitation rates. High variance values (i.e., high and low values enclosed within the object) for CAM Eulerian Spectral T170 also support the agreement in the mean values between CAM Eulerian Spectral and CAM FV.

The results shown in Figure 28 give a quantitative picture of how resolvable scales of precipitation features affect the simulation performance of the CAM FV and CAM Eulerian Spectral dynamical cores. The results for the more realistic idealized setup with smaller scales in the horizontal give a better picture of how these dynamical cores simulate both large-scale and small-scale objects.
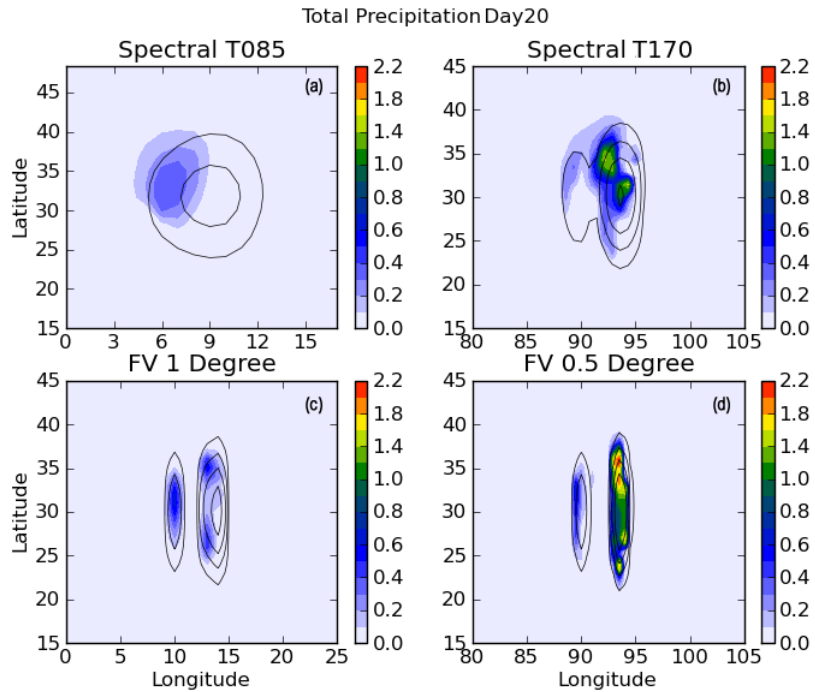
Figure 29: *Day 20 total precipitation rate (mm/day), surface geopotential (topography) for the realistic case, simulated by (a) CAM Eulerian Spectral T85, (b) CAM Eulerian Spectral T170, (c) CAM FV 1 degree, and (d) CAM FV 0.5 degrees. Surface geopotential contours are 500, 2.000, 5.000 and 11.000 m^2s^{-2}, with the peak contour at the interior of the mountain.*

Figure 29 shows the day 20 total precipitation rate simulated by the CAM Eulerian Spectral T85 and T170, CAM FV 1 degree and FV 0.5 degrees for the realistic idealized setup. As discussed in chapter 2, there are significant differences in the simulated precipitation between CAM Eulerian Spectral and CAM FV models due to the topography filter in CAM Eulerian Spectral models and the smaller horizontal scales of mountains in the realistic case. We focus on the large-scale upslope ascent and the small-scale local evaporation and lee-side convergence features simulated on the leeward mountain by finer resolution simulations (CAM Eulerian Spectral T170 and CAM FV 0.5 degrees). As seen in Figures 29b and 29d, the precipitation features simulated on the leeward mountain creates a complex structure unlike the single and double mountain setups where these features are not merged due to the large size and separation of

mountains. The large-scale and the small-scale features almost merge into each other over the leeward mountain in the realistic case, which makes it harder to distinguish and isolate these different features separately. However, the classification tree algorithm was able to isolate each feature successfully by the precipitation value patterns, without the need of additional information from other fields such as winds or moisture flux convergence.
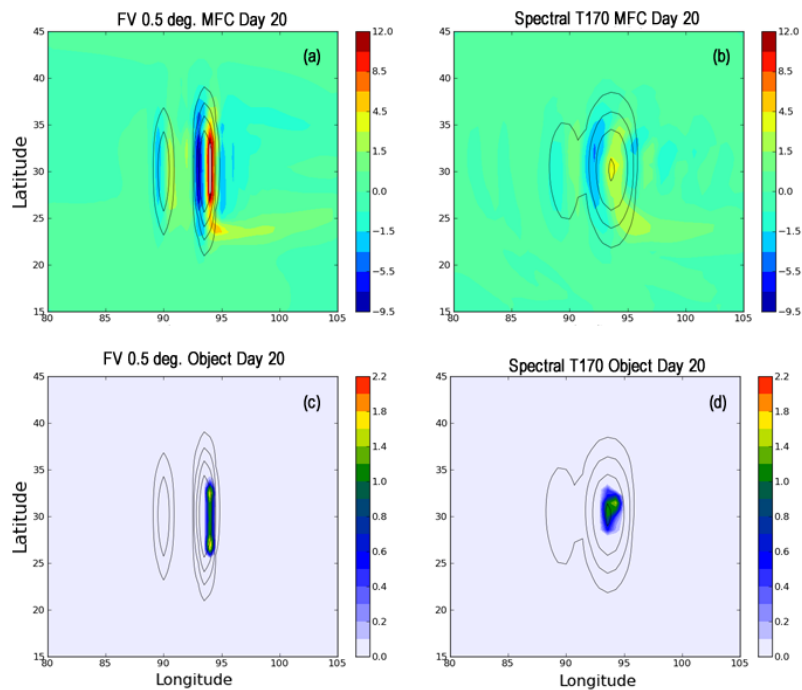
Figure 30: *Day 20 moisture flux convergence (10^{-4} kg $m^{-2}s^{-1}$) by (a) CAM FV 0.5 degrees, (b) CAM Eulerian Spectral T170 and their related precipitation (mm/day) objects (c, d) isolated by the classification tree algorithm. Surface geopotential contours are 500, 2.000, 5.000 and 11.000 m^2s^{-2}, with the peak contour at the interior of the mountain.*

Figure 30 shows the precipitation features objectively isolated by the classification tree algorithm for CAM FV 0.5 degrees and CAM Eulerian Spectral T170 (Figures 30c and 30d). The corresponding moisture flux convergence (MFC) plots (Figures 30a and 30b) shows the overlap of the isolated features with the positive MFC areas. The vertical

pressure velocities (OMEGA) for the domain given in Figure 30 (not shown) indicate no overlap of updrafts with the isolated precipitation features. Therefore, these features are not related to stable upslope ascent but rather the local evaporation and lee-side convergence features the classification tree algorithm isolated from the whole precipitation field. The peak and the mean values as well as the variances are calculated for these isolated features (Figure 31).
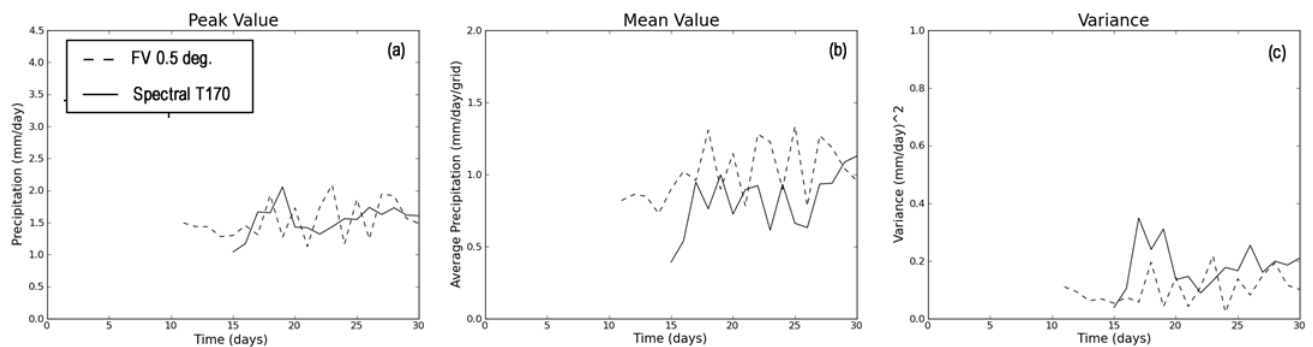
Figure 31: (a) The peak value, (b) mean value, and (c) the variance for the small-scale local evaporation and lee-side convergence features for the realistic setup shown in Figure 30, simulated by CAM FV 0.5 degrees and CAM Eulerian Spectral T170.

In this case there is better agreement between the CAM FV 0.5 degrees and CAM Eulerian Spectral T170 simulated small-scale local evaporation and lee-side convergence features compared to their analogues in the double mountain setup (Figures 28b, 28d, and 28f). In the realistic case, the onset of the small-scale feature is earlier for CAM FV 0.5 degrees, which was not the case for double mountain setup. This strengthens the argument about the correlation between the resolution and the time of the onset mentioned previously. The mean values for CAM FV 0.5 degrees are higher than that of CAM Eulerian Spectral T170 (Figure 31b), which is also not the case for the double mountain setup (Figure 28d). However, in the realistic case the peak, mean values and the variance for CAM Eulerian Spectral T170 exhibit an abrupt increase right after the onset of the small-scale feature suggesting an initial instability. The quantitative analysis given

in Figure 31 shows that, unlike in the double mountain case, both CAM Eulerian Spectral T170 and CAM FV 0.5 degrees simulated similar small-scale local evaporation and lee-side convergence features. The biggest difference is at the spatial extent where CAM Eulerian Spectral T170 bulged the feature due to the shape of topography (Figure 30d). These results suggest that it is not only the horizontal spatial scales that contribute to the performance of a model, because even though the realistic case has relatively smaller horizontal scales, the simulations of the fine resolution CAM FV and CAM Eulerian Spectral models for this case are more similar (Figure 31). However in the realistic case, the height of the leeward mountain is doubled (1500 m for the double mountain case, 3000 m for the realistic case) and this increase in the vertical scales have affected the CAM Eulerian Spectral T170 simulation of the small-scale features.

Better agreement between the results of CAM Eulerian Spectral T170 and CAM FV 0.5 simulations for the realistic setup small-scale features shows that there is a higher amount of numerical noise introduced by CAM Eulerian Spectral T170 for the double mountain setup small-scale features given the erratic behavior of that schemes results (Figures 28b, 28d, and 28f). A relatively lower MFC is observed at the peak of the leeward mountain of the realistic case (Figure 31b) than that of the double mountain case (not shown) for CAM Eulerian Spectral T170. Therefore the amount of moisture is also effective in the simulation of precipitation for spectral models where a higher amount of moisture within a smaller area forced CAM Eulerian Spectral T170 to produce unrealistic simulations. In chapter 2, we showed that these small-scale features are influenced by the constant sea surface temperature (SST) set in the initial conditions of the idealized setups. Therefore we conducted an additional model run with reduced SST value of 287 K (instead of 288 K which is set for all the experiments presented so far) for the double mountain setup to investigate its effect on the simulation of the small-scale local evaporation and lee-side convergence features by CAM FV 0.5 degrees and CAM Eulerian Spectral T170.
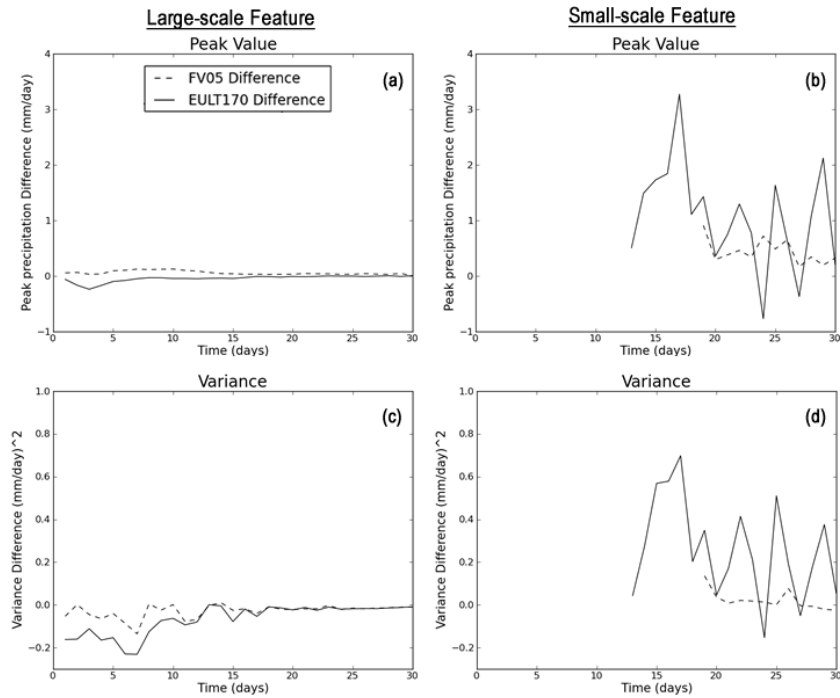
Figure 32: *The peak value, and the variance difference (288 K – 287 K SST runs) for (a,c) the large-scale stable upslope ascent feature on the windward mountain, and (b,d) the small-scale local evaporation and lee-side convergence feature on the leeward mountain for the double mountain setup, simulated by CAM Eulerian Spectral T170 and CAM FV 0.5 degrees.*

Figure 32 shows the daily difference between the 288 K SST minus the 287 K SST run peak values and differences for large-scale stable upslope ascent feature (Figures 32a and 32c) and the small-scale local evaporation and lee-side convergence feature (Figures 32b and 32d) simulated by CAM Eulerian Spectral T170 and CAM FV 0.5 degrees for the double mountain setup. The large-scale feature is minimally affected by the change in SST for both CAM Eulerian Spectral and CAM FV models since this feature is manifested through airflow over (and around) the mountains rather than surface temperature. However, the affect of the SST change is apparent for CAM Eulerian Spectral T170 for the small-scale feature (Figures 32b and 32d). The positive difference in both peak and variance for CAM Eulerian Spectral T170 is significant especially after the onset of the small-scale feature, with continued oscillations throughout the end of the simulation. The difference for CAM FV 0.5 degrees is relatively lower and more stable.

In order to investigate the grid-scale behavior in the double mountain case, we subtracted the isolated features from the whole field of precipitation (i.e., 0-70° North, 10-120° East) simulated by the CAM FV and CAM Eulerian Spectral models. Semivariograms (SVs) are employed for this comparison to analyze the spatial continuity for the remaining irregularly spaced grid points. Grid values below 0.01 mm/day were excluded from the analysis. Examples of the fields for CAM FV 0.5 degrees and CAM Eulerian Spectral T170 for 6th day of the simulation with 288K SST, and their corresponding omni-directional SVs are given in Figure 33.
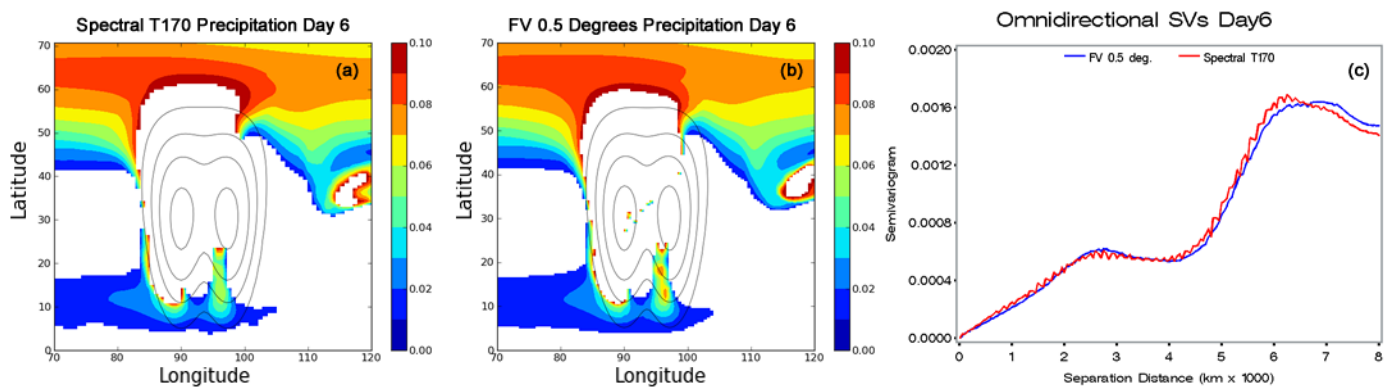
Figure 33: *The remaining precipitation rate (mm/day) fields after subtracting the isolated features and grid points with values below 0.01 mm/day for (a) CAM Eulerian Spectral T170, and (b) CAM FV 0.5 degrees. Both plots are from the 6th day simulation of the double mountain setup with SST = 288 K. The omni-directional SVs (mm/day)^2 for both simulations are given in (c). Surface geopotential contours are 500, 2.000, 5.000 and 11.000 m^{2}s^{-2}, with the peak contour at the interior of the mountain.*

The separation distance intervals (i.e., the lag classes explained in section 3.1.2) over which the SVs (Figure 33c) are calculated such that they are increments of 55 km for CAM FV 0.5 degrees and 70 km for CAM Eulerian Spectral T170, which are the respective grid sizes for each dynamical core. There is a close agreement between hhe SVs of CAM FV 0.5 degrees and CAM Eulerian Spectral T170 in Figure 33. This agreement is due to the similarity of the remaining precipitation fields (Figures 33a and

33b). The SVs of the two dynamical cores start to depart from each other as the simulation proceeds after day 15. However, the grid scale oscillatory behavior of the CAM Eulerian Spectral T170 observed in Figure 33c is consistent throughout the 30-day simulation, whereas the SVs of CAM FV 0.5 degrees is smooth indicating higher spatial continuity. This contrast between the two dynamical cores indicates the systematic grid-scale noise introduced by CAM Eulerian Spectral models. In particular, The SV values at ~70 km for CAM Eulerian Spectral T170 are consistently higher than the SV values at ~55 km for CAM FV 0.5 degrees (12.0×10^{-6} and 28.4×10^{-6} mm/day^{-2} for CAM FV and CAM Eulerian Spectral models respectively. This means higher variability of precipitation values for spectral model on the grid-scale.

4.3. Summary of the Daily Simulation Analysis

Daily simulations of CAM Eulerian Spectral T170 and T85, CAM FV 1 degree and 0.5 degrees resolutions for the double mountain and the realistic setups were analyzed in this section. A classification tree algorithm that allows flexible thresholding was implemented to identify and isolate the small-scale precipitation features (as well as the large-scale features). The isolated features were compared by simple statistics across all simulations.

The classification tree algorithm proved successful in sensible isolation of precipitation features even within a complex precipitation field as observed in the realistic case results. The relatively small spatial scales of the mountains in the realistic case led to the manifestation of different types of precipitation features over a smaller area. These features merged to form a complex and highly structured field, which makes it difficult to observe each type of feature visually. However, the classification tree

algorithm was able to extract different types of features from this complex field by detecting the patterns of the precipitation values.

The quantitative results showed different behavior between CAM FV and CAM Eulerian Spectral models for different precipitation features. The close agreement between CAM Eulerian Spectral T170 and the CAM FV models at the two resolutions in the case of large-scale stable upslope ascent features was not observed for the small-scale features for the double mountain setup. The disagreement of the coarse resolution CAM Eulerian Spectral model (T85) was already discussed in chapter 2 where it is found out that the spectral filtering of the topography is the primary cause of this disagreement. However, the disagreement of the fine resolution models (i.e., CAM Eulerian Spectral T170 and CAM FV 0.5 degrees) shown in Figures 28b and 28f is due to the amount of moisture introduced by surface fluxes of the simple-physics parameterization. This is supported by the results of the realistic case where there is less local evaporation on the relatively high leeward mountain leading to better agreement in simulation of the small-scale features by CAM Eulerian Spectral T170 and CAM FV 0.5 degrees (Figure 31). The experiments with decreased SST (Figure 32) also show how the increased moisture input from the surface affect the simulation of the small-scale features by CAM Eulerian Spectral T170 significantly more than CAM FV 0.5 degrees. The simulation of the large-scale features was less affected by the change in SST since the mechanism responsible for their manifestation (stable upslope ascent) is related to the upward movement of air rather than local surface fluxes. Therefore it can be concluded that there is numerical noise introduced by the spectral transform scheme in the case of the small-scale features for the double mountain setup. When the simulations are physical with less numerical noise (as in the case of the realistic setup in this study), it is observed that there is a correlation between the resolution and the onset time of the small-scale features, i.e., the higher the resolution, the earlier the onset.

Finally, the isolated objects were removed from the field and semivariograms were calculated to the remaining irregularly spaced grids to quantify the grid-scale variability of both CAM Eulerian Spectral T170 and CAM FV 0.5 degrees. It is observed (Figure 33c) that there is systematic numerical noise introduced by the spectral transform method at the grid-scale, which adds to the disagreement of CAM FV and CAM Eulerian Spectral models in the case of both large and small-scale precipitation features.

CHAPTER 5: CONCLUSIONS

The primary objective of this dissertation is to help improve the simulation of future climate by GCMs with better understanding and quantification of the particular biases these models introduce. Due to the highly complex nature of the earth's climate system, its simulation with mathematical models is equally complicated with many different subcomponents responsible for different natural phenomena. The output of such a system is produced by the combination of these subcomponents, therefore any bias in the output, systematic or not, have contributions from such combination. This nature of the state-of-the-art climate models makes it difficult to pinpoint the origins of any particular bias and renders the problem of understanding their causes and effects a complicated task. This study undertakes that task by breaking down the problem into simpler parts to identify, isolate and analyze the particular bias. Precipitation rate is chosen as the variable of interest since it is problematic to simulate by GCMs due to its highly discontinuous nature and complex underlying physics, as well as its importance in the climate system. To further narrow the focus on the bias in simulation of precipitation, local scales were selected to analyze with a focus on precipitation over mountains. In summary, the approach of this study involves analyzing and quantifying the behavior of simulated orographic precipitation and with the aid of the knowledge about the GCM subcomponent(s) that are responsible for its simulation, understand the nature of the associated bias. Idealized topographical setups using the simple-physics parameterization suite (Reed and Jablonowski 2012) were created to analyze the different types of bias in a simplified environment. Two different dynamical cores (FV and spectral) within the NCAR CAM 5.0 were compared in terms of their simulation of orographic precipitation.

An object-based approach was developed and implemented to identify the bias introduced by the dynamical core with a focus on its interaction with physical parameterizations, and the evolution of bias with changing resolution. As the first step of the object-based approach, a local precipitation feature (study feature) that is consistently simulated differently by CAM Eulerian Spectral and CAM FV models within AMIP simulations was selected (Figure 6). As the second step of the object-based approach, the selected feature was reproduced in a simplified environment resembling the topographic characteristics of the study domain (i.e., Coast Range and Sierra-Nevada) coupling spectral and FV dynamical cores in CAM 5.0 (Neale et al. 2010) with the simple-physics parameterization. The experimental model runs revealed that the models also produce small-scale features as well as the large-scale features, which are the selected study features in the first. Both type of features are products of different physical and dynamical phenomena, therefore different model components are responsible for their simulation and the bias associated with them. The third step of the object-based approach is implemented to quantify and understand these biases. Both large and small-scale features are identified and isolated using two different methods: a conventional method (k-means clustering) on monthly mean results, and a non-conventional algorithm using classification trees on daily results. After the identification and isolation of the features, they were matched with their analogues between models and quantitatively compared using a geostatistical method (variography), and simple statistics (e.g., peak, mean and variance values). In the remainder of this section, the utility of these methods in terms of GCM bias identification is discussed and then the findings of the particular biases identified are presented.

As explained in the introduction chapter, one of the objectives of this study is to develop an object-based quantitative method to identify biases in GCMs, which can be generically applicable to GCM output. The previously developed object-based methods suffered from the disadvantage of user-defined threshold limitation for the object 'identification' step, and the loss of information due to averaging with statistical

95

comparison using measures such as root mean squared error (RMSE) and correlation coefficient in the subsequent object 'evaluation' step. To address and remedy the user-defined threshold limitation, two different methods, namely k-means clustering and classification trees were implemented for object identification. Both methods allow objective and flexible thresholding to identify and isolate features using the statistical characteristics of the field of interest. However, k-means clustering has three main disadvantages when compared to classification trees in identification of features simulated by GCMs. One of the disadvantages is the non-uniqueness of the k-means clustering solutions. This limitation has not been a significant problem in the scope of this study since the features of the idealized test cases to be isolated were distinct and mostly separated from each other. However, in the case of a smoother field (e.g., winds) the lack of unique solutions will result in different feature (object) boundaries (This has been observed when k-means clustering was applied to a potential vorticity field as a side study). One remedy to this problem in clustering is to make a number of calculations to form the clusters and choose the most common solution. However this will introduce significant amount of computational expense that will make the quantification effort unfeasible especially in the case of large amounts of data produced by GCMs. Another disadvantage of k-means clustering is its tendency to agglomerate the grids of similar values close to each other to form a single cluster. This is an inherent characteristic of the clustering procedure, however there are situations where it is undesirable in the case of simulated climate variables such as the small-scale feature shown in Figure 30. The small-scale feature due to local evaporation and lee-side convergence in Figure 30 is not completely separated from the precipitation surrounding it, so k-means clustering produced a larger object boundary, which included the surrounding grid-points (not shown). However, the classification tree algorithm was able to isolate the values related to the positive moisture flux values and extract the corresponding feature from the surrounding precipitation by using the impurity measure of precipitation values. The final limitation that k-means clustering has is the lack of flexibility to use information from other fields (e.g., topography, winds etc.) when identifying object boundaries. It is hard to

identify such boundaries especially when dealing with smoother fields like temperature and winds, therefore using information from other variables that are responsible for the spatial organization of the variable of interest is required. One disadvantage of classification trees, which is the ability of partitioning the field only in rectangles, was compensated by the introduction of information from the topography. Precipitation features of the idealized test cases (and in general) are circular in their spatial orientation, thus the classification trees usually isolate the interior rectangular area and remove the edges. The removed edges were then added to the rectangles to reconstruct the feature using their distance to mountain peaks.

Semivariograms, geostatistical measures for spatial continuity of a regionalized variable, were employed when comparing identified objects between CAM Eulerian Spectral and CAM FV dynamical cores. The application on synthetically created data showed that semivariograms carry information about an objects magnitude, size and location, which makes it a superior measure of evaluation to the traditional grid-point-by-grid-point comparison methods. Semivariograms simplifies the analysis needed to evaluate objects by indicating information on a single plot, thereby eliminating the need for separate analysis on size, shape, location, magnitude etc. Application of semivariograms on large-scale upslope ascent precipitation features revealed important information about the behavior of these features (e.g., the effect of the circulation between two mountains on the feature in front of the windward mountain, the shift in the location of features etc.). However, semivariograms have limitations due to inherent averaging in their calculation. The method tends to show signature of similar spatial characteristics of an object (such as similar distances of an objects size an location) with the same peak or bend on a semivariogram plot. This method is also ineffective on showing characteristics of small-scale features close to each other, since it tends to treat them as one single-large scale object. Therefore, the usage of this method is recommended preferably on large-scale features with apparent characteristics to eliminate any possible ambiguity in results.

The results of this study suggest that an efficient and informative study about the biases produced by GCMs should involve daily (or even hourly) output (rather than monthly mean) analysis over local scales. Small-scale features such as the ones identified due to local-evaporation carry significant information about the biases originating by their corresponding physical parameterizations and numerical schemes. These features are lost in monthly mean plots due to averaging (Figure 9). This is also important for analyzing "local" scales where significant bias can manifest in GCM simulations as explained in the introduction part. Our study showed that analyzing local features rather than a whole precipitation field gives more accurate insight about the nature of bias. A good example of this is shown in Figure 32, where two different types of features over the mountains of the same model run (double mountain case) show significant difference in their evolution over time due to the bias introduced for the small-scale feature. The small-scale feature has a completely different mechanism of manifestation (i.e., local evaporation and lee-side convergence), and isolating these features separately gives insight about the bias related to that mechanism, how it is parameterized, and how the parameterization is coupled with dynamics.

In summary, the object-based approach with focus on local phenomena let us quantify the differences between CAM Eulerian Spectral and CAM FV models in simulation of orographic precipitation and evaluate how this difference evolves with increased resolution. We were able to understand the causes of the difference of CAM FV and CAM Eulerian Spectral models in simulation of the study features (Figure 6). One prominent conclusion of this study is that the resolvable spatial scales of precipitation features to be simulated play a crucial role in how they will be simulated by GCMs. This is naturally related to the scales of the mountains involved in the simulation. Throughout the discussion of the results, it has been clear that the simulation of large-scale features due to stable upslope ascent was in agreement between CAM Eulerian Spectral and CAM FV model with the exception of CAM Eulerian Spectral T85. However the quantitative

characteristics of the simulated small-scale features by CAM FV and CAM Eulerian Spectral models did not converge. The reasons for this difference, or in other words, the reasons why the CAM Eulerian Spectral models failed to simulate precipitation features in agreement with CAM FV models and observations as seen in the AMIP runs (Figure 6) can be summarized under 3 categories:

1. Bias due to spectral filtering of the topography
2. Bias in small-scale phenomena due to spectral transform method
3. Grid scale variability (noise) due to spectral transform method

Bias due to spectral filtering of the topography in the CAM Eulerian Spectral Transform dynamical core is a global source of bias, i.e., it has an effect on any type of simulated feature especially if the feature is over a topographic structure. In spectral models, filtering is applied to topography to reduce the Gibbs oscillations, which are artificial waves inherent to Fourier transforms over steep gradients (such as high mountains). To eliminate (or reduce) these numerical artifacts, the topography is smoothed via filters. A convolution kernel is applied to the harmonic coefficients for the spectral representation of orography and the high-wavenumber part of the spectrum is damped. The convolution kernel for the triangular truncation in the CAM Eulerian Spectral model is:

$$\sigma_n^m = 1 - \left(\frac{n}{1.4N}\right)^2 \tag{26}$$

where σ is the kernel function which is multiplied by harmonic coefficients and is only a function of n which is the total wavenumber of the spherical harmonics. N is the truncation parameter (i.e., for the case of T85 spectral truncation, $N = 85$) and m is the zonal wavenumber. This is a two dimensional filter where the above kernel is applied to the zonal (Fourier) and the meridional (Legendre) coefficients equally. It is an effective

filter that leads to a strong smoothing, which does not guarantee shape preservation of the horizontal features (Navarra et al. 1994). The effect of the strong smoothing is observed in this study especially in coarse resolution (T85) as shown in Figure 14. Our study confirms this effect as the primary reason for the merger of two large-scale upslope ascent precipitation features simulated over the Coast Range and Sierra Nevada by the spectral dynamical core (Figure 6). The merger was also quantified by k-means clustering (Figure 20). One remedy to this situation is the application of a less aggressive filter using a kernel that will produce less severe dampening with more "tunable" parameters. One candidate for such filter is an exponential filter, which is designed empirically (therefore known also as pseudo-differential operators) in the form:

$$\sigma_n^m = exp[-\alpha(n/N)]^{2\beta} \tag{27}$$

where $\alpha = 32$ and $\beta = 2, 4, 8$ are usually used (Navarra et al. 1994). A non-uniform smoothing spline combined with a zonal filter is also shown to improve the simulation of orographic precipitation by spectral models (Lindberg and Broccoli 1996).

The right choice of the spectral filtering method of topography is not straightforward due to the dependence of the simulations on the spatial scales of topography. We were able to show that dependence by running the CAM 5.0 spectral dynamical core without the filtering with the idealized topographies. The removal of the filtering improved the simulation of precipitation in the double mountain case (Figure 13), and reduced the level of merger of the two large-scale stable upslope ascent features over the mountains. However the removal of filtering exacerbated the results in the realistic case where the leeward mountain height is doubled, thus introducing a much bigger gradient. Therefore the most efficient method to smooth the topography should be variable depending on the local gradient.

Bias in small-scale phenomena due to spectral transform method is a local source of bias that affects relatively small scales, and in the case of precipitation, when there are high amounts of rain introduced by physical parameterizations. The procedure for the coupling of dynamics and physics in CAM 5.0 plays an important role in the manifestation of this type of bias in spectral dynamical core. In CAM 5.0, there are two types of coupling strategies, namely time split and process split. In the time split coupling, dynamics and physics are calculated sequentially, each based on the state produced by other. Whereas in the process split coupling the calculations of dynamics and physics are both based on the same past state (Neale et al. 2010). Between the two coupling strategies, process split is more suitable for spectral transform models (and it is the default in CAM 5.0) since the time split requires extra spectral transforms to convert the momentum variables provided by the physical parameterizations. The formulation of the CAM spectral model is such that every physical process is calculated and updated on the Gaussian grid, and then their contribution to the dynamics is transformed to spectral space. This procedure creates problems when dealing with discontinuous physical processes that occur in small-scale such as the ones highlighted in this study (small-scale features in Figure 10).

As indicated throughout this dissertation and quantified in Figure 32, the manifestation of the small-scale features due to local evaporation and lee-side convergence have significant contribution from the surface flux parameterization of the simple physics suite and a key component of this evaporation is the SST value of the aquaplanet setting. Once the Gaussian grid precipitation value is updated by surface flux parameterizations, it introduces a relatively high value of precipitation on the grid level and causes a "jump" between the previous and current time states. This jump is not handled accurately with the spectral transform method and numerical noise is introduced. This noise is clearly observed in Figure 28b and Figure 28f where we quantified the initial oscillatory behavior of double mountain test case small-scale feature simulated by the CAM Eulerian Spectral model immediately after its genesis. As the simulation

proceeds, the oscillations become less severe since the grid values become similar between the previous and current time states and consequently the spectral transform method produces lesser numerical noise.

However, we also showed that such noise is not as prominent for the same type of feature in the realistic test case (Figure 31). This is also related to the interaction between physical parameterizations and dynamics. The planetary boundary layer (PBL) diffusion in simple-physics suite is parameterized such that the physical processes below 850 hPa are affected by it (Reed and Jablonowski 2012). In the double mountain case for the spectral model, the peak mountain height is below 850 hPa (the smoothing of the topography by filtering also contributes to that) therefore the small-scale scale features simulated over the mountain are affected by PBL parameterization. Whereas the leeward mountain in the realistic case (where the small-scale features occur) is sufficiently higher so that the PBL parameterization doesn't have any effect. Therefore, there is more contribution from physics in Gaussian grid level in the double mountain case, which results in considerable amount of bias when the values are transformed to the spectral space.

Grid scale variability (noise) due to spectral transform method is a global source of bias associated with spectral transform methods. As shown over the background precipitation field (Figure 33) there is inherent variability over grid-scale values of precipitation resulting from the spectral harmonics. The semivariogram of CAM FV 0.5 degrees resolution in Figure 33 is smooth, which indicates higher spatial continuity in the grid-scale as opposed to the discontinuity apparent in CAM Eulerian Spectral T170 simulation (i.e., wiggles in the semivariogram of CAM Eulerian Spectral T170). This type of bias is not as significant as the ones introduced by filtering of the topography and the coupling of physics and dynamics. However, it affects any type of variable, whether highly discontinuous (e.g., precipitation) or smooth (e.g., temperature) and it has to be

taken into account when evaluating models that make use of spectral transformations such as the spectral element dynamical core.

Finally, we place this work in context with some of the previous work on effective resolution of dynamical cores. Williamson (2008) examined the two dynamical cores used here to establish equivalent resolutions. Williamson used an aquaplanet configuration and examined zonal and global means of diagnostics relevant to momentum, energy, moist physics and the transport of those parameters. Williamson (2008) concludes that CAM FV 1 degree (0.5 degree) and CAM Eulerian Spectral T85 (T170) are equivalent. With the introduction of simple topography in our study, we see significant quantitative and qualitative differences in the spatial patterns of precipitation at resolutions that Williamson (2008) determined to be equivalent. This suggests that topographic precipitation amplifies differences in the schemes that were not discernable in Williamson's (2008) analysis.

Kent et al. (2014) explored the effective resolution of numerical algorithms used in dynamical cores of general circulation models. In most models the dynamics interact with the physics at the scale of the grid. However, at the scale of the grid, dynamical variables are far below the resolved scales of the numerical schemes. There is a range of scales between the grid size and a number of grid boxes where the dynamical features are not fully resolved. The suggestion from these results is that as the dynamical variables span the scales from fully resolved to partially resolved and to the grid scale, that the physics, which are acting at the grid scale, are not treated in the same way by the dynamical cores. Hence the end result of the coupling between the dynamics and physics, e.g. the precipitation, takes on different characteristics for different dynamical cores. This will be explored more fully in future studies.

REFERENCES

Airey, M., and M. Hulme, 1995: Evaluating climate model simulations of precipitation: Methods, problems and performance. *Progress in Physical Geography*, **19,** 427-448.

Alhamed, A., S. Lakshmivarahan, and D. J. Stensrud, 2002: Cluster analysis of multimodel ensemble data from SAMEX. *Monthly Weather Review*, **130,** 226-256.

Alpert, P., 1986: Mesoscale Indexing of the Distribution of Orographic Precipitation over High Mountains. *Journal of Climate and Applied Meteorology*, **25,** 532-545.

Bader, M. J., and W. T. Roach, 1977: Orographic Rainfall in Warm Sectors of Depressions. *Quarterly Journal of the Royal Meteorological Society*, **103,** 269-280.

Bala, G., R. B. Rood, D. Bader, A. Mirin, D. Ivanova, and C. Drui, 2008a: Simulated climate near steep topography: Sensitivity to numerical methods for atmospheric transport. *Geophysical Research Letters*, **35**, 1-5.

Bala, G., and Coauthors, 2008b: Evaluation of a CCSM3 simulation with a finite volume dynamical core for the atmosphere at 1 degrees latitude x 1.25 degrees longitude resolution. *Journal of Climate*, **21,** 1467-1486.

Baldwin, M. E., and S. Lakshmivarahan, 2003: Development of an events-oriented verification system using data mining and image processing algorithms. *Preprints, 3rd Conf. on Artificial Intelligence, Long Beach, CA, Amer. Meteor. Soc., paper 4.6.*

Baldwin, M. E., S. Lakshmivaravan, and J. S. Kain, 2002: Development of an "events-oriented" approach to forecast verification. *Preprints, 19th Conf. on weather Analysis and Forecasting/15th Conf. on Numerical Weather Prediction, Amer. Meteor. Soc., paper 7B.3*.

Banacos, P. C., and D. M. Schultz, 2005: The use of moisture flux convergence in forecasting convective initiation: Historical and operational perspectives. *Weather and Forecasting*, **20,** 351-366.

Banta, R. M., 1990: *The role of mountain flows in making clouds.* Atmospheric Processes over Complex Terrain. Meteorol Monograph 23: 229-283.

Barros, A. P., and D. P. Lettenmaier, 1993: Dynamic Modeling of the Spatial-Distribution of Precipitation in Remote Mountainous Areas. *Monthly Weather Review*, **121,** 1195-1214.

——, 1994: Incorporation of an Evaporative Cooling Scheme into a Dynamic-Model of Orographic Precipitation. *Monthly Weather Review*, **122,** 2777-2783.

Barros, A. P., G. Kim, E. Williams, and S. W. Nesbitt, 2004: Probing orographic controls in the Himalayas during the monsoon using satellite imagery. *Natural Hazards and Earth System Sciences*, **4,** 29-51.

Becker, E. J., E. H. Berbery, and R. W. Higgins, 2011: Modulation of Cold-Season US Daily Precipitation by the Madden-Julian Oscillation. *Journal of Climate*, **24,** 5157-5166.

Bergeron, T., 1968: On the low-level distribution of atmospheric water caused by orography. *Presented at Int. Cloud Phys. Conf., Toronto*.

Bhushan, S., and A. P. Barros, 2007: A numerical study to investigate the relationship between moisture convergence patterns and orography in central Mexico. *Journal of Hydrometeorology*, **8,** 1264-1284.

Bosilovich, M. G., Y. C. Sud, S. D. Schubert, and G. K. Walker, 2003: Numerical simulation of the large-scale North American monsoon water sources. *Journal of Geophysical Research-Atmospheres*, **108**.

Breiman, L., J. H. Friedman, R. A. Olshen, and C. J. Stone, 1984: *Classification and Regression Trees.* CRC Press.

Bryan, G. H., and J. M. Fritsch, 2002: A benchmark simulation for moist nonhydrostatic numerical models. *Monthly Weather Review*, **130,** 2917-2928.

Carruthers, D. J., and T. W. Choularton, 1983: A Model of the Feeder Seeder Mechanism of Orographic Rain Including Stratification and Wind-Drift Effects. *Quarterly Journal of the Royal Meteorological Society*, **109,** 575-588.

Choularton, T. W., and S. J. Perry, 1986: A Model of the Orographic Enhancement of Snowfall by the Seeder-Feeder Mechanism. *Quarterly Journal of the Royal Meteorological Society*, **112,** 335-345.

Colle, B. A., 2008: Two-dimensional idealized simulations of the impact of multiple windward ridges on orographic precipitation. *Journal of the Atmospheric Sciences*, **65,** 509-523.

Collins, W. D., and Coauthors, 2006: The Community Climate System Model version 3 (CCSM3). *Journal of Climate*, **19,** 2122-2143.

Davis, C., B. Brown, and R. Bullock, 2006: Object-based verification of precipitation forecasts. Part I: Methodology and application to mesoscale rain areas. *Monthly Weather Review*, **134,** 1772-1784.

Douglass, B. P., 2000: *Real-time UML: Developing Efficient Objects for Embedded Systems.* Addison Wesley, 328 pp.

Dryden, I. L., and K. V. Mardia, 1998: *Statistical Shape Analysis.* John Wiley & Sons.

Ebert, E. E., and J. L. McBride, 2000: Verification of precipitation in weather systems: determination of systematic errors. *Journal of Hydrology*, **239,** 179-202.

Eltahir, E. A. B., and R. L. Bras, 1996: Precipitation recycling. *Reviews of Geophysics*, **34,** 367-378.

Everitt, B. S., S. Landau, M. Leese, and D. Stahl, 2011: *Cluster Analysis.* Wiley. Frankhauser, J. C., 1965: A comparison of kinematically computed precipitation with observed convective rainfall. *National Severe Storms Laboratory Rep.* , **25,** 28.

Gates, W. L., 1992: AMIP - the Atmospheric Model Intercomparison Project. *Bulletin of the American Meteorological Society*, **73,** 1962-1970.

Gates, W. L., and Coauthors, 1999: An overview of the results of the Atmospheric Model Intercomparison Project (AMIP I). *Bulletin of the American Meteorological Society*, **80,** 29-55.

Gilleland, E., 2013: Testing Competing Precipitation Forecasts Accurately and Efficiently: The Spatial Prediction Comparison Test. *Monthly Weather Review*, **141,** 340-355.

Gilleland, E., D. Ahijevych, B. G. Brown, B. Casati, and E. E. Ebert, 2009: Intercomparison of Spatial Forecast Verification Methods. *Weather and Forecasting*, **24,** 1416-1430.

Hoffman, R. N., Z. Liu, J. F. Louis, and C. Grassotti, 1995: Distortion Representation of Forecast Errors. *Monthly Weather Review*, **123,** 2758-2770.

Holman, K. D., and S. J. Vavrus, 2012: Understanding Simulated Extreme Precipitation Events in Madison, Wisconsin, and the Role of Moisture Flux Convergence during the Late Twentieth and Twenty-First Centuries. *Journal of Hydrometeorology*, **13,** 877-894.

Houze, R. A., and S. Medina, 2005: Turbulence as a mechanism for orographic precipitation enhancement. *Journal of the Atmospheric Sciences*, **62,** 3599-3623.

Hudson, H. R., 1970: On the relationship between horizontal moisture convergence and convective cloud formation. *ESSA Tech. Memo.*, **ERLTM-NSSL** 29.

Huth, R., I. Nemesova, and N. Klimperova, 1993: Weather Categorization Based on the Average Linkage Clustering Technique - an Application to European Midlatitudes. *International Journal of Climatology*, **13,** 817-835.

Iorio, J. P., P. B. Duffy, B. Govindasamy, S. L. Thompson, M. Khairoutdinov, and D. Randall, 2004: Effects of model resolution and subgrid-scale physics on the simulation of precipitation in the continental United States. *Climate Dynamics*, **23,** 243-258.

Isaaks, E. H., and R. M. Srivastava, 1989: *Applied Geostatistics.* Oxford University Press.

Jablonowski, C., and D. L. Williamson, 2011: The Pros and Cons of Diffusion, Filters and Fixers in Atmospheric General Circulation Models. *Numerical Techniques for Global Atmospheric Models*, Springer-Verlag Berlin Heidelberg, pp 381-493.

Jablonowski, C., P. H. Lauritzen, R. D. Nair, and M. Taylor, 2008: Idealized test cases for the dynamical cores of Atmospheric General Circulation Models: A proposal for the NCAR ASP 2008 summer colloquium. *Technical Report*.

Jiang, Q. F., and R. B. Smith, 2003: Cloud timescales and orographic precipitation. *Journal of the Atmospheric Sciences*, **60,** 1543-1559.

Johnson, A., X. G. Wang, F. Y. Kong, and M. Xue, 2011: Hierarchical Cluster Analysis of a Convection-Allowing Ensemble during the Hazardous Weather Testbed 2009 Spring Experiment. Part I: Development of the Object-Oriented Cluster Analysis Method for Precipitation Fields. *Monthly Weather Review*, **139,** 3673-3693.

Kent, J., J. P. Whitehead, C. Jablonowski, and R. B. Rood, 2014: Determining the effective resolution of advection schemes. Part I: Dispersion Analysis. *Journal of Computational Physiscs*, **In press**.

Lakshmanan, V., R. Rabin, and V. DeBrunner, 2003: Multiscale storm identification and forecast. *Atmospheric Research*, **67-8,** 367-380.

Lin, S. J., 2004: A "vertically Lagrangian" finite-volume dynamical core for global models. *Monthly Weather Review*, **132,** 2293-2307.

Lin, S. J., and R. B. Rood, 1996: Multidimensional flux-form semi-Lagrangian transport schemes. *Monthly Weather Review*, **124,** 2046-2070.

——, 1997: An explicit flux-form semi-Lagrangian shallow-water model on the sphere. *Quarterly Journal of the Royal Meteorological Society*, **123,** 2477-2498.

Lin, Y., and K. E. Mitchell, 2005: The NCEP Stage II/IV hourly precipitation analyses: development and applications. *Preprints, 19th Conf. on Hydrology, American Meteorological Society, San Diego, CA, 9-13 January 2005, Paper 1.2.*

Lindberg, C., and A. J. Broccoli, 1996: Representation of topography in spectral climate models and its effect on simulated precipitation. *Journal of Climate*, **9,** 2641-2659.

Littmann, T., 2000: An empirical classification of weather types in the Mediterranean Basin and their interrelation with rainfall. *Theoretical and Applied Climatology*, **66,** 161-171.

Liu, Z., and R. George, 2005: *Mining Weather Data Using Fuzzy Cluster Analysis.* Springer Berlin Heidelberg.

Loh, W.-Y., 2011: Classification and Regression Trees. *Wiley Interdisciplinary Reviews: Data Mining and Knowledge Discovery*, **1,** 14-23.

Marzban, C., and S. Sandgathe, 2006: Cluster analysis for verification of precipitation fields. *Weather and Forecasting*, **21,** 824-838.

——, 2009: Verification with Variograms. *Weather and Forecasting*, **24,** 1102-1120.

Matheron, G., 1963: Principles of Geostatistics. *Economic Geology*, **58,** pp. 1246-1266.

McGuffie, K., and A. Henderson-Sellers, 2005: *A Climate Modelling Primer.* 170-174 pp.

Micheas, A. C., I. F. Neil, S. A. Lack, and C. K. Wikle, 2007: Cell identification and verification of QPF ensembles using shape analysis techniques. *Journal of Hydrology*, **343,** 105-116.

Miglietta, M. M., and R. Rotunno, 2009: Numerical Simulations of Conditionally Unstable Flows over a Mountain Ridge. *Journal of the Atmospheric Sciences*, **66,** 1865-1885.

Navarra, A., W. F. Stern, and K. Miyakoda, 1994: Reduction of the Gibbs Oscillation in Spectral Model Simulations. *Journal of Climate*, **7,** 1169-1183.

Neale, R. B., and Coauthors, 2010: Description of the NCAR Community Atmosphere Model (CAM 5.0). National Center for Atmospheric Research (*NCAR) Technical Note*, **NCAR/TN-486+STR**.

Neale, R. B., and B. J. Hoskins, 2000: A standard test for AGCMs including their physical parametrizations: I: The proposal. AtScL, 1, 101-107.

Newman, W. R., 1971: The relationship between horizontal moisture convergence and severe storm occurrences. M.S. Thesis, School of Meteorology, University of Oklahoma, 54 pp.

Notaro, M., S. Vavrus, and Z. Y. Liu, 2007: Global vegetation and climate change due to future increases in CO2 as projected by a fully coupled model with dynamic vegetation. *Journal of Climate*, **20,** 70-90.

Peak, J. E., and P. M. Tag, 1994: Segmentation of Satellite Imagery Using Hierarchical Thresholding and Neural Networks. *Journal of Applied Meteorology*, **33,** 605-616.

Posselt, D. J., A. R. Jongeward, C. Y. Hsu, and G. L. Potter, 2012: Object-Based Evaluation of MERRA Cloud Physical Properties and Radiative Fluxes during the 1998 El Nino-La Nina Transition. *Journal of Climate*, **25,** 7313-7327.

Preisendorfer, R. W., and T. P. Barnett, 1983: Numerical-Model Reality Intercomparison Tests Using Small-Sample Statistics. *Journal of the Atmospheric Sciences*, **40,** 1884-1896.

Rasch, P. J., D. B. Coleman, N. Mahowald, D. L. Williamson, S. J. Lin, B. A. Boville, and P. Hess, 2006: Characteristics of atmospheric transport using three numerical formulations for atmospheric dynamics in a single GCM framework. *Journal of Climate*, **19,** 2243-2266.

Reed, K. A., and C. Jablonowski, 2012: Idealized tropical cyclone simulations of intermediate complexity: A test case for AGCMs. *Journal of Advances in Modeling Earth Systems*, **4**, M04001.

Rienecker, M. M., and Coauthors, 2008: The GEOS-5 Data Assimilation System - Documentation of versions 5.0.1, 5.1.0, and 5.2.0. Technical Report Series on Global Modeling and Data Assimilation 104606, **v27**.

Roe, G. H., 2005: Orographic precipitation. *Annual Review of Earth and Planetary Sciences*, **33,** 645-671.

Roe, G. H., and M. B. Baker, 2006: Microphysical and geometrical controls on the pattern of orographic precipitation. *Journal of the Atmospheric Sciences*, **63,** 861-880.

Rood, R., 2011: A Perspective on the Role of the Dynamical Core in the Development of Weather and Climate Models. *Numerical Techniques for Global Atmospheric Models*, P. Lauritzen, C. Jablonowski, M. Taylor, and R. Nair, Eds., Springer Berlin Heidelberg, 513-537.

Sanberg, J. A. M., and J. Oerlemans, 1983: Modeling of Pleistocene European Ice Sheets - the Effect of Upslope Precipitation. *Geologie En Mijnbouw*, **62,** 267-273.

Santer, B. D., and T. M. L. Wigley, 1990: Regional Validation of Means, Variances, and Spatial Patterns in General-Circulation Model Control Runs. *Journal of Geophysical Research-Atmospheres*, **95,** 829-850.

Santer, B. D., and Coauthors, 2009: Incorporating model quality information in climate change detection and attribution studies. *Proceedings of the National Academy of Sciences of the United States of America*, **106,** 14778-14783.

Sinclair, M. R., 1994: A Diagnostic Model for Estimating Orographic Precipitation. *Journal of Applied Meteorology*, **33,** 1163-1175.

Skok, G., J. Bacmeister, and J. Tribbia, 2013: Analysis of Tropical Cyclone Precipitation Using an Object-Based Algorithm. *Journal of Climate*, **26,** 2563-2579.

Smith, R. B., 1979: The influence of mountains on the atmosphere. *Adv. Geophys.*, **21,** 87-230.

——, 2003: A linear upslope-time-delay model for orographic precipitation. *Journal of Hydrology*, **282,** 2-9.

Smith, R. B., and I. Barstad, 2004: A linear theory of orographic precipitation. *Journal of the Atmospheric Sciences*, **61,** 1377-1391.

Spath, H., 1985: *Cluster dissection and analysis: theory, FORTRAN programs, examples.* Ellis Horwood Ltd. Wiley, Chichester, 226.

Thuburn, J., 2008: Some conservation issues for the dynamical cores of NWP and climate models. *Journal of Computational Physics*, **227,** 3715-3730.

Tomita, H., and M. Satoh, 2004: A new dynamical framework of nonhydrostatic global model using the icosahedral grid. *Fluid Dynamics Research*, **34,** 357-400.

Wernli, H., M. Paulat, M. Hagen, and C. Frei, 2008: SAL-A Novel Quality Measure for the Verification of Quantitative Precipitation Forecasts. *Monthly Weather Review*, **136,** 4470-4487.

Williamson, D. L., 2007: The evolution of dynamical cores for global atmospheric models. *Journal of the Meteorological Society of Japan*, **85B,** 241-269.

——, 2008: Equivalent finite volume and Eulerian spectral transform horizontal resolutions established from aqua-planet simulations. *Tellus Series a-Dynamic Meteorology and Oceanography*, **60,** 839-847.

Williamson, D. L., and P. J. Rasch, 1994: Water-Vapor Transport in the NCAR-CCM2. *Tellus Series a-Dynamic Meteorology and Oceanography*, **46,** 34-51.

Xu, K. M., T. M. Wong, B. A. Wielicki, L. Parker, and Z. A. Eitzen, 2005: Statistical analyses of satellite cloud object data from CERES. Part I: Methodology and preliminary results of the 1998 El Nino/2000 La Nina. *Journal of Climate*, **18,** 2497-2514.